Theoretical studies of the constriction of rare-gas glow discharge plasmas

I n a u g u r a l d i s s e r t a t i o n

zur

Erlangung des akademischen Grades eines
doctor rerum naturalium (Dr. rer. nat.)
an der Mathematisch-Naturwissenschaftlichen Fakultät
der
Ernst-Moritz-Arndt-Universität Greifswald

vorgelegt von
Mykhaylo Gnybida
geboren am 01.04.1982
in Kamenez-Podolskij,
Ukraine

Greifswald, im März 2010

Dekan:	Prof. Dr. Klaus Fesser
1. Gutachter:	PD Dr. Detlef Loffhagen
2. Gutachter:	Prof. Dr. Karl-Heinz Spatschek
Tag der Promotion:	2. Juli 2010

Zusammenfassung

In der vorliegenden Arbeit wurde ein Fluidmodell entwickelt, das den raumzeitlichen Übergang einer diffusen Entladung zur kontrahierten Entladung beschreibt. Das Modell wurde als selbstkonsistent aufgebaut, so dass Teilchenbilanzgleichugen für alle relevanten Spezies, die Bilanz für die mittlere Elektronenenergie und die Schwerteilchentemperatur, die Poisson-Gleichung zur Bestimmung des elektrischen Potentials sowie die Bilanzgleichung des elektrischen Strom im Plasma gelöst wurden. Dem Modell wurde die nichtlokale Momentenmethode zugrunde gelegt, in dem die Bilanzgleichungen für makroskopische Größen aus den Momenten der radialabhängigen Boltzmann-Gleichung hergeleitet wurden. Die Transportparameter der Elektronen und die Ratenkoeffizienten der Prozesse zwischen Elektronen und Schwerteilchen wurden als Funktion der mittleren Elektronenenergie, der Gastemperatur und des Ionizationsgrades bestimmt.

Mit Hilfe des Modells wurde erstmalig die Kontraktion der positiven Säule einer DC-Entladung in Argon untersucht, wobei eine weiträumige Variation des Druckes und des elektrischen Stromes vorgenommen wurde. Die Ergebnisse demonstrierten ein ausgeprägtes nichtlokales Verhalten der Energiebilanz der Elektronen, dessen Einfluss auf die kontrahierte Argon-Entladung ferner analysiert wurde. Dazu wurden unterschiedliche Annahmen über die Form der Elektronengeschwindigkeitsverteilungsfunktion (EGVF) in Betracht gezogen. Eine Maxwellsche Geschwindigkeitsverteilung erwies sich als ungeeignet. Im Gegenteil, führte eine Druyvesteynsche Verteilungsfunktion zu einem Übergang von Glimmentladung zur kontrahierten Entladung. Dennoch wurde eine signifikante Diskrepanz mit aus Experimenten gewonnenen Daten beobachtet. Eine zufriedenstellende Übereinstimmung zwischen Experiment und Modellierung konnte jedoch erzielt werden, indem die EGVF als Lösung der stationären, räumlich homogenen Boltzmann-Gleichung unter Berücksichtigung der Elektron-Elektron-Stöße bestimmt wurde.

Das entwickelte Fluidmodell wurde als nächstes zur Untersuchung der Eigenschaften der positiven Säule einer kontrahierten Mitteldruckentladung in Xenon eingesetzt. Die Simulationsergebnisse ermöglichten einen detaillierten Einblick in

die physikalischen Mechanismen gepulster Entladungen in Xenon. Die Stufenionisation der angeregten Atome, die Umwandlung atomarer Ionen in molekulare Ionen sowie die dissoziative Rekombination molekularer Ionen wurden als dominante Prozesse in der positiven Säule der kontrahierten Xenon-Entladung erkannt. Das Modell konnte Ergebnisse in guter Übereinstimmung mit dem Experiment liefern. Insbesondere wurden der deutliche Anstieg der Dichte angeregter Atome in den unteren Niveaus sowie der Anstieg der Xe_2^*-Dichten während der Abklingphase wiedergegeben.

Abstract

In the present work, a time- and radial-dependent fluid model has been developed to describe the glow-to-arc transition of the positive column in the course of constriction. The self-consistent model comprises the particle balance equations for the relevant species, the balance equation of the mean electron energy and the heavy particle temperature in the plasma, the Poisson equation for the space-charge potential, and a current balance determining the axial electric field. The model adopts the nonlocal moment method, i.e., the system of the balance equations resulting from the moments of the radially dependent Boltzmann equation is solved. The electron transport and rate coefficients are adapted as functions of the mean energy of the electrons, the gas temperature and the ionization degree.

The model is applied to a description of the constriction of the dc positive column in argon, for a wide range of pressures and applied currents. Pronounced nonlocal features of the mean electron energy balance are found and their influence on the constricted argon positive column is analyzed. Different assumptions concerning the electron velocity distribution function (EVDF) have been considered in the present model. The assumption of a Maxwellian distribution for the electrons was found to be inappropriate, while the assumption of a Druyvesteyn distribution for the electrons was found to be suitable for describing qualitatively the glow-to-arc transition. However, the standard model using the EVDF obtained from the solution of the steady-state, spatially homogeneous electron Boltzmann equation including electron-electron collisions allows to describe the constriction effect and provides best agreement with experimental data and other available modelling results.

The fluid model has also been used to study a medium-pressure pulsed positive column in xenon at conditions of the contracted discharge. The simulation results provide a detailed insight in the physical mechanisms of xenon discharges in pulsed mode. The stepwise ionization of the excited atoms, the conversion of the atomic ions into molecular ions as well as the dissociative recombination of the molecular ions are found to be the most important processes for the pulsed positive column in xenon plasmas at conditions of the contracted discharge. The comparison of the model predictions with experimental results generally shows

good agreement. In particular, the model predictions are suitable for qualitative reproduction of the significant increase of low-lying atomic levels densities as well as of the higher and of the relaxed lowest vibrational states of the Xe_2^* excimers in the afterglow phase of the pulse.

Contents

List of Figures

List of Tables

1 Introduction

This thesis deals with the analysis of the glow-to-arc transition process in positive column plasmas by means of numerical modelling. In the following chapter the subject of interest is introduced by a short overview of gas discharges, by describing non-equilibrium and equilibrium modes of a steady-state gas discharge, and their applications. Afterwards, various numerical approaches to gas discharge modelling are discussed. Finally, the aim of the present studies and an outlook over the following chapters are presented.

1.1 Gas discharges

The term "gas discharge" is applied to any flow of electric current through an ionized gas, and to any process of ionization of the gas by the applied electric field [1]. A gas discharge can be generated using relatively simple experimental apparatus [Fig. 1.1]. Two metal electrodes connected to a dc power supply are inserted into a glass tube. An external resistance is connected in series with the discharge. The tube can be evacuated and filled with various gases at different pressures. The quantities measured in the experiment are the voltage between the electrodes and the current in the circuit.

Various industrial and laboratory gas discharges are operated at pressures ranging from close to vacuum to several atmospheres. At low pressure conditions, say from 0.1 to 10 Torr, and high resistance of the external circuit [1], a glow discharge develops. Here, the plasma fills the whole volume and emits low-intensity

[1] It prevents the current from reaching a large value.

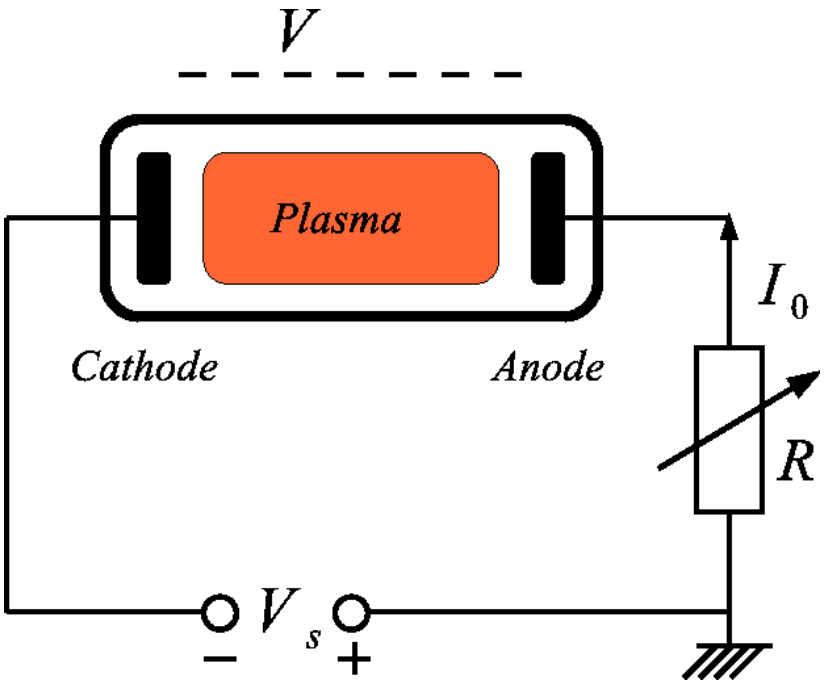

Figure 1.1: Gas discharge.

light. Glow discharges are characterized by a low current, $I_0 \sim 10^{-6} - 10^{-1}$ A in tubes of radius $R \sim 1$ cm, and rather high voltage: from hundreds to thousands of volts. The glow discharge plasma is weakly ionized, to $n_e/N = 10^{-8} - 10^{-6}$ (where n_e/N denotes ratio between electrons and ground state atoms), and it is in non-equilibrium in many aspects. First of all, the glow plasma is in non-equilibrium with respect to radiation, for which it is transparent in many spectral ranges. In this case own radiation of the plasma freely leaves the discharge tube and, therefore, the principle of detailed balancing cannot be satisfied. In glow plasma excitation and de-excitation processes are not balanced and so the distribution of the excited states of the neutral atoms is far from equilibrium (Boltzmann) distribution. Due to low ionization degree the plasma of the glow discharge is not in ionization equilibrium, i.e., distribution of the charged species does not obey Saha equation. The electron component of the glow discharge plasma captures energy directly from the external electric field, has a mean energy $U_e \approx 3 - 6$ eV, which corresponds to a "temperature" $T_e \approx 20000 - 40000$ K, and has non-equilibrium

(non-Maxwell) electron velocity distribution function (EVDF). The heavy particles (ions and neutrals) have a Maxwell energy distribution because of their intensive energetic contact in elastic collision processes. The temperature T_h of the gas, including the ions, is not much higher than the ambient temperature of 300 K. A plasma with above properties is often called as cold or non-thermal or non-equilibrium plasma.

At higher pressures, say around atmospheric level, and low resistance of the external circuit [1], an arc discharge develops. Arcs are characterized by high current ($I_0 > 1$ A) and a low voltage of several tens of volts. They form a bright narrow column. Arc plasmas are usually partially or strongly ionized gases with ionization ratio of $n_e/N = 10^{-3} - 10^{-1}$. The energy from the external electric field is mainly got by the electrons due to their high mobility. Part of this energy is transfered to the heavy particles by elastic collisions. The high value of the electron density n_e in the arc plasma is responsible for high elastic electron-neutral frequencies, which usually leads to Maxwell energy distribution function for all types of the particles. Thermodynamic equilibrium is established: the mean heavy particle energy is the same as the mean electron energy. In the core of the arc plasma, this mean energy is of the order of 1 eV, which corresponds to a temperature of the order of 10^4 K. The high value of the electron density is also mainly responsible for a high value of the inelastic collision frequencies. Inelastic collisions tend to establish a statistical equilibrium among all the kinds of particles; i.e., excited atoms and ions tend to obey equilibrium laws, such as Boltzmann and Saha laws. Such assumption is completed by radiation equilibrium (Planck) law, which, in general, is only verified in the hottest regions of the arc plasmas, but not in the outer (cold) regions. This limitation does not allow to consider that arc plasmas are in a state of thermodynamic equilibrium. Nevertheless, it is possible to assume that arc plasmas are in state of a local thermodynamic equilibrium (LTE), where the particle number densities are given by the equilibrium laws (due to high collision frequencies), but radiation does not obey Planck law. Plasmas with above properties are often called as hot or thermal or equilibrium plasmas.

[1] The circuit allows a passage of a high current.

1.2 Glow-to-arc transition

Glow and arc discharges are representative of non-equilibrium and equilibrium plasmas, respectively. Such types of discharges are well studied both theoretically and experimentally, and their properties, in general, are well understood. But there is a transition region between these two types of plasmas, which can neither be classified as a classical glow discharge nor as an arc discharge. Up to present days this glow-to-arc transition region is not well studied and discharge properties and mechanisms are not well known. Transition from non-equilibrium to equilibrium plasmas is observable at e.g.

- constriction of a glow discharge [2–4],
- glow-to-arc transition in the electrode region of glow discharges [5],
- atmospheric pressure glow discharges [6; 7],
- active laser media [8; 9],
- gliding arc discharge [10],
- arc plasmas at reduced pressures and currents [11].

Typical plasma parameters of the glow-to-arc transition are given in Table 1.1.

Table 1.1: Plasma parameters of the glow-to-arc transition.

Parameter	Range
Ionization degree	$10^{-6} - 10^{-3}$
Gas pressure	$10 - 760$ Torr
Discharge current	$0.001 - 10$ A
Gas temperature	$400 - 2000$ K
Mean electron energy	$1 - 3$ eV
Electron density	$10^{12} - 10^{15}$ cm^{-3}

The plasma is characterized by high sensitivity to instabilities. Due to the high value of the electron density n_e the plasma has a high electron-neutral collision frequency and high population of the excited species. Stepwise ionization become more important than direct one. Due to the high value of the gas pressure p, three-body reactions become important.

Plasma processing is widely used in semiconductor device fabrication, where one of the key steps is etching of material layers on wafer surfaces. Usually, low-pressure, non-equilibrium plasmas are used to dissociate and ionize a feed gas for the purpose of reactive ion etching [12]. Low-pressure plasmas are used in such applications as light sources for publicity lighting and fluorescent lamps for general lighting [13; 14].

At present, high-pressure, non-equilibrium plasmas are widely used in material processing applications. In particular, they include plasma-assisted chemical vapor deposition [15; 16], etching [17; 18], and polymer surface modification [19]. Also such types of plasmas are used in development of new excimer ultraviolet sources [20], high-power gas lasers [9], surface sterilization for healthcare [21], and water and air treatment systems [22].

In the present thesis the glow-to-arc transition of the positive column in rare-gas plasmas in the course of the constriction has been investigated.

1.3 Constriction of the positive column

The diffuse state of the positive column plasma of glow discharges can abruptly jump into a mode with strong inhomogeneities. One of the inhomogeneous modes is the constricted column [1]. Such a mode typically develops from the diffuse mode, when the pressure or the current is increased. This effect is undesirable in applications of gas discharge, as e.g., high-power gas lasers [1; 9] and excimer lamps [23].

The plasma constriction in the positive column in inert gases has been studied both experimentally [2–4; 24–33] and theoretically [2; 4; 24; 25; 28; 32; 34–40]. Experimental investigations have shown that filamentation of the positive column arises if pressure and discharge current are above critical values. This effect also depends on the tube radius. Below the critical values the plasma fills the

whole tube cross section and exists in the diffuse mode. Above the critical values the plasma column abruptly develops into a narrow filament. The transition from glow to constricted mode is accompanied by a sudden decrease of the axial electric field, an abrupt growth of the electron density at the discharge axis by more than one order of magnitude and a decrease of the mean electron energy. A hysteresis effect was observed, i.e., the transition from glow to constricted mode (with increasing current) and the opposite transition (with decreasing current) occurs at different values of discharge parameters [3; 37; 41].

The phenomenon of discharge constriction is not limited only to the dc sustained plasma in inert gases. It has also been observed in molecular and electronegative gases [42–45] as well as in microwave plasmas at atmospheric pressure [46].

Various analytical theories were implemented to explain the reasons of the constriction of glow discharges. These theories can be divided in two different groups. One group, which was historically the first, used the fact that the plasma is heated inhomogeneously when the current maintains the discharge. The plasma was characterized by the dependence of the local ionization-recombination balance of charged species on the heavy particle temperature [2; 24–27]. Some of the authors proposed to explain the constriction effect using the classical theory of arc plasmas [25–27]. Kenty [24] concentrated on the radial dependence of the recombination of charged particles and suggested that the contraction is due to an increase of the recombination coefficient from the of the discharge towards the wall caused by the radial decay of the heavy particle temperature. One of the shortcomings of the mentioned theories consists in the disregard of the diffusion in the charged particle balance.

Later on another group of theories, so-called diffusion-recombination theories, were suggested in the literature [3; 30; 32; 34; 37–39]. The term “diffusion” was used to emphasize the importance of the diffusion in the charged particle balance. According to these theories, a strong nonlinear dependence of the ionization rate on the spatial electron population is the key reason for constriction. This dependence results from the concurrence between electron-electron collisions, which tend to randomize the electron velocity distribution function (EVDF), and

electron-atom interactions, which tend to deplete the tail of the EVDF. Ambipolar diffusion to the wall is the major factor acting against constriction. It was shown by Golubovskii *et al.* [37–39] that electron-electron collisions play a key role in the abrupt constriction of glow discharges in inert gases (except for helium). If electron-electron collisions are neglected, constriction still occurs, but more gradually. These authors have also found that a nonuniform plasma heating is a minor factor for the column filamentation, but it produces additional contraction and reduces the critical pressure and current.

1.4 Gas discharge modelling

Gas discharges are a rather complex system, where different physical phenomena are included at the same time, and often quantities of interest cannot be observed directly. Moreover, quite often they cannot be explained by simplified theories, which describe the system. Numerical modelling is the link between theory and experiment.

The model of a physical phenomenon is a mathematical representation of all the major features of certain phenomenon. Usually, a model contains a system of equations for the physical quantities, relevant theoretical or experimental atomic data and assumptions. The modelling of the physical phenomenon is the process of solving of basic equations. Model results are used to validate and predict experimental results and vice versa. They can also be employed to e.g. optimize discharge or geometry parameters.

A complete model of a gas discharge requires three sub-models: an electrical (or plasma) model, a plasma chemistry model and a surface model. The different components of the gas discharge model and their interrelationship are shown in Fig. 1.2. Each of these components involves equations that determine the spatial and temporal variation of important quantities. The electrical model describes the behaviour of the charged particles in the discharge and comprises the charge particle transport and kinetic equations as well as Maxwell's equation. The plasma chemistry model treats the transport and kinetics of the different atomic and molecular species, and photons. In the surface model the interaction of the various species in the discharge with the walls and electrodes is described.

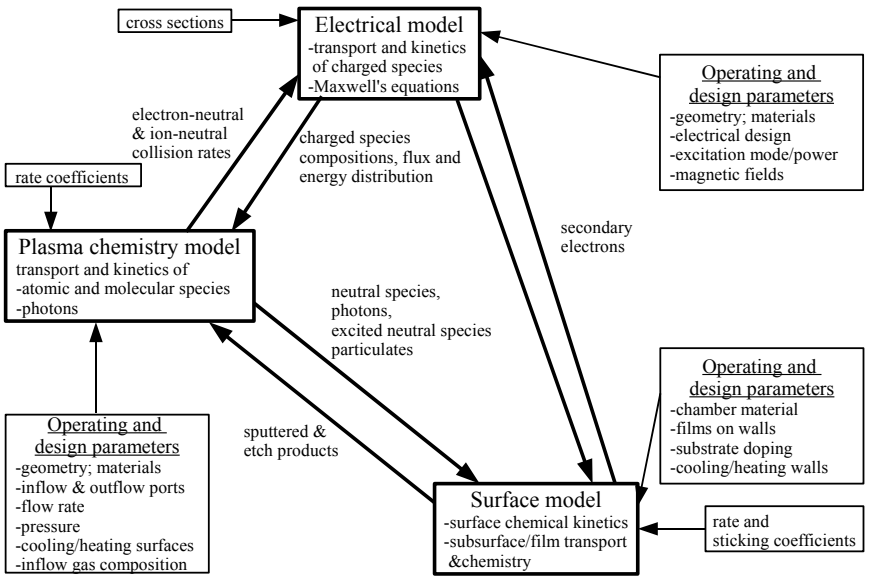

Figure 1.2: Components of the gas discharge model.

Different kinds of methods are used for the theoretical description of gas discharge plasmas ranging from fluid (or hydrodynamic) models over so-called hybrid methods to a fully kinetic treatment of the plasma. Each of these approaches has its particular advantages and shortcomings.

Fluid models are models in which the transport of the charge carriers and neutral components of the plasma are described by the first few velocity moments of the Boltzmann equation (BE) [47], where appropriate relations are used to close the system of equations. The fluid equations are usually complemented with Maxwell equations, such as Poisson's equations, to provide self-consistent solution and suitable boundary conditions, to describe plasma-surface interactions. The fluid models are in principle comparatively fast, but they take into account only partly nonequilibrium behaviour of charge carriers.

Kinetic models apply the particle-in-cell (PIC) technique for the transport of superparticles representing electrons and ions with a Monte Carlo collision (MCC) treatment of collisions between charged and neutral particles and cou-

pled with Poisson's equation on a spatially discretized mesh [48; 49]. Also, the term "kinetics" is used in literature in the context of solution of Boltzmann's equation for each component of the plasma with appropriate boundary and initial conditions. Further, the quantities of physical interest are obtained as velocity "moments" of the distribution function. The advantage of the kinetic method is accurate calculation of the quantities of the physical interest. However, application of the kinetic method is an extremely hard computational task, especially when electron-electron collisions are taken into account and a coupling with the Poisson equation to consider space charge field is required.

Hybrid approach is the combination of the two approaches: kinetic and fluid. It is mainly applied to systems, which consist of slow and fast particles [50]. The plasma description is represented by model, where the behaviour of the slow particles (ions and neutrals) are described by fluid approach, and the fast particles (electrons) are treated by kinetic approach.

1.5 Motivation and objectives of research

The major shortcoming of all mentioned theories in Section 1.3 is their semi-analytical nature. The discharge kinetics at different pressure ranges cannot be consistently described by means of analytical expressions for the ionization and recombination rates, the charged and excited states populations. Therefore, the proper description of the constriction of the positive column plasma requires the solution of the particle balance equations for the charged and neutral species and the thermal balance equation for the heavy particle temperature. The rate and transport coefficients of the electrons are provided from the solution of the BE for the EVDF. Using such approach 1D axisymmetric models were presented in [4; 40] and applied to investigate numerically the constriction phenomenon in pure argon. However, this approach fails to strictly describe the radial variation of the mean electron energy.

The impact of nonlocal behaviour in the electron kinetics, in particular, on the radial profiles of electric potential and electron mean energy has already been pointed out in [51]. In the present thesis the nonlocal moment method is adopted, where additionally to the particle balance equations of the relevant species and

the thermal balance equation for the heavy particle temperature the equation for the mean electron energy is treated [52]. Due to the expected strong gas heating and high electron density, transport and rate coefficients of electrons are adapted as functions of the mean electron energy, the gas temperature and the ionization degree. The constriction phenomenon in glow discharges in rare gases has been studied and the results are evaluated by comparison with available experimental data and other modelling results.

The main objectives of the research of the thesis are:

- development of a suitable model for the glow-to-arc transition region in positive column plasmas,
- analysis of the mechanism of the constriction of positive column plasmas,
- study of main physical processes of dc and pulsed glow plasmas at conditions of the contracted discharge.

1.6 Outline of the thesis

The Chapter 2 contains the theoretical basis of a self-consistent model, which is used to describe a gas discharge. The basic equation system adapted by this work is presented in this chapter. Numerical algorithms adopted to solve the system of equation are provided in the Chapter 3. The main numerical limitations are also discussed. In Chapter 4 modelling results of the constriction of the dc positive column in argon are given. They are compared with existing experimental and theoretical data. The analysis of the results focuses on the mechanism causing constriction and, in particular, on the energy balance of the electrons. Chapter 5 provides modelling results and analysis of a pulsed xenon glow discharge at medium pressure. Conclusions and an outlook are presented in Chapter 6.

2

Theoretical approach

In this chapter the self-consistent model to describe the glow-to-arc transition in positive column plasmas is presented. This model takes into account major physical aspects: the balance equations for the relevant species densities, the electron energy balance, the heavy particle energy balance, the action of electric fields, and the radiation transport. A detailed set of model equations is given in Section 2.1. These equations describe the relations between all important physical quantities in the plasma volume. The Poisson equation for the radial space-charge potential and a current balance determining the axial electric field are presented in Section 2.2. Details related to the description of the electron kinetics are given in Section 2.3. Plasma-surface interactions are included into the model as boundary conditions of the equations [Section 2.4]. Finally, details related to the collisional-radiative models of argon and xenon are presented in Section 2.5.

2.1 Model equations

2.1.1 Introduction

The positive column of gas discharge is described by a fluid approach which include a coupled solution of balance equations for the charge carrier and neutral species densities, mean electron energy, and the heavy particle temperature. These equations are coupled to Poisson's equation for the radial potential and a

current balance determining the axial electric field. The derivation of the fluid equations from the BE is described in [47].

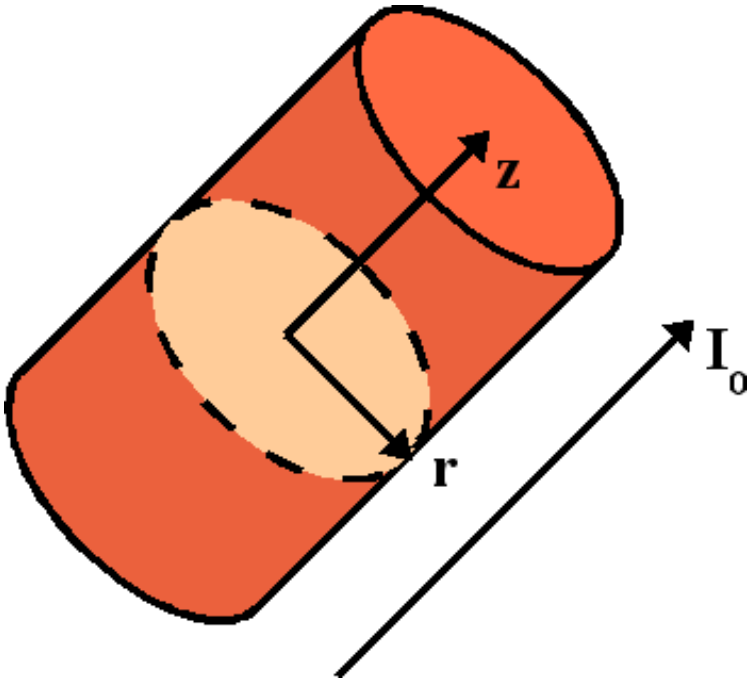

Figure 2.1: One-dimensional gas discharge geometry.

The positive column plasma is considered to be radially inhomogeneous, axially uniform along the axis z of the discharge tube with a radius R, and sufficiently far from the electrodes so that their influence can be ignored. For such assumptions, a 1D axisymmetric fluid model is applicable [Fig. 2.1].

2.1.2 Equations for the particle densities

The radially dependent electron balance equation is described by using zeroth moment of corresponding 1D electron BE and is written as follows [53; 54]

$$\frac{\partial}{\partial t} n_e(r,t) = -\frac{1}{r}\frac{\partial}{\partial r}\left(r\Gamma_e(r,t)\right) + S_e(r,t) \quad , \tag{2.1}$$

where Γ_e is the electron radial flux, expressed in drift-diffusion form

$$\Gamma_e(r,t) = -\frac{\partial}{\partial r}\left(n_e(r,t)D_e(r,t)\right) - \mu_e(r,t)n_e(r,t)E_r(r,t) \quad , \tag{2.2}$$

and S_e is the electron gain/loss term due to kinetic processes. D_e and μ_e are the electron free diffusion coefficient Eq. (B.2) and electron mobility Eq. (B.1), respectively, and E_r is the radial electric field. The first term gives the flux due to the electric field (drift) and the second term represents the flux due to the concentration gradients (diffusion). Particle inertia is neglected.

The radially dependent ion balance equation is described by using zeroth moment of corresponding 1D ion BE and is expressed as follows [53; 54]

$$\frac{\partial}{\partial t} n_j(r,t) = -\frac{1}{r}\frac{\partial}{\partial r}\left(r\Gamma_j(r,t)\right) + S_j(r,t) \quad , \tag{2.3}$$

where Γ_j is the ion radial flux, written in drift-diffusion form

$$\Gamma_j(r,t) = -\frac{\partial}{\partial r}\left(n_j(r,t)D_j(r,t)\right) + \mu_j(r,t)n_j(r,t)E_r(r,t) \quad , \tag{2.4}$$

and S_j is the ion gain/loss term due to kinetic processes. D_j and μ_j are the ion free diffusion coefficient and ion mobility, respectively and E_r is the radial electric field.

The radial population of the excited states is given by [53; 54]

$$\frac{\partial}{\partial t} n_j(r,t) = -\frac{1}{r}\frac{\partial}{\partial r}\left(r\Gamma_j(r,t)\right) + S_j(r,t) \tag{2.5}$$

where $\Gamma_j(r,t) = -D_j(r,t)\frac{\partial}{\partial r}n_j(r,t)$ for non-radiative (metastable) levels, $\Gamma_j = 0$ for radiative levels and S_j is the gain/loss term due to kinetic processes for excited states.

The source terms S_j in balance equations for charged and excited species are determined by collisions occurring in the plasma volume and consist of two contributions: positive, from the collisions in which a particle of species j is created, and negative, from those in which such a particle is lost. Source terms have contributions due to various inelastic collisional and radiation processes. More details will be given in Section 2.5. These terms are proportional to the densities of the reacting particles:

$$S_2(r,t) = k(r,t)n_1(r,t)n_2(r,t) \quad , \tag{2.6}$$

for two-body collisions, and

$$S_3(r,t) = k(r,t)n_1(r,t)n_2(r,t)n_3(r,t) \quad , \tag{2.7}$$

for three-body collisions. The proportionality constant k is the reaction rate coefficient. For spontaneous radiation, the source term is

$$S(r,t) = An(r,t) \quad , \tag{2.8}$$

where A is the decay frequency.

The plasma in the positive column is assumed as an ideal gas. The ground state density n_0 is related to the heavy particle temperature T_h, the mean electron energy U_e and pressure p by the expression

$$n_0(r,t) = \frac{p}{k_B T_h(r,t)} - n_e(r,t)\frac{T_e(r,t)}{T_h(r,t)} - \sum_j n_j(r,t) \tag{2.9}$$

with corresponding "electron temperature" $T_e(r,t) = 2U_e(r,t)/(3k_B)$, where k_B is the Boltzmann constant.

2.1.3 Equation for the mean electron energy

The radially dependent balance equation for mean electron energy is described by using second moment of corresponding 1D electron BE and is written as follows [53; 54]

$$\begin{aligned}\frac{\partial}{\partial t}\big(n_e(r,t)U_e(r,t)\big) = &-\frac{1}{r}\frac{\partial}{\partial r}\big(r\Gamma_\varepsilon(r,t)\big) - e_0\Gamma_z(r,t)E_z(t) \\ &-e_0\Gamma_e(r,t)E_r(r,t) + S_{sc}(r,t) + S_{ci}(r,t) + S_{r3}(r,t) \\ &-S_{el}(r,t) - S_{in}(r,t) - S_{r2}(r,t)\,,\end{aligned} \tag{2.10}$$

where Γ_ε is the electron energy flux in radial direction, e_0 denotes the elementary charge, Γ_z and Γ_e are the electron particle fluxes in axial and radial direction, respectively, and E_z is the axial electric field. The electron energy flux Γ_ε is given by the drift-diffusion approach

$$\Gamma_\varepsilon(r,t) = -\mu_\varepsilon(r,t)n_e(r,t)E_r(r,t) - \frac{\partial}{\partial r}\big(D_\varepsilon(r,t)n_e(r,t)\big)\,, \tag{2.11}$$

where μ_ε and D_ε are the mobility and diffusion coefficient of electron energy transport. The term $-e_0\Gamma_z E_z$ in (2.10) describes the power gain from the axial electric field (Joule heating) whereas the term $-e_0\Gamma_e E_r$ represents the power

loss due to the retarding of the electron movement towards the wall (radial cooling). S_{sc}, S_{ci} and S_{r3} are the power gain rates in superelastic electron collisions, chemo-ionization processes and three-body recombination, respectively. S_{el} and S_{in} denote the power loss rates due to elastic collisions and inelastic collision processes leading to excitation and ionization. The power loss rate caused by electron-ion recombination in two-body collisions is represented by S_{r2}. These terms are given by [55–58]

$$
\begin{aligned}
S_{sc}(r,t) &= n_e(r,t)\sum_j n_j(r,t)\sum_l U^{sc}_{j,l}k^{sc}_{j,l}\,, && (2.12)\\
S_{ci}(r,t) &= \sum_p n^{(1)}_p(r,t)n^{(2)}_p(r,t)k_pU^{ci}_p\,, && (2.13)\\
S_{r3}(r,t) &= n_e(r,t)n_e(r,t)\sum_q n_q(r,t)k_qU_q\,, && (2.14)\\
S_{el}(r,t) &= n_e(r,t)\sum_j n_j(r,t)K^{el}_j\,, && (2.15)\\
S_{in}(r,t) &= n_e(r,t)\sum_j n_j(r,t)\sum_m U^{in}_{j,m}k^{in}_{j,m}\,, && (2.16)\\
S_{r2}(r,t) &= n_e(r,t)\sum_i n_i(r,t)k_iU_e\,, && (2.17)
\end{aligned}
$$

where the rate coefficient [53; 54]

$$
K^{el}_j = 2\frac{m_e}{m_j}\sqrt{\frac{2}{m_e}}\int_0^\infty U^2Q^d_j(U)\left(f_0(U)+k_BT_h\frac{\mathrm{d}}{\mathrm{dU}}f_0(U)\right) \qquad (2.18)
$$

for power dissipation in elastic collisions with species j of mass m_j has been introduced. Here Q^d_j is the cross section for momentum transfer in elastic collisions with species j. U^{ci}_p in (2.13) is the energy difference between two excited atoms and the ion, and U_q in (2.14) represents the energy difference between the ion and the resulting excited atom level.

2.1.4 Equation for the enthalpy of the heavy particles

The radially dependent balance equation for the heavy particle enthalpy is deduced from second moment of heavy particle BE and written as following [53; 54]

$$\frac{\partial}{\partial t}\left(\frac{5}{2}N(r,t)k_B T_h(r,t)\right) = \frac{1}{r}\frac{\partial}{\partial r}\left(r\lambda_h(T_h)\frac{\partial}{\partial r}T_h(r,t)\right) + S_{el}(r,t)\,, \tag{2.19}$$

where λ_h is thermal conductivity. The first term on the right-hand side in Eq. (2.15) represents heat conduction. The influence of convection on heavy particle temperature distribution is neglected. Eq. (2.15) is written in assumption, that inelastic collisions do not contribute in heavy particle power budget and heavy particles gain energy only due to elastic collisions with electrons.

2.2 Equations for the electric field

2.2.1 Poisson's equation

The self-consistent treatment of charged particles transport is guaranteed by coupling of above fluid equations with Poisson's equation. The radial electric field E_r is strongly depended on internal charge particles separation. The radial electric field writes

$$E_r = -\frac{\partial \Phi}{\partial r} \quad , \tag{2.20}$$

where Φ is the corresponding radial potential and calculated by using Poisson's equation

$$-\frac{1}{r}\frac{\partial}{\partial r}\left(r\frac{\partial}{\partial r}\Phi(r,t)\right) = \frac{e_0}{\varepsilon_0}\sum_i Z_i n_i(r,t)\,, \tag{2.21}$$

where ε_0 is the vacuum permittivity.

2.2.2 Current balance

Axial electric field is calculated using current balance

$$E_z(t) = \frac{I(t)}{2\pi e_0 \int_0^R \mu_e(r,t) n_e(r,t) r \mathrm{d}r}\,, \tag{2.22}$$

where I_0 is electric current.

2.3 Description of electron kinetic properties

For the solution of the particle and power balance equation of the electrons, their transport and rate coefficients have to be known. In the present work, different assumptions concerning the EVDF have been adapted.

In the standard fluid model, the transport and rate coefficients of the electrons are obtained from the solution of the 0D BE for the EVDF [59]. Details are presented in Appendix B.

To evaluate the impact of the electron transport and rate coefficients, further calculations using the Maxwellian distribution [54]

$$f_0^{\mathrm{M}}(U) = \frac{2}{\sqrt{\pi}} \left(\frac{3}{2U_e}\right)^{3/2} \exp\left(-\frac{3}{2}\frac{U}{U_e}\right) \tag{2.23}$$

as well as the Druyvesteyn distribution [54]

$$f_0^{\mathrm{D}}(U) = \frac{2\left(\Gamma(\frac{5}{4})\right)^{3/2}}{\left(\Gamma(\frac{3}{4})\right)^{5/2}} U_e^{-3/2} \exp\left(-\left(\frac{U}{U_e}\frac{\Gamma(\frac{5}{4})}{\Gamma(\frac{3}{4})}\right)^2\right) \tag{2.24}$$

for the determination of these properties have been performed with

$$f_1^{\mathrm{M,D}}(U) = \frac{E_z}{N}\frac{e_0}{Q_{\mathrm{eff}}}\frac{\mathrm{d}}{\mathrm{d}U} f_0^{\mathrm{M,D}}(U) \tag{2.25}$$

according to the two-term approximation of the EVDF expansion in Legendre polynomials [60; 61].

2.4 Boundary conditions

In order to solve the equations (2.1), (2.3), (2.5), (2.10), (2.19) and (2.21), knowledge of the boundary conditions is required at each time. Due to rotational symmetry the boundary conditions at the tube axis corresponding to the radial position $r = 0$ are

$$\begin{aligned} &\frac{\partial}{\partial r} n_j(0,t) = 0, \quad \frac{\partial}{\partial r}\big(n_e(0,t)U_e(0,t)\big) = 0, \\ &\frac{\partial}{\partial r} T_h(0,t) = 0, \quad \frac{\partial}{\partial r}\Phi(0,t) = 0. \end{aligned} \tag{2.26}$$

for the densities n_j of excited and charged particles, the mean electron energy density $n_e U_e$, the heavy particle temperature T_h and the radial electric potential Φ. In addition, zero radial potential is adjusted at the tube axis when solving the Poisson equation (2.21).

According to [62], the boundary conditions for the particle balance equations at the tube wall corresponding to the radial position $r = R$ are

$$\Gamma_j(R,t) = \frac{1-b_j}{1+b_j}\Big[(2a_j-1)\mathrm{sgn}(Z_j)\mu_j(R,t)\times E_r(R,t)n_j(R,t) + \frac{1}{2}v_{th,j}(R,t)n_j(R,t)\Big]. \tag{2.27}$$

Here b_j is the fraction of particles reflected from the surface and $v_{th,j} = \sqrt{\frac{8k_BT_j}{\pi m_j}}$ denotes the thermal velocity of the species j. The parameter a_j is set to one if the drift velocity $\mathrm{sgn}(Z_j)\mu_j E_r \mathbf{e}_r$ is directed towards the wall and to zero otherwise, where $\mathbf{e}_r$ is the normal vector pointing towards the surface. In present work, the reflection coefficients $b_e = 0.9$ for electrons, $b_i = 0.01$ for ions and $b_m = 0.33$ for metastable atoms were used [53; 63].

To solve the power balance equation (2.10) of the electrons the electron energy flux at the tube wall was calculated similarly [62; 64] and the corresponding relation reads

$$\Gamma_\varepsilon(R,t) = \frac{1-b_e}{1+b_e}\Big[\mu_\varepsilon(R,t)n_e(R,t)E_r(R,t) + \frac{2}{3}v_{th,e}n_e(R,t)U_e(R,t)\Big]. \tag{2.28}$$

The heavy particle temperature at the tube wall $T_h(R,t)$ has been assumed to be 300 K for argon and 350 K for xenon at each time.

2.5 Collisional-radiative model

2.5.1 Argon

For the argon discharge the following species are considered in the collisional-radiative model: ground state atom Ar, three excited levels Ar*(m), Ar*(r), and

$Ar^*(4p)$, two excimers $Ar_2^*(3)$ and $Ar_2^*(1)$, the ions Ar^+ and Ar_2^+ as well as electrons e. The excited states are "effective" levels in which different states have been united: the two metastable states ($1s_5$ and $1s_3$) combined into the $Ar^*(m)$ state, the two resonance states ($1s_4$ and $1s_2$) lumped into the $Ar^*(r)$ state and $Ar^*(4p)$ is the sum of the ten 4p levels. 28 electron and heavy particle collision processes and 5 radiative transitions are taken into account. A schematic of the argon levels is shown in Fig. 2.2 and the processes included in the collisional-radiative model are listed in Tab. A.1.

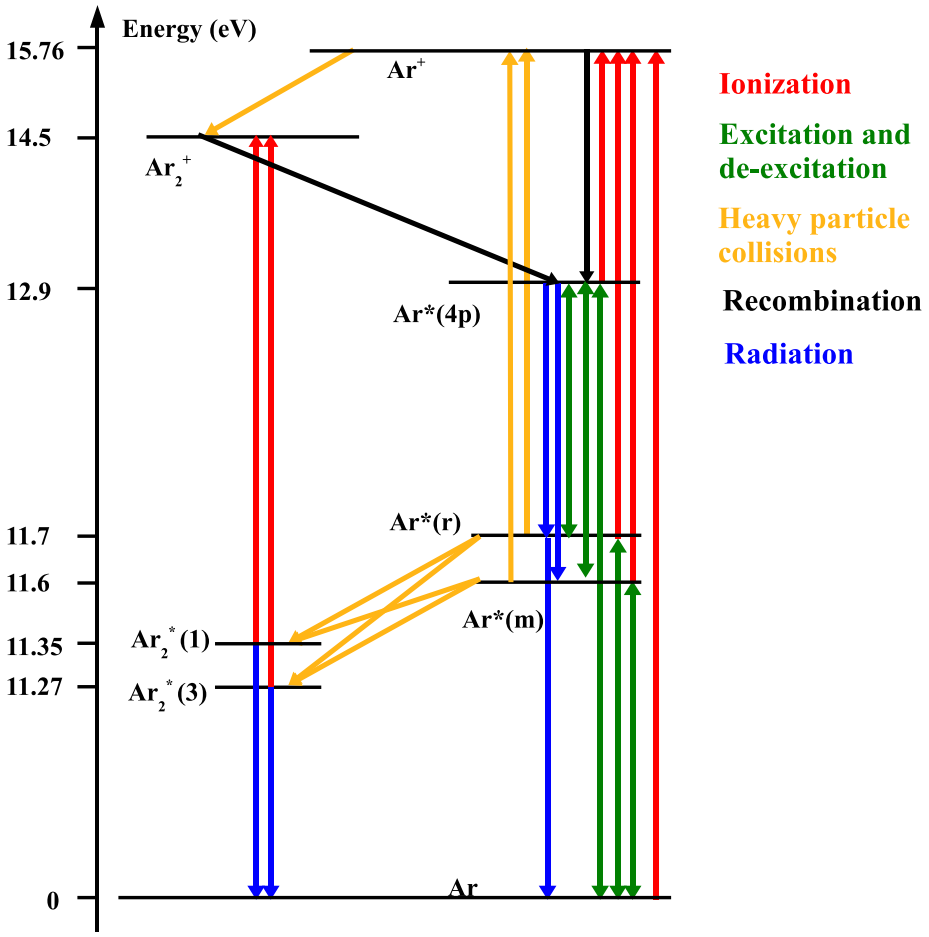

Figure 2.2: Argon collisional-radiative model.

The atomic data for electron-atom collisions have been taken from the liter-

ature. The momentum transfer cross section for elastic electron-atom collisions of Ref. [65] has been used in the calculations. Cross sections for electron impact excitation of ground state atoms up to 30 eV and among excited states up to 20 eV have been described using the theoretical data set from Ref. [66], which was obtained by calculations using the Breit-Pauli R-matrix method. For higher electron energies data sets of Hayashi [67] for excitation from the ground state and Born approximation for excitation between excited states has been used. The cross sections for de-excitation in electron collisions have been obtained according to the principle of detailed balancing. For ground state ionization of argon atoms the cross section data of Ref. [68] has been applied. The electron impact cross sections for stepwise ionization have been obtained according to the Deutsch-Märk formalism [69]. The ionization of excimers has been treated using data from Ref. [70]. Cross sections have been used to determine the transport and the rate coefficients of the electrons as described in Appendix B. These transport and rate coefficients have been used in model as functions of U_e, T_h and n_e/N.

Three-body recombination of argon ions in electron collisions has been described using the rate coefficient given in [9]. The dissociative electron-molecular ion recombination has a large importance for the constriction in inert gas plasmas due to its strong dependence on the mean electron energy. At higher pressures vibrational excitation of molecular ions also becomes important for this process. This can be expressed by a functional dependence on the heavy particle temperature. Therefore, the rate coefficient for dissociative electron-molecular ion recombination of [71] has been used.

The main source of the molecular argon ions is ion conversion from atomic ions. This process has considerable impact at higher pressure due to the square dependence on the ground state population. The ion conversion rate coefficient of [72] has been used. The excimers are produced due to neutral association of metastable and resonance states with ground state atoms. These processes have been treated using data from Ref. [9]. Chemo-ionization processes of excited levels were additionally taken into account by applying the rate coefficients of Ref. [73].

Radiative transitions from different argon levels have been included in the model. For higher pressure, the plasma cannot be assumed to be optically thin

for the transition from $Ar^*(r)$ into the ground state ($\lambda_0 = 106$ nm). This process of resonance radiation trapping was described by an effective lifetime according to Holstein's theory for a cylindrical plasma [74]. The transition probability for the trapped radiation A_{eff} becomes

$$A_{eff} = 0.196 A \sqrt{\frac{\lambda_0}{R}} \quad , \tag{2.29}$$

where A is the transition probability (untrapped), R is the tube radius, and λ_0 is the transition wavelength. For all other optically allowed transitions the natural lifetimes from Refs. [75; 76] have been used.

The mobility of atomic ions has been given by the functional form in [77] depending on the reduced electric field E_z/N and the mobility of molecular ions has been taken from Ref. [78]. The diffusion coefficients of the atomic and molecular ions have been calculated using the Einstein relation [1] with the heavy particle temperature T_h. The diffusion coefficient of the metastable argon atoms has been taken from the relation $ND_m = 1.738 \times 10^{18} \mathrm{cm}^{-1}\mathrm{s}^{-1}$ in accordance with [79]. In the present studies the following value of the thermal conductivity for argon $\lambda_h = 4.17 \times 10^{-6} T_h^{2/3}$ W cm^{-1} K$^{-5/3}$ [3] has been used.

2.5.2 Xenon

For the xenon medium pressure discharge in the collisional-radiative model the following species are considered: ground state atom Xe, seven excited levels $Xe^*(1s_5)$, $Xe^*(1s_4)$, $Xe^*(1s_3)$, $Xe^*(1s_2)$, $Xe^*(2p_{10})$, $Xe^*(2p_{9..5})$, and $Xe^*(2p_{4..1})$, two relaxed lowest vibrational state excimers $Xe_2^*(1)$, $Xe_2^*(3)$, and two higher vibrational state excimers $Xe_2^*(1v)$, and $Xe_2^*(3v)$, three ions Xe^+, Xe_2^+, and Xe_3^+, and electrons e. The following excited states are "effective": $Xe^*(2p_{9..5})$ and $Xe^*(2p_{4..1})$ in which different states have been lumped together. 76 electron end heavy particle collision processes and 12 radiative transitions are taken into account. A scheme of the xenon levels is shown in Fig. 2.3 and the processes included in the collisional-radiative model are listed in Tab. A.2.

The atomic data for electron-atom collisions have been taken from the literature. Elastic electron collision processes are considered with xenon atoms. The momentum transfer cross section for elastic electron-atom collisions up to 30 eV

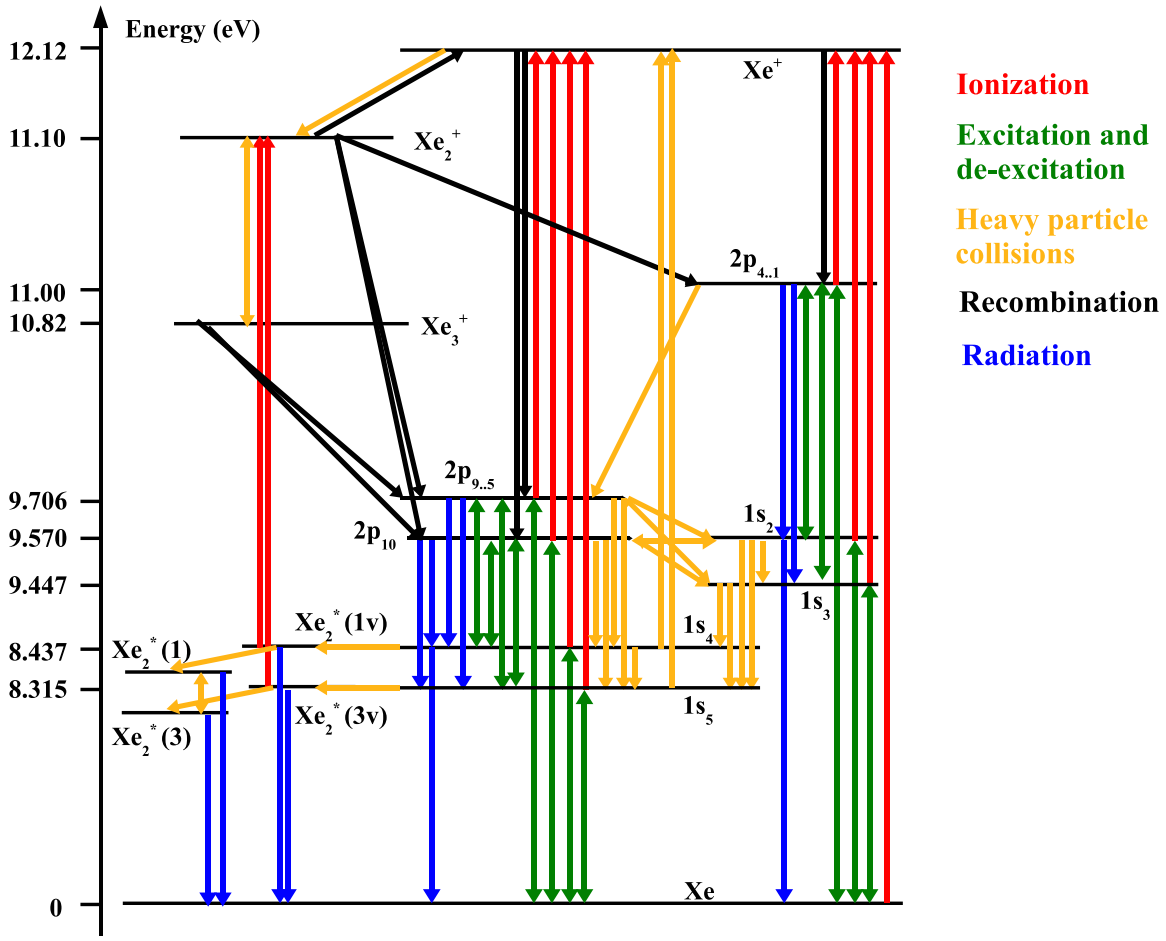

Figure 2.3: Xenon collisional-radiative model.

[80] and for higher electron energies [81] have been used in the calculations. Cross sections for electron impact excitation of ground state atoms up to 30 eV from data set of Nakazaki *et al.* [82], obtained with the Breit-Pauli R-matrix method, have been chosen. For higher energies data set of Puech *et al.* [83] has been used. Cross sections for electron impact excitation among excited states, i.e., for transitions from the four lowest-lying s levels to the p levels, have been calculated according Vriens and Smeets [84]. However, the data calculated in such way seem to overestimate the cross sections. To ensure better agreement with experimental results the data calculated by the Vriens and Smeets formula and

additionally dimished by a factor of 0.4 have been adopted in the model. The cross sections for de-excitation have been obtained according to the principle of detailed balancing. For ground state ionization of xenon atoms the cross section data of Ref. [85] has been applied. The electron impact cross sections for stepwise ionization have been obtained according to the Deutsch-Märk formalism [69]. In order to obtain better agreement with experimental data the stepwise ionization cross section have been enlarged by a factor of 10. Cross sections have been used to determine the transport and the rate coefficients of the electrons as described in Appendix B. These transport and rate coefficients have been used in model as functions of U_e, T_h and n_e/N.

The ionizations of excimers has been treated using data from Ref. [86]. Molecular ion-atomic ion conversion by electron impact has been described using the cross section given in [87]. The outcome from three-body e/Xe^+, dissociative e/Xe_2^+ and e/Xe_3^+ recombination [88–90] is distributed amongst high-lying Xe(2p) levels according to their statistical weights.

The model includes the quenching kinetics for xenon high-lying excited levels in collisions with xenon ground state atoms. Quenching rate coefficients have been taken from works by Alford [91] and by Nelson *et al.* [92]. Molecular ion formation by heavy particle impact has considerable importance at elevated pressures. The rate coefficient has been estimated using experimental and theoretical data presented in [93]. The formation of the Xe_3^+ by heavy particle impact and reverse reaction have been treated according to [94]. The excimers $Xe_2^*(3v)$ and $Xe_2^*(1v)$ are produced due to three-body reaction of metastable $Xe^*(1s_5)$ and $Xe^*(1s_4)$ resonance levels with ground state atoms. These processes have been treated using data from [95; 96]. The quenching for xenon low-lying excited levels and excimers in collisions with xenon ground state atoms have been treated in accordance with [96; 97]. The electron production due to chemoionization is described by taking into account collisions between xenon low-lying excited levels. The rate coefficients are estimated according to Ref. [73]. Additionally, a functional dependence on the heavy particle temperature has been introduced for three-body reactions and dissociative recombination reactions according to [98; 99].

The model includes the radiative transitions between different atomic and molecular xenon levels. For elevated pressure, the plasma cannot be assumed to be optically thin for the transition from $Xe^*(1s_4)$, $Xe^*(1s_2)$ into the ground state ($\lambda_0 = 147$ nm, 129.6 nm). This process of resonance radiation trapping was described by an effective lifetime according to Holstein's theory for a cylindrical plasma [74] (see Eq. 2.29). For all other optically allowed transitions the natural lifetimes from Refs. [96; 100] have been used.

The mobilities of Xe^+ and Xe_2^+ have been taken from [101]. The mobility of Xe_3^+ is assumed to be the same as that of Xe_2^+. The diffusion coefficients of the atomic and molecular ions have been calculated using the Einstein relation [1] with the heavy particle temperature T_h. Diffusion coefficients for the diffusion of metastable xenon atoms in xenon have been taken from Ref. [102]. In the present studies the following value of the thermal conductivity for xenon $\lambda_h = 1.35 \times 10^{-4}(T_h/800)^{0.69}\ \mathrm{W\,cm^{-1}\,K^{-1}}$ [103] has been used.

3 Numerics

In this chapter, the numerical approach is presented which was used to solve the system of fluid equations derived in the previous chapter. In order to solve partial differential equations, the finite difference method has been applied, where all quantities are represented by their values at a discrete set of points in space and time. This approach incorporates the exponential formulation for spatial gradient terms, and an implicit algorithm to advance equations in time. Details about discretization of the model equations and solving of the discretized equations were shown.

3.1 Finite difference method

The system of fluid equations can be solved by using numerical discrete method. The main idea of the method is dividing physical spatial continuum $D(r)$ into a set of discrete finite points i called *computational mesh* or *grid*. The discretization procedure is the approximation of the set of partial differential equations in each discrete point by a set of equations describing, at each time, the various physical variables at different points within the region D. In contrast to analytical methods, the numerical discretization gives a solution in a finite number of points, only.

In this work the **finite difference method** (FDM) of discretization has been adapted [104]. This method approximates the solution to differential equation by replacing derivative expressions with approximately equivalent difference quotients. One-dimensional nonuniform grid has been used, along r direction. The

mesh is represented by n points in space. In order to describe the expected large density gradients the grid is finer near the centre of the discharge and near the wall. The part of the nonuniform grid is shown in Fig. 3.1. Let the r-positions of the grid points be referred by subscript, where $r_{i+1} = r_i + h_p$ and $r_{i-1} = r_i - h_m$. All scalar physical quantities are evaluated at the grid points r_i, and all vector variables, i.e., fluxes, radial field are evaluated exactly midway between grid points $r_{i+1/2}$. The value of the scalar variable midway between grid points is taken to be the average of its values at the points: $r_{i+1/2} = (r_{i+1} + r_i)/2$.

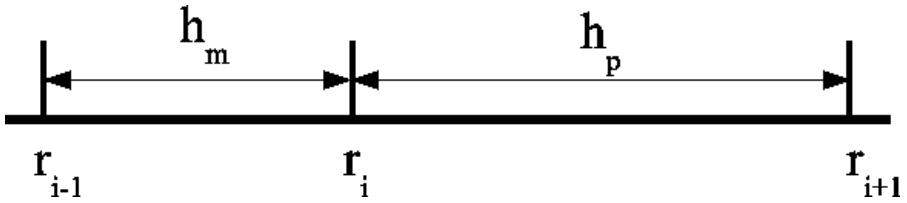

Figure 3.1: The part of the nonuniform grid.

According to the FDM, the first derivatives can be derived from a truncated Taylor series. Assuming the function whose derivatives are to be approximated is properly behaved, by Taylor's theorem,

$$f(r_i + h_p) = f(r_i) + \frac{f'(r_i)}{1!}h_p + \frac{f^{(2)}(r_i)}{2!}(h_p)^2 + ... + \frac{f^{(n)}(r_i)}{n!}(h_p)^n + R_n(r), \quad (3.1)$$

where $n!$ denote the factorial of n, and $R_n(x)$ is a reminder term, denoting the difference between the Taylor polynomial of degree n and the original function. Again using the first derivative of the function f as an example, by Taylor's theorem,

$$f(r_i + h_p) = f(r_i) + f'(r_i)h_p + R_1(r) \qquad , \quad (3.2)$$

which for $R_1(r)$ sufficiently small, is equivalent to

$$f'(r_i) \approx \frac{f(r_i + h_p) - f(r_i)}{h_p} \qquad \text{(FD)}. \quad (3.3)$$

Relation (3.3) is so-called forward-difference (FD) expression. In same way one can derive backward-difference (BD) and centred-difference (CD) expressions.

$$f'(r_i) \approx \frac{f(r_i) - f(r_i - h_m)}{h_m} \qquad \text{(BD)}. \quad (3.4)$$

$$f'(r_i) \approx \frac{h_m}{h_m + h_p} \frac{f(r_i + h_p) - f(r_i)}{h_p} + \frac{h_p}{h_m + h_p} \frac{f(r_i) - f(r_i - h_m)}{h_m} \qquad \text{(CD)}. \tag{3.5}$$

The one source of error in FDM is truncation error, the difference between the exact solution of the finite difference equation and the exact quantity assuming perfect arithmetic. The *order* of an algorithm refer to the highest power of expansion parameter that is truncate in the solution method. Consequently, the FD and BD expressions are only first-order, while CD is second-order accurate. In present work CD expressions have been used to discretize the first derivatives in space, except treatment of boundary conditions, where BD or FD treatment has been applied.

For expression of the second derivative in space one can use second-order CD relation. For example, the second radial derivative of variable f at point i can be written as

$$f''(r_i) \approx \frac{h_m \cdot f(r_i + h_p) - (h_p + h_m) \cdot f(r_i) + h_p \cdot f(r_i - h_m)}{0.5 \cdot h_p \cdot h_m \cdot (h_p + h_m)} \quad . \tag{3.6}$$

3.2 Explicit, implicit numerical schemes

Choice of an appropriate time step is particularly important, since the using high Δt can lead to solution oscillation or divergence. When solving the system of fluid equations, one can use different procedures to advance the equation system in time: *explicit* or *implicit*.

Let upper indices refer to a moment in time, and let Δt to be a time step, with $t^{k+1} = t^k + \Delta t$. To show the difference between explicit and implicit procedures the electron balance equation (2.1) is considered

$$\frac{\partial n_e}{\partial t} = -\frac{1}{r} \frac{\partial (r \Gamma_{er})}{\partial r} + S_e \quad .$$

Using a FD expression to discretize the time derivative term, the electron balance equation is written as:

$$n_e^{k+1} - n_e^k = f(t^k) \Delta t \quad , \tag{3.7}$$

where the flux and source term (in above example included in function f) are calculated at time t^k. Equation (3.7) corresponds to the **explicit** or forward time

integration scheme, where flux and source term are evaluated using the solutions values received at an earlier time t^k.

If the flux and source term are obtained at time t^{k+1}, one receives

$$n_e^{k+1} - n_e^k = f(t^{k+1})\Delta t \qquad , \tag{3.8}$$

corresponding to the **implicit** or backward time-integration scheme.

Explicit evaluation is computationally attractive, but it can lead to numerical oscillations or even divergence for large Δt. Implicit scheme is numerically stable, but it can be very hard to realize: the coupling between different equations and nonlinearities can make implicit evaluation quite heavy or impossible. In this work, densities, mean electron energy and heavy particle temperature in transport terms are always evaluated implicitly, because the explicit treatment would lead to very strong time step constraints due to the fundamental necessary condition for the convergence of difference methods, known as Courant-Friedrich-Lewy (CFL) condition [105]. In particular, to determine the particle densities n_j^{k+1}, the mean electron energy density $(n_e U_e)^{k+1}$ and the heavy particle temperature T_h^{k+1} at the time $t + \Delta t$, the respective property has been approximated by its value at the time $t + \Delta t$ in the corresponding equation, while the rate and transport coefficients as well as the further properties have been estimated by their values at time t.

3.3 Spatial discretization of the transport equations

The flux term in the balance equation for the densities and the mean electron energy is discretized using CD scheme as follows:

$$(\nabla \cdot \Gamma)_i = -\frac{1}{r_i} \frac{(r\Gamma)_{i+1/2} - (r\Gamma)_{i-1/2}}{\Delta r} \qquad . \tag{3.9}$$

In order to describe the expected large density gradients, for the density and energy flux, all having the same drift-diffusion form, the Scharfetter-Gummel exponential scheme is used [106]. It is based on the analytical solution for a constant drift-diffusion flux between two grid points. The flux at half-point position can

be written as

$$\Gamma_{i+1/2} = \frac{1}{r_{i+1} - r_i} D_{i+1/2} \left(f_1 \left(z_{i+1/2} \right) n_{i+1} + f_2 \left(z_{i+1/2} \right) n_i \right) \quad , \tag{3.10}$$

with

$$z_{i+1/2} = -\frac{\mathrm{sgn}(Z)\mu_{i+1/2}(\Phi_{i+1} - \Phi_i)}{D_{i+1/2}} \quad , \tag{3.11}$$

and the functions $f_1(z)$, $f_2(z)$ defined as

$$f_1(z) = \frac{z}{1 - \exp(z)} \quad , \tag{3.12}$$

$$f_2(z) = \frac{z}{1 - \exp(-z)} \quad , \tag{3.13}$$

for $z \neq 0$, and $f_1(0) = -1$, $f_2(0) = 1$.

After the substitution of the exponential scheme for the flux, the discretized balance equation has the form of a three-point equation for the density:

$$A_i n_{i-1} + B_i n_i + C_i n_{i+1} = R_i \tag{3.14}$$

a set of linear equations that relates the density in a grid point to the densities in the two neighboring grid points. The left, right, central and source coefficients of equation (3.14) are given by

$$A_i = -\frac{r_l \cdot h_p}{0.5 \cdot r_i \cdot h_p \cdot h_m \cdot (h_p + h_m)} D_{i-1/2} f_2 \left(z_{i-1/2} \right) \quad , \tag{3.15}$$

$$C_i = \frac{r_r \cdot h_m}{0.5 \cdot r_i \cdot h_p \cdot h_m \cdot (h_p + h_m)} D_{i+1/2} f_1 \left(z_{i+1/2} \right) \quad , \tag{3.16}$$

$$B_i = \frac{1}{\Delta t} - A_i - C_i \quad , \tag{3.17}$$

$$R_i = \frac{n_i}{\Delta t} + S_i \quad , \tag{3.18}$$

respectively, where $r_l = r_i - 0.5 \cdot (r_i - r_{i-1})$ and $r_r = r_i + 0.5 \cdot (r_{i+1} - r_i)$.

The three-point coefficients (3.15), (3.16), (3.17), (3.18) apply at every grid points of the computational mesh. At the boundaries, the three-points coefficients include the boundary condition (2.27) and (2.28). For example, the boundary conditions for the electron density flux is discretized as

$$(\Gamma \cdot \mathbf{n})_i = \frac{1 - b_e}{1 + b_e} \left[-(2a_e - 1)\mu_i E_{r,i-1/2} n_i + \frac{1}{2} V_{th,i} n_i \right] \quad , \tag{3.19}$$

on a right boundary point. Substitution of this relation in the discretized balance equation gives the following three-point coefficients for a right boundary point n:

$$A_n = -\frac{1}{r_n - r_{n-1}} D_{e,n-1/2} f_1(z_{n-1/2}) \quad , \tag{3.20}$$

$$B_n = -\frac{1}{r_n - r_{n-1}} D_{e,n-1/2} f_2(z_{n-1/2}) \quad , \tag{3.21}$$

$$C_n = 0 \quad , \tag{3.22}$$

$$R_n = \frac{1 - b_e}{1 + b_e} \left(-(2a_e - 1)\mu_{e,n} E_{r,n-1/2} n_{e,n} + 0.5 V_{th,n} n_{e,n} \right) \quad . \tag{3.23}$$

3.4 Poisson-transport coupling

The electric potential profile is calculated by solving Poisson's equation

$$-\Delta\Phi = \frac{e_0}{\varepsilon_0} \left(\sum_j Z_j n_j - n_e \right) \quad , \tag{3.24}$$

knowing the updated profiles of charged densities. The coupling between charge densities balance equations and the electric potential has strong constraint on the electron dielectric relaxation time

$$\tau_M = \frac{\varepsilon_0}{\sum_j Z_j e_0 \mu_j n_j} \quad , \tag{3.25}$$

where Z_j, μ_j and n_j are the particle charge number, mobility, and density, respectively. If the potential in the density flux term is treated explicitly, the stability of numerical solution requires that $\Delta t < \tau_M$ [107]. This constraint can be a strong limitation at high plasma densities and/or pressure. One can evaluate electron potential implicitly to avoid this time step restriction, but such procedure become too cumbersome and also leads to a strong increase of the total computation time [108]. To circumvent this time step limitation, a semi-implicit procedure has been adapted in this thesis [109]. In particular, Poisson's equation (3.24) has been solved for the potential Φ^{k+1} at time $t + \Delta t$ using the densities n_j^k and transport coefficients μ_j^k and D_j^k at time t to estimate the charge carrier

density at time $t + \Delta t$. The densities $\tilde{n}_j^{k+1}$ at time $t + \Delta t$ have been expressed as following:

$$\tilde{n}_j^{k+1} = n_j^k - \Delta t \nabla \Gamma_j^{k+1} + S_j^k \Delta t \quad , \tag{3.26}$$

where

$$\Gamma_j^{k+1} = \mathrm{sgn}(Z_j)\mu_j^k n_j^k (-\nabla\Phi)^{k+1} - D_j^k \nabla n_j^k \quad . \tag{3.27}$$

Substitution of the estimated charge densities (3.26) into Poisson's equation after some algebra yields

$$-\Delta\Phi^{k+1} - \Delta t \frac{e_0}{\varepsilon_0} \sum_j \mu_j^k n_j^k \Delta\Phi^{k+1} = \frac{e_0}{\varepsilon_0} \sum_j \mathrm{sgn}(Z_j) n_j^k + \Delta t \frac{e_0}{\varepsilon_0} \Delta \sum_j \mathrm{sgn}(Z_j) n_i^k D_j^k \quad . \tag{3.28}$$

Notice, that the source terms S_j eliminate each other. Using this semi-implicit procedure, the time step can be 10-100 times greater than the electron dielectric relaxation time, thus give a drastic speedup of the computation.

Current balance equation is solved for the axial electric field E_z^{k+1} at time $t + \Delta t$ using the electron mobility at time t and the electron density n_e^{k+1} at time $t + \Delta t$

$$E_z^{k+1} = \frac{I_z}{2\pi e_0 \int_0^R (\mu_e(r))^k (n_e(r))^{k+1} r \mathrm{d}r} \quad . \tag{3.29}$$

The integral is calculated by use of a trapezoid rule.

3.5 Time integration of the system of equations

The model uses an efficient method to advance system of the equations in time in order to reach a steady-state solution or to describe temporal evolution of the pulsed discharge. The partial differential equations are solved successively as shown in the flow chart of the fluid model in Fig. 3.2. To take into account possible deviation from a Maxwellian energy spectrum for the electrons a set of look-up tables (LUTs) have been constructed, where electron transport and rate coefficients depend on the mean electron energy U_e, heavy particle temperature T_h, and ionization ratio n_e/N (see more detail in Section 2.3).

Time integration starts at $t = 0$ from an appropriate set of initial conditions. Iterations proceed at discrete time step intervals Δt. Input discharge parameters

are tube radius R, discharge current I_0 and total gas pressure p. Typical initial conditions correspond to charged particle densities of about 10^9 - 10^{12} cm^{-3}, excited particle densities of about 10^6 - 10^8 cm^{-3}, an electron mean energy of about 2 eV, heavy particle temperature 300 - 3000 K, axial electric field 10 V/cm and a constant zero potential profile.

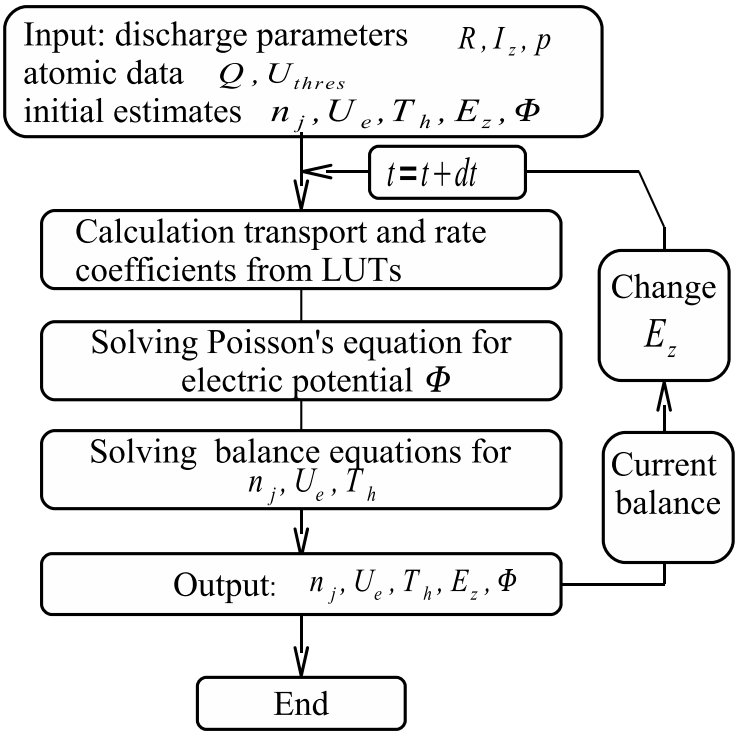

Figure 3.2: Flowchart of the numerical solution.

The time loop starts by using the values of the charged particle densities to solve Poisson's equation according to (3.28) and to obtain the radial electric potential distribution in the discharge at the time $t + \Delta t$. This electric potential profile as well as the transport and rate coefficients depending on the spatial position are used to determine the charged and neutral particle densities, the electron mean energy, the heavy particle temperature, the related particle and electron energy fluxes and the axial electric field at $t + \Delta t$. Details related to the time- and spatial discretization of the model equations and numerical parame-

ters are given in Appendix C. The discrete counterparts of the equations (2.1), (2.3), (2.5) and (2.9) have been solved together by use of a band algorithm [104]. The equations (2.10), (2.19), and (2.21) have been solved separately by use of a tridiagonal algorithm [104]. New value of the axial electric field is computed, according to current balance (2.22) and time loop is repeated.

3.6 Convergence criterion

For steady-state problem numerical iteration stops if convergence criterion is met. Each balance equation have gain and loss terms. Divergence of the flux can be gain or loss, depending on the radial position. Convergence criterion is satisfied if the absolute value of the ratio between gain and loss terms is smaller than 0.1 %. Calculation of the ratio is performed at each inner mesh point and at each time step.

4

Results of the constriction of the dc positive column in argon

The spatial behaviour of the positive column of a dc argon discharge has been studied at pressures between 100 and 500 Torr, currents from 0.6 to 70 mA, and a discharge tube radius $R = 1$ cm using the temporal relaxation method described previously.

4.1 Parametric study

In the following, results of model calculations for dc discharges at pressures $p =$ 100 Torr and $p = 500$ Torr, and different discharge currents I are presented using the standard fluid model. In particular, the model uses the transport and rate coefficients of the electrons as functions of the mean electron energy, gas temperature and ionization degree. Details about determining are given in Appendix B.

Fig. 4.1a illustrates the radial distributions of the normalized electron density for argon at $p = 100$ Torr and discharge currents between 2 and 70 mA. For currents up to about 4 mA the discharge is in diffuse mode and the density profile is close to a Bessel function of zero order. The discharge passes into the constricted mode at currents between 4 and 6 mA. For $I > 6$ mA the discharge is characterized by almost the same narrow normalized electron density profile as for $I = 70$ mA.

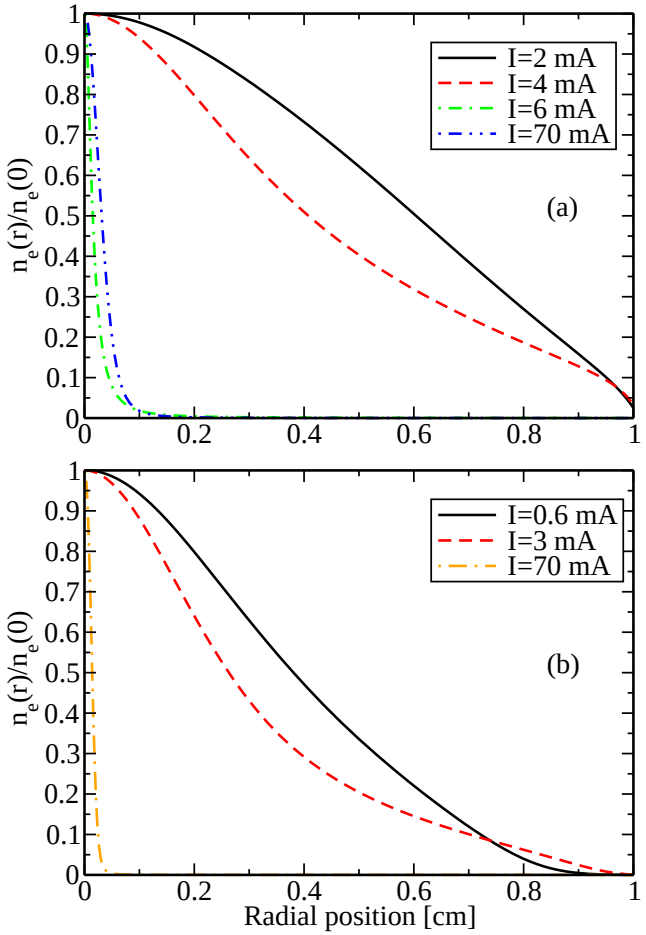

Figure 4.1: Radial profiles of the normalized electron density for argon at $p = 100$ Torr (a), at $p = 500$ Torr (b), and different discharge currents.

Fig. 4.1b shows the radial distributions of the normalized electron density for argon at $p = 500$ Torr and discharge currents between 0.6 and 70 mA. A very similar behaviour in the radial variation of the normalized electron density is observed for the two pressures of 100 and 500 Torr. An increase of pressure leads to more narrow normalized radial profile of the electron density.

Fig. 4.2a illustrates the radial distributions of the heavy particle temperature for argon at $p = 100$ Torr and discharge currents between 2 and 70 mA. The heavy particle temperature deviates from room temperature in the entire discharge region even for the lowest current of $I = 2$ mA considered. In the diffuse mode the

current increase leads to a growth of the heavy particle temperature in the entire discharge region. During the transition to the constricted mode the temperature changes its shape towards a Gaussian-like profile while the absolute values decrease because of reduced global power input. Starting at about 6 mA the temperature increases again with growing current where the enlargement takes place much more in the discharge center than in outer regions.

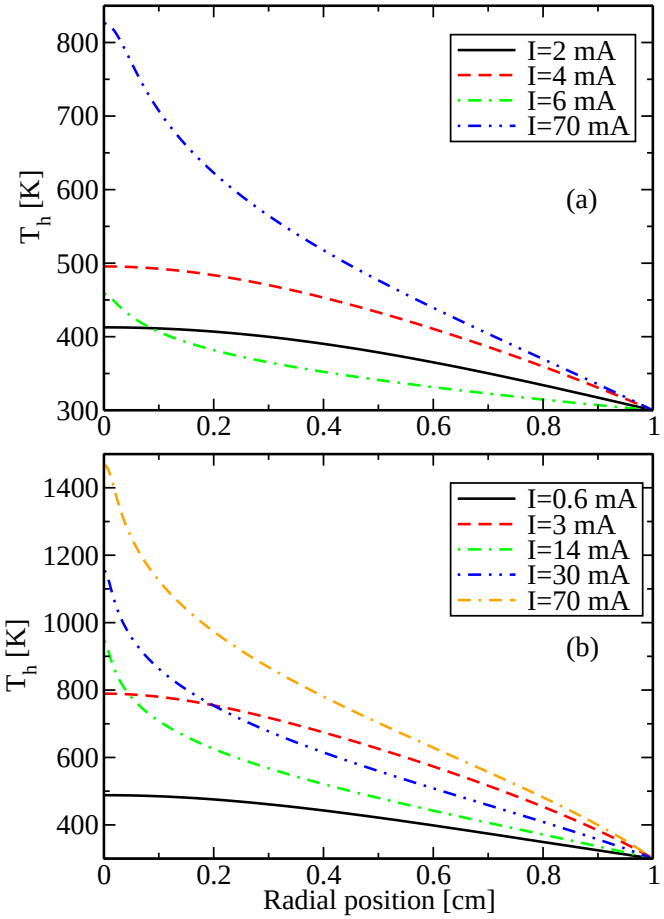

Figure 4.2: Radial profiles of the heavy particle temperature for argon at $p =$ 100 Torr (a), at $p = 500$ Torr (b), and different discharge currents.

Fig. 4.2b shows the radial distributions of the heavy particle temperature for argon at $p = 500$ Torr and discharge currents between 0.6 and 70 mA. A very similar qualitative behaviour as in Fig. 4.2a is found with larger absolute values at higher current.

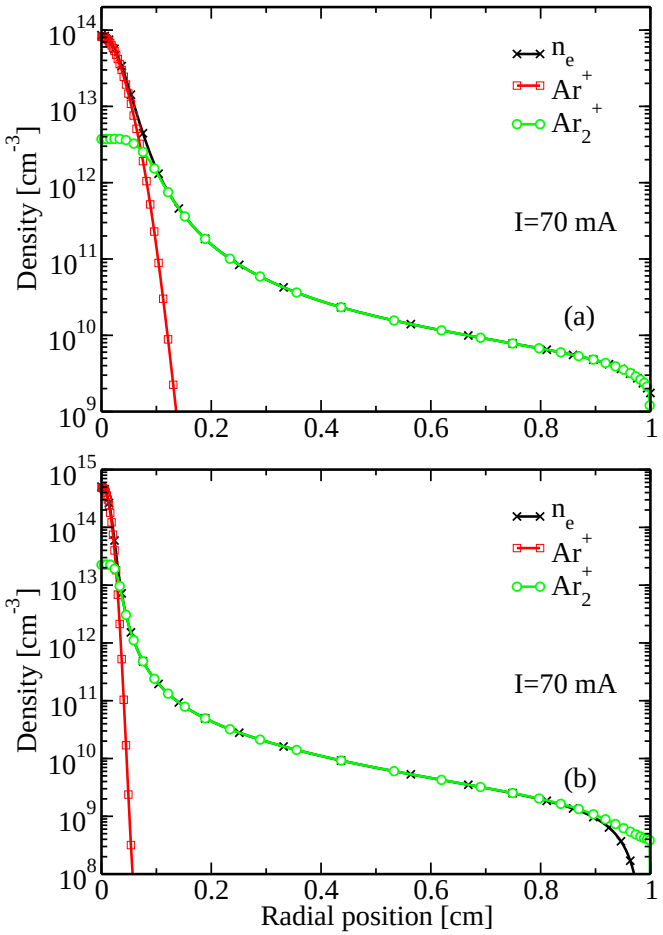

Figure 4.3: Radial profiles of charged species in the constricted mode of the positive column for argon at $p = 100$ Torr (a), at $p = 500$ Torr (b), and discharge current $I = 70$ mA.

Fig. 4.3 shows the radial population of charged species in the constricted discharge at $I = 70$ mA. The population of atomic ions is almost equal to the electron density in the constricted discharge core and abruptly decreases in the outer part of the discharge region, where molecular ions are predominant. A simplified reaction kinetic scheme can be proposed to explain the different distributions of atomic and molecular ions. Atomic ions are created by direct and stepwise ionization processes and are rapidly converted into molecular ions through three-body reactions with two ground state atoms. The main loss channel for molecular ions is dissociative recombination by electron impact. Due to strong

heating near the axis of the discharge tube the ground state argon atom density is depleted there. Therefore, the gain of molecular ions from ion conversion, which is proportional to the square of ground state density, is much smaller in the center of the positive column. At the same time, the loss of molecular ions due to dissociative recombination, which is proportional to electron density, is higher near the axis compared to the outer part of the discharge. Consequently, the density of atomic ions considerably exceeds that of the molecular ions in the center of the constricted discharge for the considered plasma parameter range.

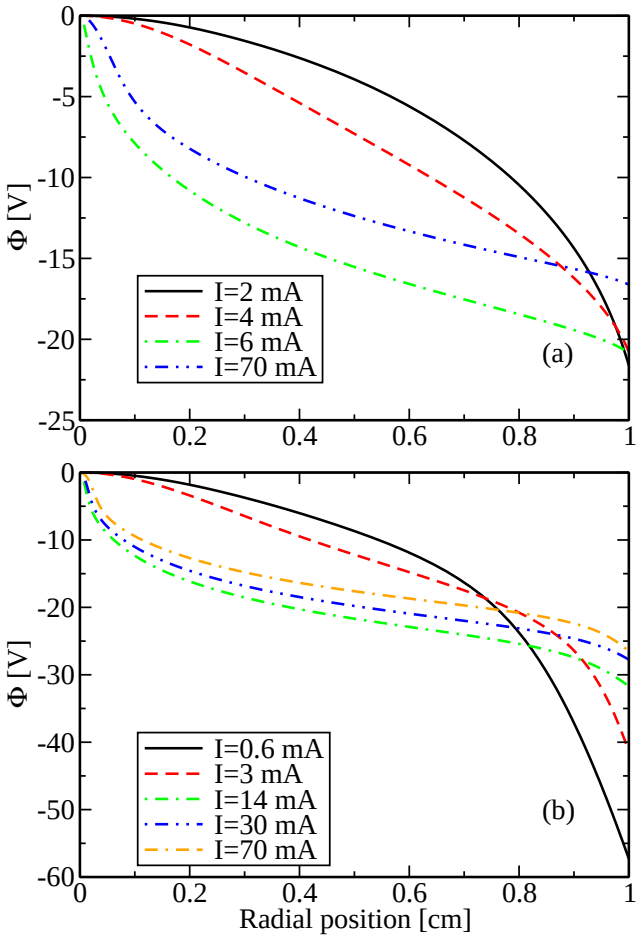

Figure 4.4: Radial profiles of the electric potential for argon at $p = 100$ Torr (a), at $p = 500$ Torr (b), and different discharge currents.

Fig. 4.4a illustrates the radial distribution of the electric potential for different

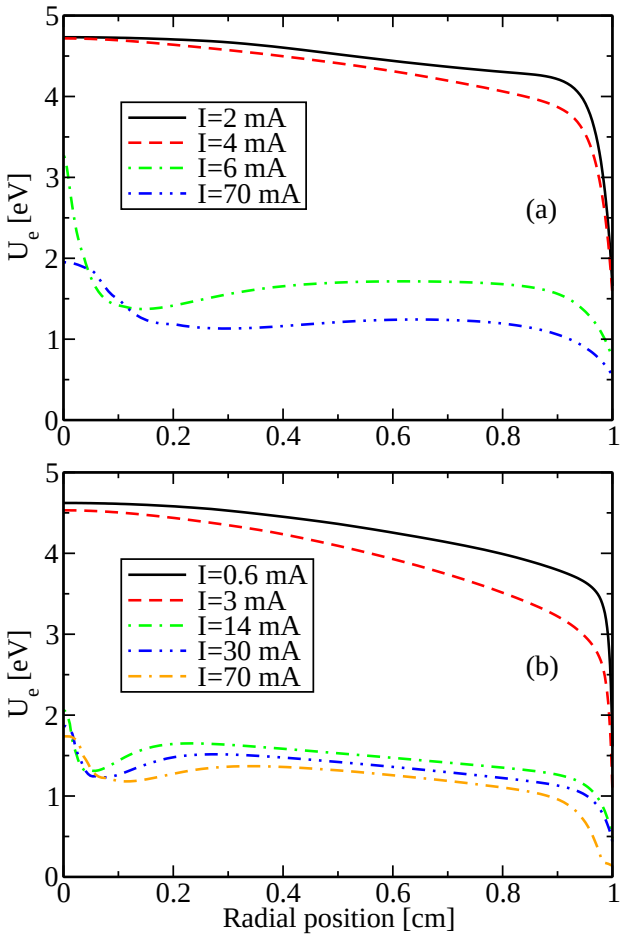

Figure 4.5: Radial profiles of the mean electron energy for argon at $p = 100$ Torr (a), at $p = 500$ Torr (b), and different discharge currents.

discharge current for pressure 100 Torr. For currents up to 4 mA the radial profile of the electric potential is close to classical potential profiles of the diffuse positive column: slow variation near the axis and fast variation of the radial electric potential near the wall. During transition from the diffuse to the constricted mode of the positive column radial profile of the electric potential changes completely. Strong constriction of the charge carriers near the axis leads to fast variation of the electric potential. The outer region of the positive column is characterized by slow increase of the electric potential.

Fig. 4.4b shows the radial distribution of the electric potential for different

discharge current for pressure 500 Torr. A very similar behaviour in the radial variation of the electric potential is observed for the two pressures of 100 and 500 Torr. An increase of pressure leads to higher wall potential. Such behaviour is caused by volume recombination, which is more pronounced at higher pressure.

Fig. 4.5a shows the radial distribution of the mean electron energy for different discharge current for pressure 100 Torr. The diffuse mode of the positive column is characterized by high mean electron energy, which slightly decreases with current. Transition from the diffuse state to the constricted state leads to abrupt decrease of the average value of the mean electron energy by factor of 2, which also decreases with current. Difference of the mean electron energy values for two modes is explained by the different values of electric field strength E_z in the diffuse and constricted positive column (see Fig. 4.8a). Radial profile of the mean electron energy is almost homogeneous (except for the wall region) for the diffuse state of the discharge. However, the constricted mode of the positive column is characterized by the inhomogeneity of the mean electron energy near the axis. Such behaviour can be explained by nonlocal nature of the mean electron energy during transition from the diffuse to the constricted mode. More details will be given in Section 4.6.

Fig. 4.5b shows the radial distribution of the mean electron energy for different discharge current for pressure 500 Torr. A very similar qualitative behaviour as in Fig. 4.5a is found. The mean electron energy at the tube axis for the diffuse mode is almost independent of the gas pressure. The reason is the following: the EVDF in the argon plasma is not a Maxwellian one in the whole range of electron energies, especially in the case of the low ionization degree. Therefore, the U_e value characterizes the main body of the EVDF but not its high energy tail, which governs the excitation rates of electronic levels from the ground state by the electron impact.

4.2 Comparison with experimental and other modelling results

Model calculations have been performed for two assumptions of the EVDF, i.e., (i) using the standard fluid model and (ii) employing the Maxwellian energy distribution (2.23) to determine the rate and transport coefficients (B.7), (2.18), (B.1), (B.2), (B.3) and (B.4) of the electrons. This second approach is referred to as "Maxwell model" in the following.

The results obtained by means of both the models have been compared with existing experimental data from Ref. [3] and model calculation results in [40].

The diagnostics in [3] consisted of measurements of the axial electric field and of the radial brightness profile of the bremsstrahlung continuum. The absolute values and radial profiles of the electron density and heavy particle temperature were determined from the current balance and heat balance equation. The latter equation was written assuming that all discharge power gained from axial electric field is transferred into heavy particle heating. The "electron temperature" was calculated from the measured axial electric field and the electron energy balance taking into account the redistribution of ground state argon atoms in the radial direction. Because power is also spent in many inelastic processes, such as ionization and excitation, the above assumption can be a rough overestimation and, unfortunately, the errors accompanied with such determination were not estimated in [3].

Fig. 4.6 and Fig. 4.7 show the axial electric field E_z as well as the electron density $n_e(0)$, electron temperature $T_e(0)$ and heavy particle temperature $T_h(0)$ on the discharge axis versus the discharge current for a pressure of 100 Torr and the current range between 2 and 70 mA. For the standard model the "electron temperature" is calculated according following relation: $T_e = 2U_e/3$.

The results of the standard model agree sufficiently well with the experimental data of [3] and model predictions of Petrov *et al.* [40]. They show a jump for a critical value of the discharge current I_{crit}. In particular, $n_e(0)$ abruptly increases by more than one order of magnitude [Fig. 4.6b], while E_z [Fig. 4.6a] and $T_e(0)$ [Fig. 4.7a] steeply drop at the same critical current value. Remaining

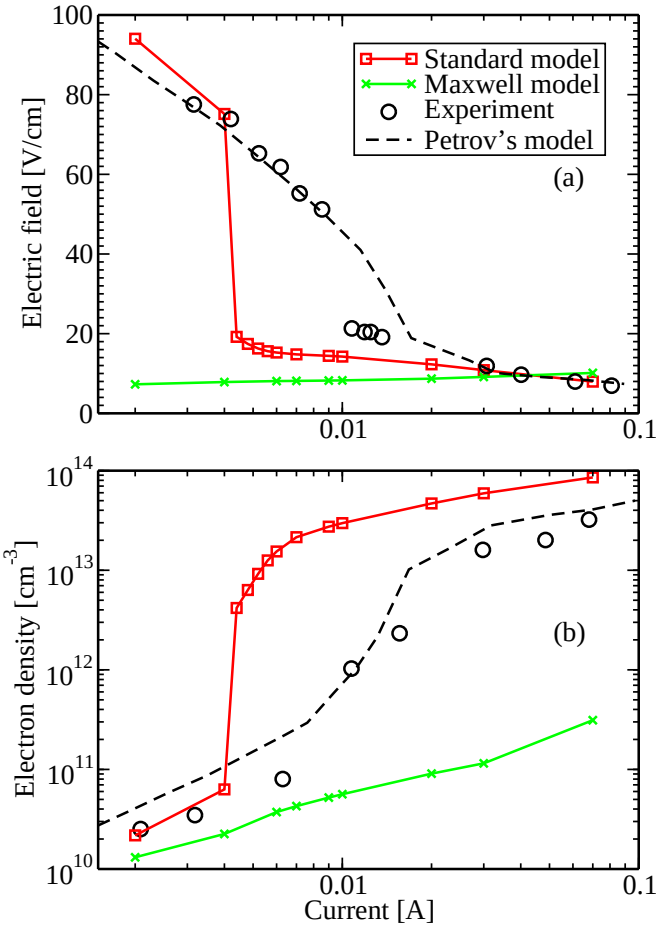

Figure 4.6: Axial electric field (a) and electron density on the axis (b) as a function of the discharge current at $p = 100$ Torr.

discrepancies between the standard and Petrov's model occur around the critical current and can be attributed e.g. to different atomic data and assumptions in the models. In particular, the present standard model predicts the jump into the constricted mode at a smaller current value than the experiments, while Petrov's model [40] results in a transfer to the constricted mode at a little larger current value in comparison with the measurements. The model results of the heavy particle temperature exhibit a small drop during the transition from the diffuse to the constricted state, which has also been observed in the experiments. Such

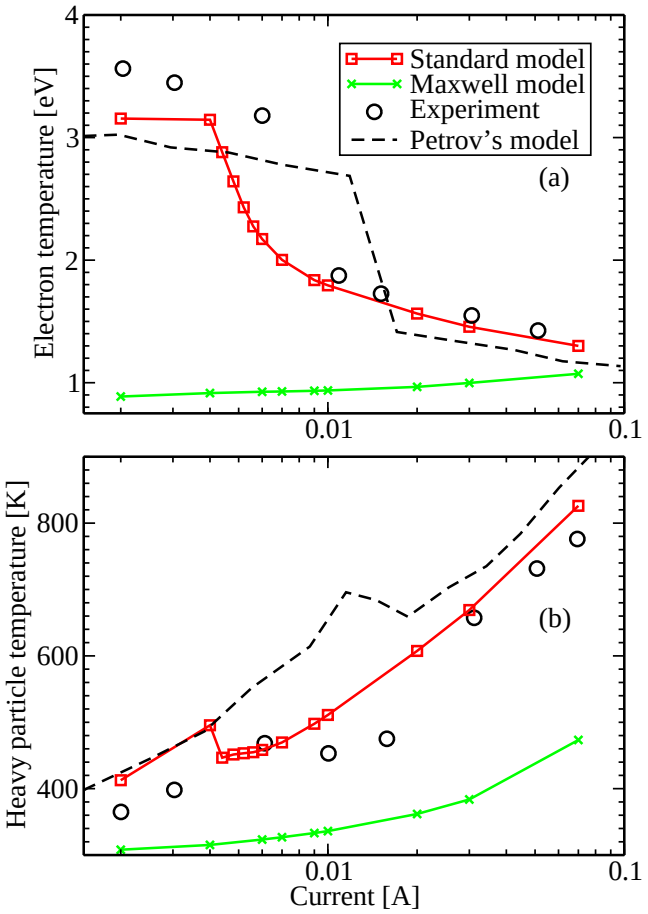

Figure 4.7: Electron temperature on the axis (a) and heavy particle temperature on the axis (b) as a function of the discharge current at $p = 100$ Torr.

behaviour is caused by the decrease of the total power IE_z dissipated through the volume. The results show as well that the assumption of a Maxwellian energy distribution is not appropriate for describing the constriction of glow discharges in argon for the considered plasma parameters. This finding confirms the explanation proposed in [3] that the main reason of positive column constriction is the nonlinear dependence of the electron production frequency on the electron density. Contrary to the Maxwellian energy distribution, which is determined on the assumption of constant electron-atom collision frequency, such dependence can be reproduced from rate coefficients which result from solutions of the electron

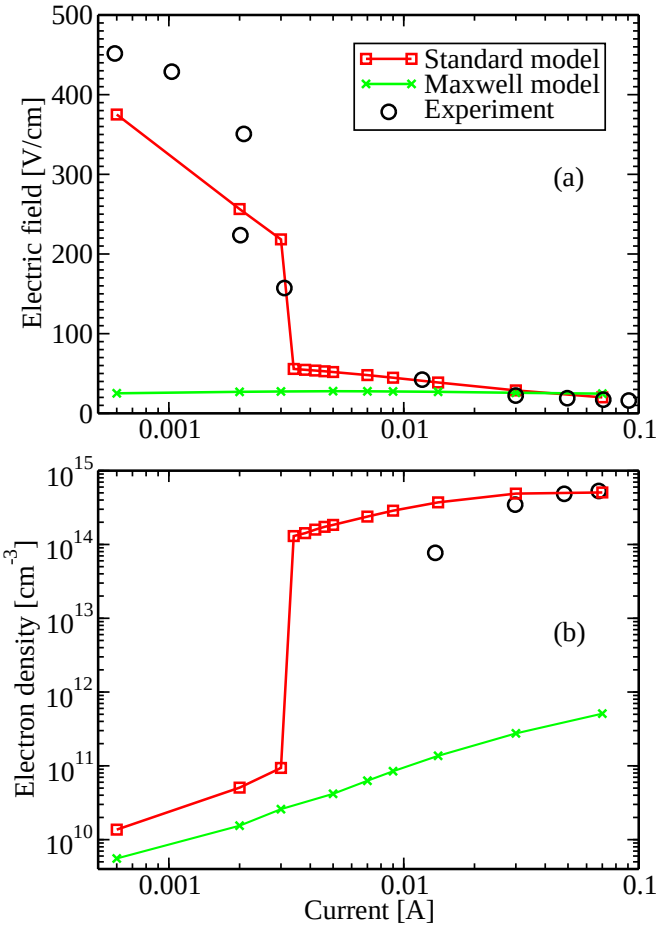

Figure 4.8: Quantities as in Fig. 4.6 but for a pressure of 500 Torr.

Boltzmann equation for the EVDF.

The corresponding dependence of the axial field as well as of the electron density, electron temperature and heavy particle temperature at the discharge axis on the discharge current is shown in Fig. 4.8 and Fig. 4.9 for a pressure of 500 Torr.

A very similar qualitative behaviour as in Fig. 4.6 and Fig. 4.7 is found. The results obtained by the standard fluid model show good agreement with experimental data of [3], especially for the range of higher current. They demonstrate that a growth of the argon pressure leads to a small decrease of the critical value

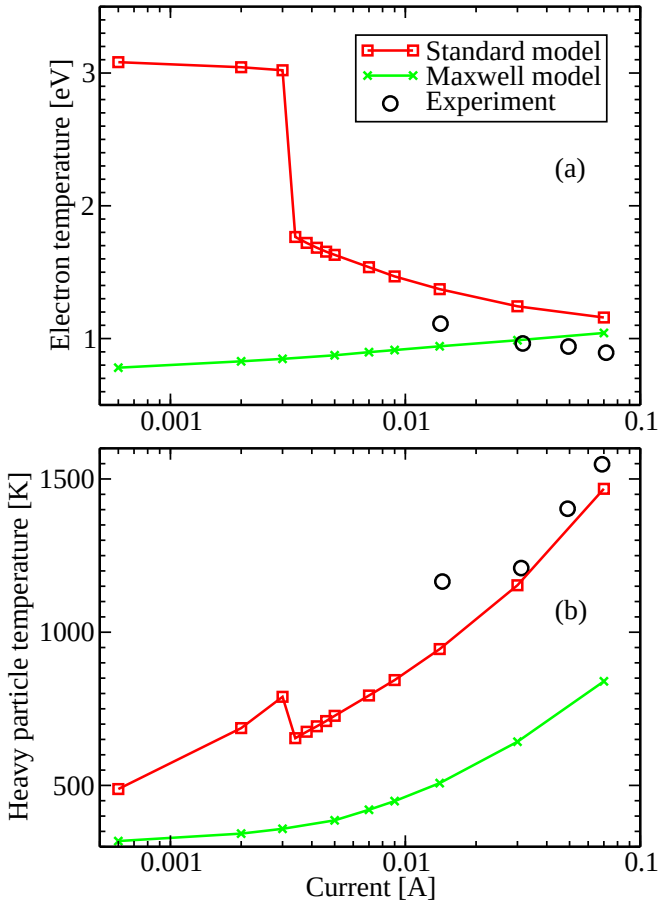

Figure 4.9: Quantities as in Fig. 4.7 but for a pressure of 500 Torr.

of the discharge current required for constriction and to an increase of the absolute values of E_z, $n_e(0)$ and $T_h(0)$. In particular, differences of three orders of magnitude between the electron density values on the discharge axis near the critical current for the diffuse and constricted case are found. However, even for the case of higher pressure the assumption of a Maxwellian energy distribution is not suitable to reproduce the glow-to-arc transition of the argon positive column.

4.3 Impact of the Druyvesteyn distribution

Model calculations have been performed for two assumptions of the EVDF, i.e., (i) using the standard fluid model and (ii) employing the Druyvesteyn energy distribution (2.24) to determine the rate and transport coefficients (B.7), (2.18), (B.1), (B.2), (B.3) and (B.4) of the electrons. This second approach is referred to as "Druyvesteyn model" in the following. The results obtained by means of both the models have been compared with existing experimental data from Ref. [3].

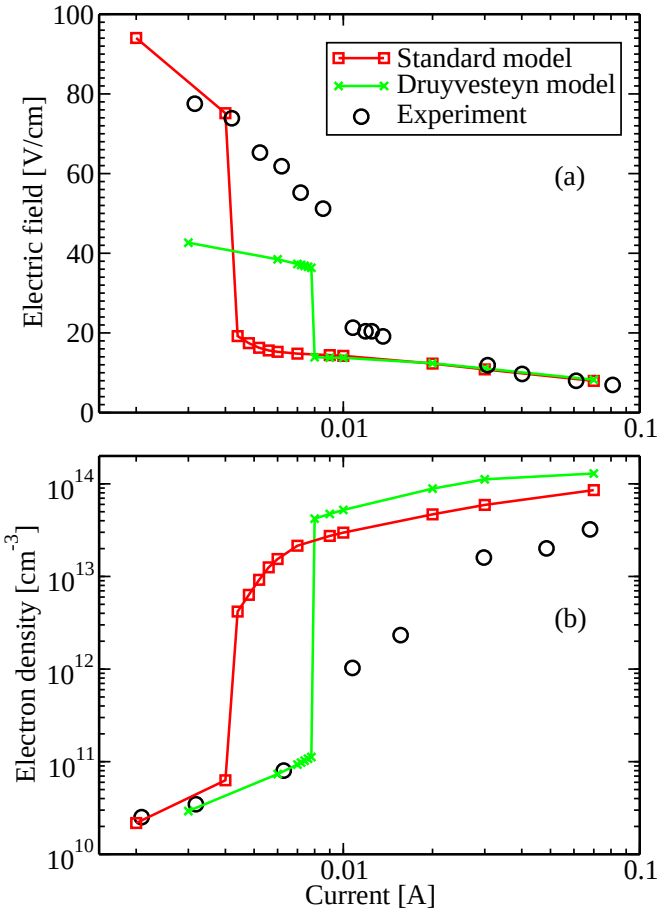

Figure 4.10: Axial electric field (a) and electron density on the axis (b) as a function of the discharge current at $p = 100$ Torr.

Fig. 4.10 illustrates the axial electric field E_z as well as the electron density $n_e(0)$ on the discharge axis versus the discharge current for a pressure of 100 Torr and the current range between 2 and 70 mA. The results of the Druyvesteyn model agree qualitatively with the experimental data of [3] and standard model predictions. They show a jump for a critical value of the discharge current I_{crit}, which is higher than that for the standard model. In particular, good agreement has been obtained for the constricted mode of the discharge. However, results of the Druyvesteyn model have bad agreement for the diffuse mode of the discharge. In particular, the axial electric field is approximately two times smaller in comparison with results of the standard model and of the experiment.

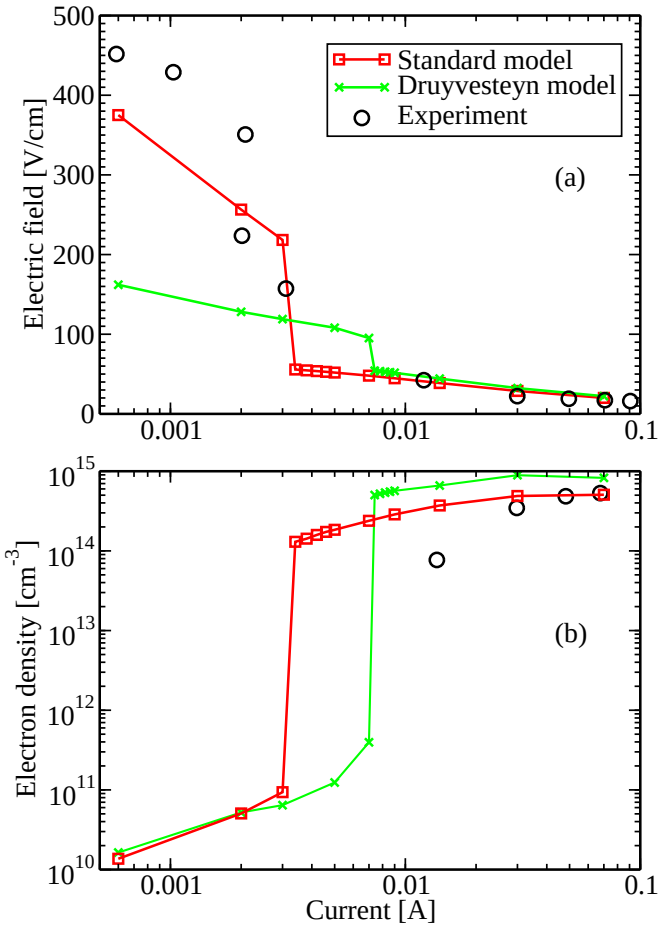

Figure 4.11: Quantities as in Fig. 4.10 but for a pressure of 500 Torr.

The corresponding dependence of the axial field as well as of the electron density at the discharge axis on the discharge current is shown in Fig. 4.11 for a pressure of 500 Torr and the current range between 0.6 and 70 mA.

A very similar qualitative behaviour as in Fig. 4.10 and Fig. 4.11 is found. A growth of the argon pressure leads to a small decrease of the critical value of the discharge current required for constriction and to an increase of the absolute values of E_z and $n_e(0)$, similarly to the standard model results. As in case of the lower pressure the axial electric field has approximately two times lower value for the diffuse mode of the discharge. However, the assumption of a Druyvesteyn energy distribution is found to be suitable to reproduce qualitatively the glow-to-arc transition of the argon positive column.

The model calculations have been carried out using the EVDF obtained from the solution of 0D BE without consideration of electron-electron collisions for the diffuse mode of the discharge. The obtained results are the same as in case as in case of including of electron-electron collisions. However, the application of such assumption of the EVDF for the constricted mode of the discharge does not lead to convergent solution. The reason of such behaviour requires additional studies.

4.4 Impact of different boundary conditions

The boundary conditions for the fluid equations are an essential part of the description of the model. For the particle balance equations as well as mean electron balance equation, a variety of the boundary conditions can be found in the literature. In the present section two approaches have been compared: (i) simple boundary conditions, such as $\nabla n \cdot \mathbf{n} = 0$ with $\mathbf{n}$ a normal vector; (ii) more general boundary conditions, according to [62]. Details related to the last approach have been mentioned in Section 2.4.

Fig. 4.12 illustrates the radial distribution of the electron density for the pressure 500 Torr and electric current 3 mA. “Case 1” is the modelling result for the fluid model with simple boundary conditions $\nabla n \cdot \mathbf{n} = 0$. Such boundary conditions have been applied to density balance equations and the mean electron energy balance equation. “Case 2” and “Case 3” are results for the fluid model

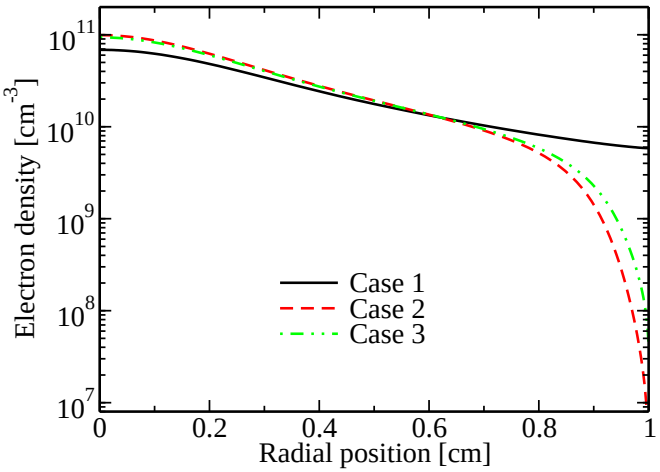

Figure 4.12: Radial profiles of the electron density for argon at $p = 500$ Torr and dc current of 3 mA.

with general boundary conditions [62]. For the two last cases the following electron reflection coefficients have been adjusted: $b_e = 0.7$ (case 2) and $b_e = 0.9$ (case 3), respectively.

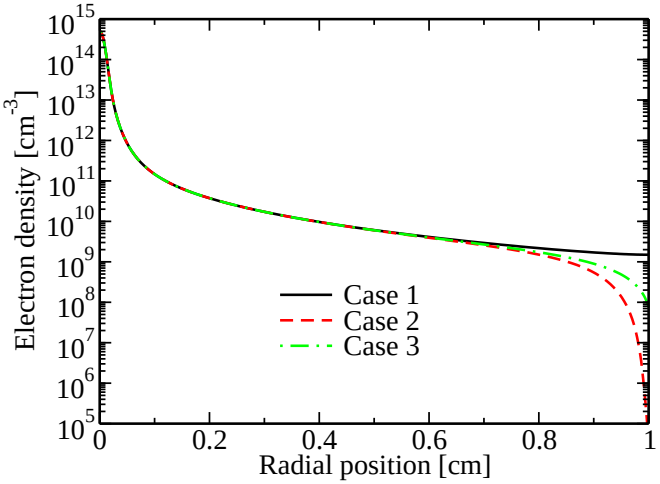

Figure 4.13: Radial profiles of the electron density for argon at $p = 500$ Torr and current 30 mA.

The radial distribution of the electron density has a typical diffuse profile. The application of the different boundary conditions leads to different radial profiles

of the electron density for the diffuse mode of the positive column. In particular, the model result of the radial distribution of the electron density with simple boundary conditions ("Case 1") has a more flat profile in comparison with model results with general boundary conditions ("Case 2" and "Case 3"). Adjusting Hagelaar's boundary conditions at the wall leads to larger population of the electron density at the axis of the positive column and to rapid decrease near the wall. The variation of the electron reflection coefficient b_e causes different electron density distributions near the wall: the decrease of b_e leads to the decrease of the value of the electron density near the wall. However, this does not influence the remaining part of the positive column.

Fig. 4.13 shows radial distributions of the electron density for the pressure 500 Torr and electric current 30 mA. The radial distribution of the electron density has a typical constricted profile. For all cases of boundary conditions the qualitative distribution of the electron density near the wall is similar to the diffuse mode: flat profile for "Case 1" and fast decreasing profile for "Case 2" and "Case 3". However, adjusting different boundary conditions does not influence the central part of the positive column.

Adjusting different boundary conditions leads to the same behaviour of other physical quantities as in case of the electron density.

4.5 Results of the model predictions for higher currents

The fluid model has been applied to predict argon positive column properties for higher currents. Like in Section 4.2 model calculations have been performed for two assumptions of the EVDF, i.e., (i) using the standard fluid model and (ii) employing the Maxwellian energy distribution.

Fig. 4.14 and Fig. 4.15 show the axial electric field E_z as well as the electron density $n_e(0)$, electron temperature $T_e(0)$ and heavy particle temperature $T_h(0)$ on the discharge axis versus the discharge current for a pressure of 500 Torr and the current range between 0.25 and 7.5 A.

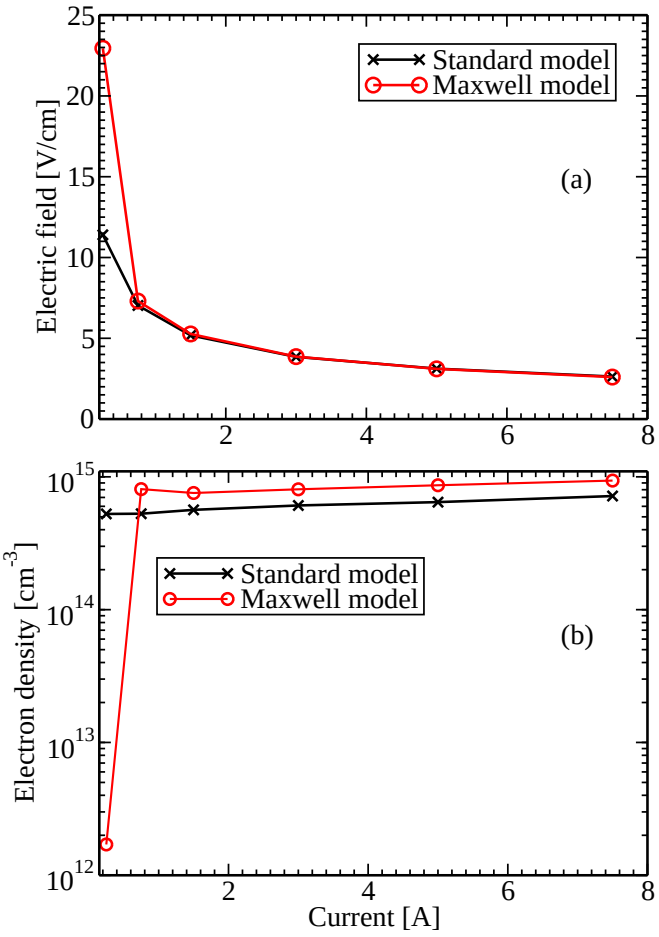

Figure 4.14: Axial electric field (a) and electron density on the axis (b) as a function of the discharge current at $p = 500$ Torr.

For the considered discharge parameters the positive column exists only in constricted mode. Further increase of the discharge current leads to smooth decrease of the E_z [Fig. 4.14a] and $T_e(0)$ [Fig. 4.15a]. $n_e(0)$ [Fig. 4.14b] and $T_h(0)$ [Fig. 4.15b] increase with the discharge current. The results reveal a transformation of the constricted positive column into the arc. In particular, the heavy particle temperature is only a factor of two lower than the electron temperature at highest current value. The model predictions show that the assumption of a Maxwellian energy distribution gives almost the same results as standard model

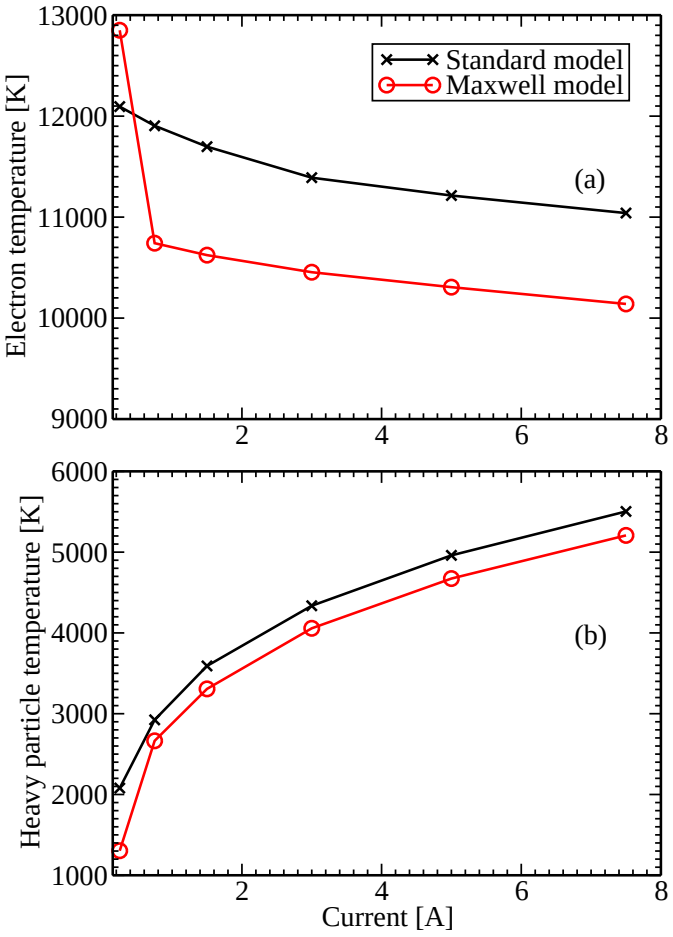

Figure 4.15: Electron temperature on the axis (a) and heavy particle temperature on the axis (b) as a function of the discharge current at $p = 500$ Torr.

for discharge currents $I \geq 1$ A and can be used for simplification in this parameter range.

4.6 Role of ion kinetics and gas temperature in the discharge constriction

The predominance of the volume recombination of the charged particles over surface recombination is a necessary condition for the constriction of a discharge

column. In rare-gas plasmas the dissociative recombination of electrons and molecular ions plays the leading role for a medium current range.

$$e + Rg_2^+ \Rightarrow Rg^* + Rg \tag{4.1}$$

Hear, Rg_2^+ is the molecular ion, Rg^* is the excited atom and Rg is the ground state atom.

In a rare-gas discharge, molecular ions prevail over atomic ones at relatively high pressure and moderate heavy particle temperatures. The relative population N_{ai} of atomic and N_{mi} molecular ions in rare-gas plasmas can be estimated on the basis of the equilibrium relation [110]

$$\frac{N_{ai}N_0}{N_{mi}} = \frac{g_{ai}g_0}{g_{mi}} \exp\left(-\frac{D}{k_B T_h}\right) \frac{1}{2\pi r_0^2} \sqrt{\frac{\mu k_B T_h}{2\pi\hbar}} \left[1 - \exp\left(-\frac{\hbar\omega}{k_B T_h}\right)\right] \quad , \tag{4.2}$$

where g_{ai}, g_0, g_{mi} are the statistical weights of the corresponding neutral and ionized particles; r_0 is the equilibrium internuclear distance; μ is the reduced mass; D is the dissociation energy and $\hbar\omega$ is the vibrational energy quantum for the molecular ion. The rare-gas molecular ions have a dissociation energy in the range 1 - 2 eV, thus, as it follows from relation 4.2, the molecular ions prevail over the atomic ones only at moderate heavy particle temperatures $T_h \leq 1000$ K.

Figs. 4.16 shows the heavy particle temperature on the axis as well as the dimensionless constriction radius r_c/R versus the discharge current at $p = 500$ Torr and $R = 1$ cm. The effective radius of the constricted positive column is estimated at a level of e^{-1} of the normalized electron density profile. While the heavy particle temperature is smaller than some equilibrium value, molecular ions dominate, and therefore, promote the discharge constriction. Further increase of the discharge current causes a rise of the heavy particle temperature (see Fig.4.16a). This leads to the destruction of the molecular ions and, as a consequence, to a decay in the contribution of the volume neutralization to the charged particle balance. Further increase of the atomic ion populations is accompanied by lowering of the constriction effect of the gas discharge constriction and, consequently, by a rise in the cross section of the area filled with the discharge current.

The constricted discharge radius can be roughly estimated from the solution of the heavy particle temperature balance equation, namely, considering this value

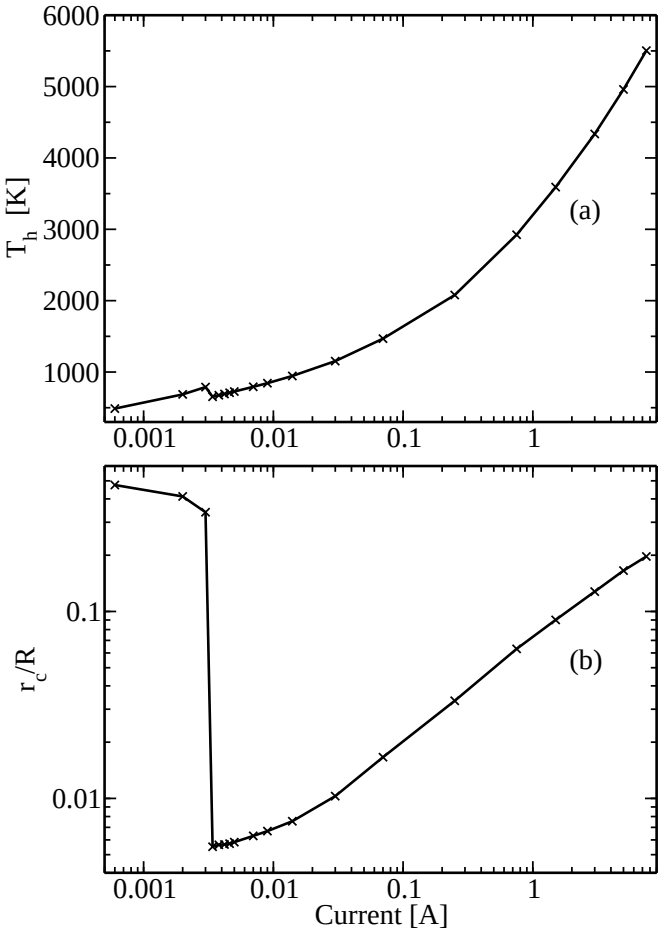

Figure 4.16: The heavy particle temperature on the axis (a) and the dimensionless constriction radius r_c/R (b) versus the discharge current at $p = 500$ Torr and $R = 1$ cm.

as a dimension of the region where the heavy particle temperature is so high that the relative density of the molecular ions is negligible. Increasing the discharge current leads to an increase of the region filled with the discharge. The latter is shown in Fig. 4.16b where the dependence of the effective radius of the constricted discharge in argon versus current at pressure $p = 500$ Torr is given. Similar results have been obtained for the constricted discharge in Ar at pressures 20 and 50 Torr [26].

4.7 Mean electron energy balance

The main features of the nonequilibrium behaviour of the positive column plasma can be observed from the electron power budget. In Fig. 4.17 the most important contributions to the local electron power balance, i.e., the transport term $\partial(r\Gamma_\varepsilon)/(r\partial r)$, Joule heating, the gain rate S_{sc} due to superelastic collisions (de-excitation), and the loss rates due to elastic collisions, excitation, ionization and dissociative recombination of electrons are shown as functions of the radial position for the pressure $p = 100$ Torr and the discharge currents 2, 9, and 70 mA. Further contributions, which are taken into account in the model, like "radial cooling", gain from three-body recombination and chemo-ionization processes, have negligible influence and, therefore, they were not plotted. Because the effective radius of the constricted plasma column is small compared with the discharge tube radius R, a logarithmic scale of the radial position was used.

In the diffuse mode with $I < I_{crit}$ [Fig. 4.17a] the dominant power gain process is the gain from the axial electric field, while the contribution of the transport term and de-exciting electron collisions is insignificant. Elastic collisions represent the main power loss mechanism for the electrons, while inelastic losses due to excitation have a quite smaller contribution. The ionization and dissociative recombination losses are almost negligible for the diffuse discharge.

The picture changes completely, when the glow discharge is in the constricted mode [Figs. 4.17b and 4.17c]. Then, the electron power is concentrated near the axis of the glow discharge. The absolute values of the main power contributions at the discharge axis have increased by about three orders of magnitude compared with the diffuse discharge in Fig. 4.17a, when the current is increased above about 5 mA. In the constricted mode the electron power is dissipated mainly in excitation and to a lesser extent in elastic collisions. The losses due to ionizing collision processes and dissociative recombination are of minor importance.

In constricted discharges at lower currents [Figs. 4.17b] the magnitude of the power gain by Joule heating and de-exciting electron collisions is smaller than that of elastic and inelastic losses in the discharge core and it exceeds slightly the losses in the outer column part. The large difference between these terms in the mean electron energy balance in the core region is compensated by the transport

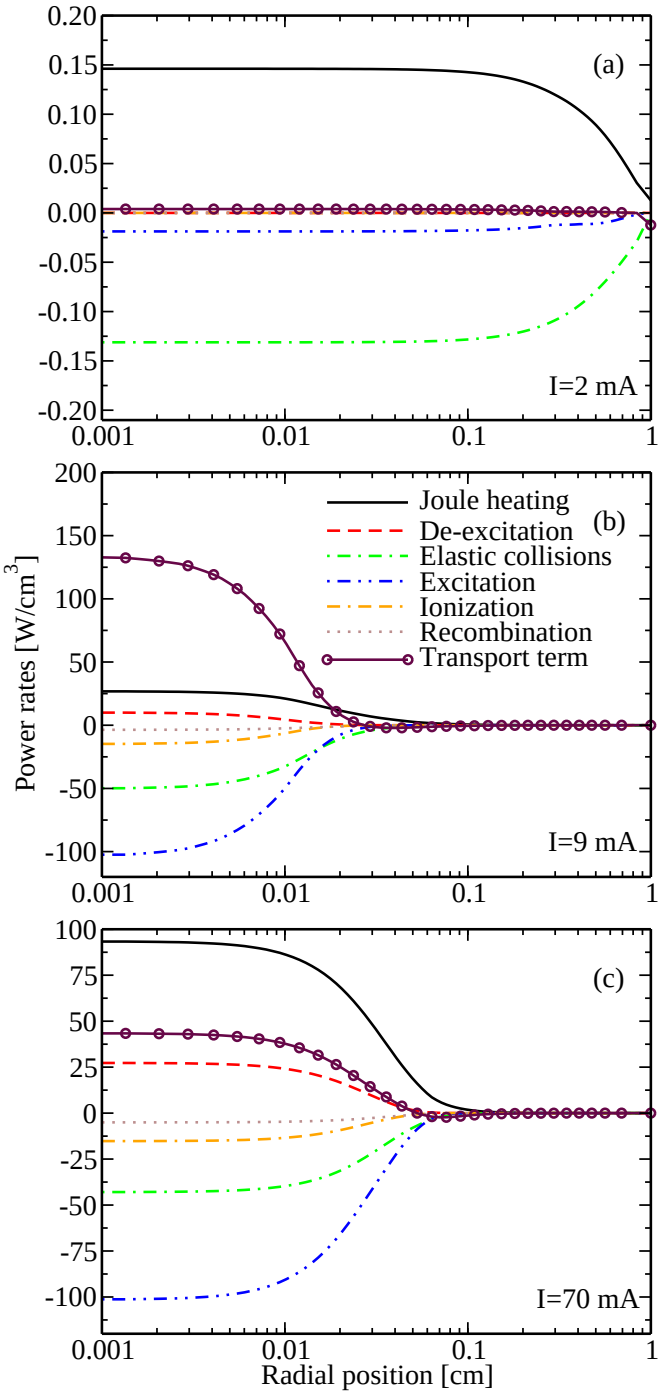

Figure 4.17: Contributions to the electron power balance as a function of the radial position at $p = 100$ Torr for $I = 2$ (a), 9 (b), and 70 mA (c).

term. In such cases the local power loss in collisions is only partly compensated by the local power gain, and a significant electron energy flux is produced, which totally compensates the remaining difference in the power budget. This is a key feature of the nonlocal behaviour of the electron component. The establishment of a considerable radial electron energy flux in the positive column has already been discussed in [52; 111] for low pressure plasma conditions. This energy flux is inward directed in the constricted plasma core and transfers energy from outer to inner parts of the column. Consequently, the process of the constriction consumes power from outer parts of the discharge. When the current is increased further on, the transport term becomes smaller than the Joule heating and the de-exciting electron collisions contribute by about 15% to the total power gain as it is illustrated in Fig. 4.17c. At the same time only small changes in the loss terms are found.

Fig. 4.18 illustrates the corresponding contributions to the electron power balance for the same discharge currents and a pressure of 500 Torr. A very similar behaviour in the radial variations of the different contributions is observed for the two pressures of 100 and 500 Torr with larger absolute values at higher pressure. Again, the local power gain from electric field is compensated by local power losses due to elastic and inelastic collisions for the diffuse mode at $I = 2$ mA [Fig. 4.18a]. In the constricted mode shown in Figs. 4.18b and 4.18c the higher pressure is accompanied by a larger power dissipation in electron collisions and a reduced contribution of the transport term. At the same time de-exciting electron collisions gain increasing importance at the higher pressure. The current growth in the constricted mode causes a transition from a nonlocal behaviour of the electrons to an almost local one [Fig. 4.18c], where the transport term is insignificant.

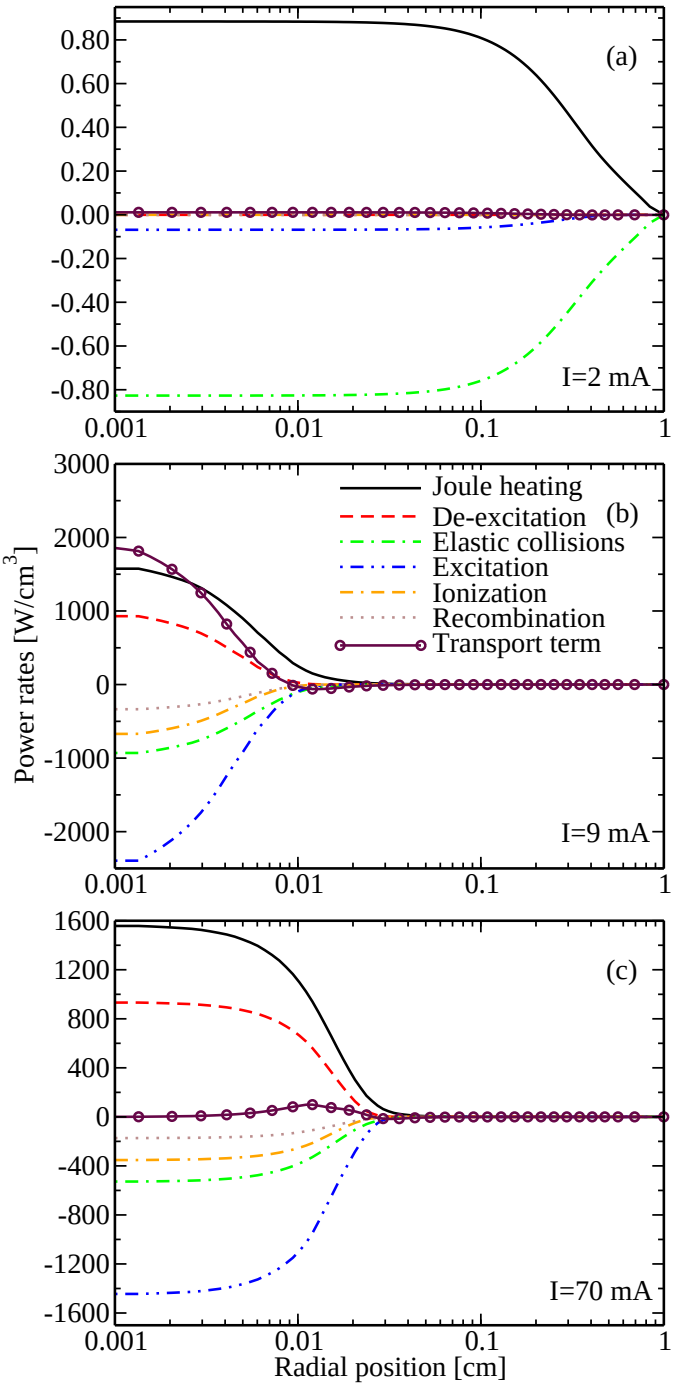

Figure 4.18: Quantities as in Fig. 4.17 but for a pressure of 500 Torr.

5

Results of the xenon glow discharge at medium pressure

5.1 Introduction

Nowadays artificial light sources have many applications in the human life. One of the artificial light sources is the gas-discharge lamp that generates light by passing an electrical discharge through an ionized gas. Typically, such lamps utilize a rare gas (neon, argon, krypton, xenon) or a mixture of these gases as a buffer gas. Most lamps are filled with additional materials, like mercury, sodium, and/or metal halides. For example, mercury vapor discharge emits photons, resulting in ultraviolet radiation. Ultraviolet (UV) radiation is converted to visible light by a fluorescent coating on the inside of the lamp's glass surface. UV radiation can be used directly to perform curing processes [112], UV-lamp induced metal deposition [113], UV assisted oxidation of Si and Ge, photo-etching and microstructuring of polymer surfaces [114; 115].

Fluorescent lamps with mercury admixture have many advantages: (i) high luminous efficacy in comparison with conventional tungsten filament incandescent lamp; (ii) typical lifetime of the fluorescent lamp is 10-20 larger than that of the incandescent lamp; (iii) fluorescent lamps offer more diffuse and physically larger light sources than point sources of light from an undiffused incandescent filaments. However, such lamps have many disadvantages. If a fluorescent lamp is broken, a very small amount of mercury can contaminate the surrounding environment.

Mercury fluorescent lamps efficacy decreases if ambient temperature is lower than room temperature.

Rare gases are an attractive substitute for mercury since they also emit strong resonance radiation. Also, their density is independent of the ambient temperature. Among other rare gases xenon has the ionization energy closest to the mercury hence the lamp power requirement is expected to be similar. Nevertheless, the light sources based on xenon have lower vacuum ultraviolet (VUV) efficiency. The luminance can be increased by increasing the lamp current or/and pressure. However, it usually leads to the positive column constriction, where the usual diffuse discharge discontinues and a bright narrow filament is formed. Also, the intensity of the phosphor-converted emissions from a contracted discharge is very low.

To suppress such behaviour and to enhance the efficiency gas discharge can be operated in pulsed mode. In a pulsed discharge, processes in a xenon plasma such as ionization, excitation, emission and so on are greatly different from those in steady state discharges such as dc. In the afterglow phase of a pulsed discharge especially two effects play an important role in the generation of radiation. Due to the high formation rate, atomic ions are converted to molecular ones by three-body collisions with two ground state atoms. Dissociative recombination between molecular ions and electrons is the main channel of the destruction of the plasma and leads to population of the excited state levels lying below the Xe_2^+. These levels are sources of atom line radiation. Also, excited atoms in the states $1s_5$ (metastable) and $1s_4$ (resonance) are the precursors for the formation of excimers Xe_2^* in three-body collisions with ground state atoms. These excimers radiatively decay into the dissociative van der-Waals ground state $^1\Sigma_g^+$ and emit the radiation of the so-called first and second continuum at 151 nm and 172 nm, respectively.

In the present thesis a medium pressure xenon discharge in pulsed mode has been studied by means of the time- and radial-dependent fluid modeling. The model predictions are compared with time-resolved measurements of the axial electric field strength, and of the absolute densities of the metastable ($1s_5$) and resonance ($1s_4$) levels [116; 117]. The discharge behaviour of medium pressure xenon plasmas in dc and pulsed modes is analyzed.

5.2 DC mode

Model calculations for xenon plasmas have been performed in accordance with the experimental conditions of [116]. The discharge tube has an inner diameter of 6.5 mm and a column length of 70 cm. The set of time-dependent fluid equations 2.1, 2.3, 2.5, 2.9, 2.10, 2.19, and the Poisson equation 2.21 as well as a current balance determining the axial electric field 2.22 have been solved numerically until steady state is reached, according to the scheme presenting in Fig. 3.2. Here, results for pressures of 20, 40 and 50 Torr and discharge currents between 60 and 150 mA are reported.

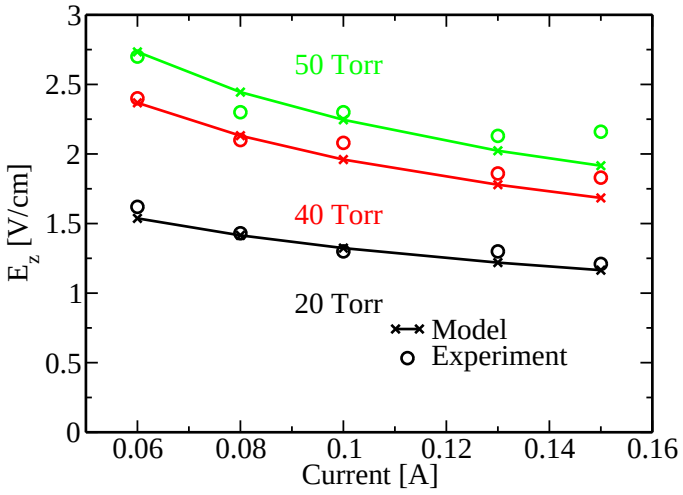

Figure 5.1: Axial electric field as a function of the discharge current at different pressures (symbols - experiment, lines - model results).

Fig. 5.1 shows the dependence of the axial electric field E_z on the current at three different pressures. The model results agree well with experimental data [117]. The negative dependence of the electric field on the discharge current is reproduced as well.

Fig. 5.2 illustrates the dependence of the electron density on the axis $n_e(0)$ [Fig. 5.2a] as well as the metastable density on axis $Xe_{1s_5}(0)$ [Fig. 5.2b] on the current at three different pressures. The population of the electron density increases with growing of the discharge current as well as of the gas pressure. Such behaviour is due to increased electron-atom collision frequency. The population of

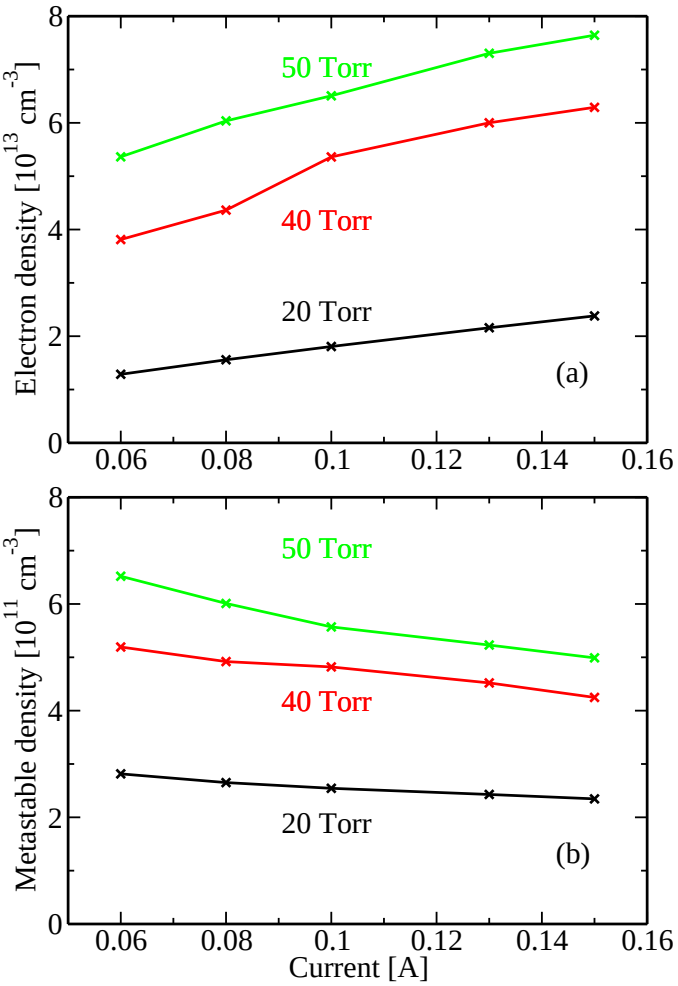

Figure 5.2: Electron (a) and metastable [Xe($1s_5$)] (b) density on the axis as a function of the discharge current at different pressures.

the metastable density has the negative dependence on the discharge current. The main source of the electron density is stepwise ionization from the excited levels. Therefore, the increase of the electron density with growing of the discharge current leads to the decay of the metastable density. The main source of the metastable density is direct ionization from the ground level. Thus, the growth of the ground state density with increasing of the gas pressure leads to increasing of the metastable density.

The xenon plasma is constricted at the pressure and current range considered.

The radial distribution of the electron density at 50 Torr and 130 mA is shown in Fig. 5.3a. The electron density falls from the axis toward the wall by a factor of approximately 10 over a distance of $r/R \approx 0.5$, which indicates constriction.

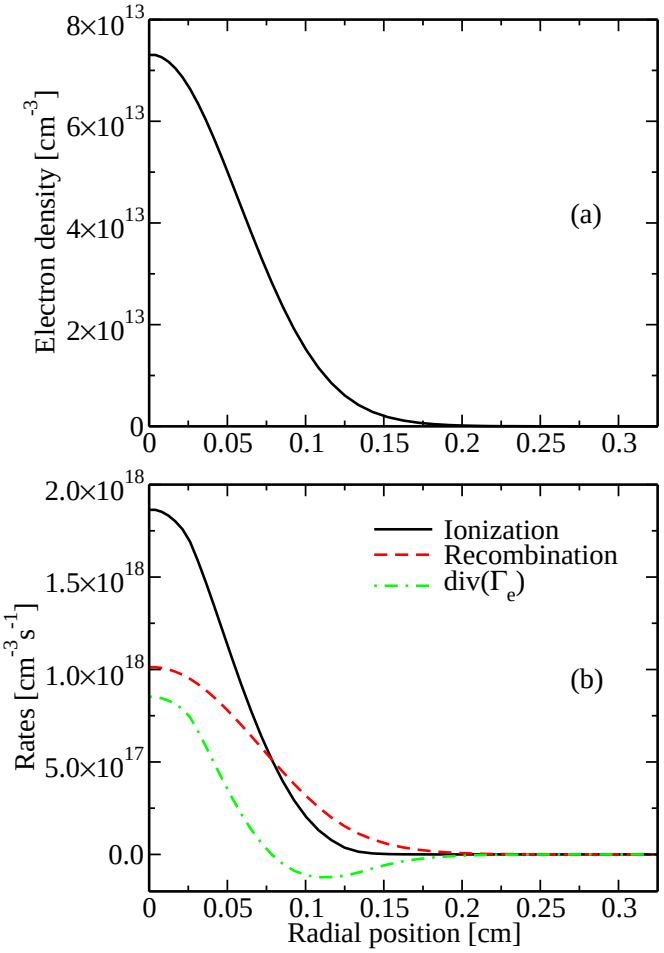

Figure 5.3: Radial profiles of the electron density (a) and of the electron rates (b) for xenon at $p = 50$ Torr and current 130 mA.

The corresponding radial distribution of the total ionization, the total recombination rate and their difference, i.e., the divergence of the electron flux, are illustrated in Fig. 5.3b. The results agree well with the diffusion-recombination theory [3] according to which the electron density profile approaches a contracted profile, if the ionization rate falls off more rapidly than the volume recombination rate.

The radial distribution of the mean electron energy at 50 Torr and 130 mA is illustrated in Fig. 5.4a. The mean electron energy is constant from the axis toward the $r/R \approx 0.5$ and it decreases over a residuary distance. Notice that the rough plot of the mean electron energy is not a radial grid effect. This is might be due to the rough resolution of the look-up tables used for the calculation of the electron transport and rate coefficients.

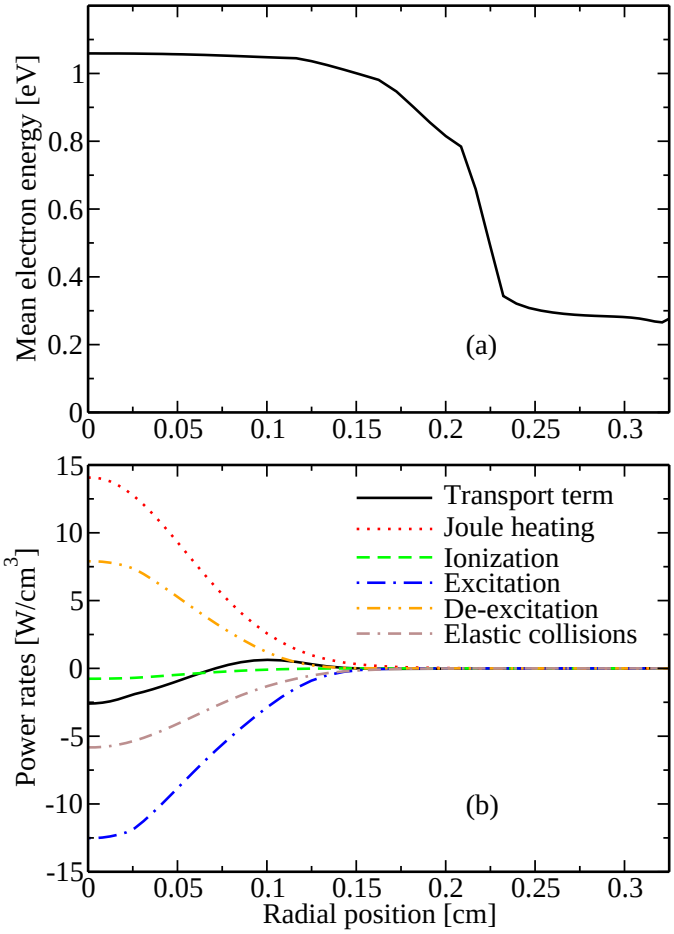

Figure 5.4: Radial profiles of the mean electron energy (a) and of the electron power rates (b) for xenon at $p = 50$ Torr and current 130 mA.

In Fig. 5.4b the most important contributions to the local electron power balance, i.e., the transport term $\partial(r\Gamma_\varepsilon)/(r\partial r)$, Joule heating, the gain rate S_{sc} due to superelastic collisions (de-excitation), and the loss rates due to elastic collisions,

excitation and ionization are shown as functions of the radial position for the pressure $p = 50$ Torr and the discharge current 130 mA. Further contributions, which are taken into account in the model, like "radial cooling", gain from three-body recombination, chemo-ionization processes and dissociative recombination, have negligible influence and, therefore, they were not plotted.

The dominant power gain process is the gain from the axial electric filed, while the contribution of the de-exciting electron collisions and the transport term has lower significance. Inelastic collisions due to excitation represent the main power loss mechanism for the electrons, while the elastic collisions have a factor of 2 smaller contribution. The ionization losses are almost negligible.

5.3 Sensitivity studies

The numerical solution obtained with mathematical model is different from reality. There are many errors, which are introduced during simulation of the gas discharge. Besides the discretization, the round-off and boundary errors, the most important sources of the errors are modelling errors and uncertainties of the atomic data. The modelling errors are results of the transformation of the real phenomena into mathematical equations. Other sources of modelling errors are neglected effects. Only major effects relevant to the present studies were included in the model. However, it is anticipated that errors introduced by modelling itself are less significant in comparison with uncertainties of the atomic data.

The majority of the cross sections and rate constants included into the collisional-radiative model are known with limited accuracy. Because of this, it is necessary to select the most important reactions which actually influence the evolution and the behaviour of the constricted glow discharge. In the present sensitivity studies the variation of the following input parameters are chosen: the rate coefficients of the stepwise ionization of the excited atoms [Tab. A.2 # 28-34], the rate coefficients of the excitation and de-excitation between excited levels [Tab. A.2 # 15-26], the rate coefficients of the dissociative recombination of the molecular ions [Tab.A.2 # 41-43], the rate coefficient of the conversion of the atomic ions into molecular ions [Tab. A.2 # 46] and heavy particle temperature dependence of the

rate coefficients of the dissociative recombination and three-body collisions [Tab. A.2 # 41-47, 49, 51]. Modelling of Xe dc discharge is used here for example.

The relative sensitivity $E_{i,j}^{rel.}$ of an output variable x_i with respect to an input parameter f_j can be calculated by varying this parameter and dividing the relative change of the result by the relative change of the parameter [118].

$$E_{i,j}^{rel.} = \frac{f_j \Delta x_i}{x_i \Delta f_j}. \tag{5.1}$$

The sensitivity analysis of xenon dc discharge are shown in Tab. 5.1 and obtained from the variation of the input parameters for a gas pressures 20 Torr, and a peak current of 130 mA.

Table 5.1: Sensitivity study of the axial electric field, electrons, metastable and resonance atoms, and mean electron energy at the axis on atomic data for a gas pressure 20 Torr, and a peak current of 130 mA.

Parameter variation	E_z	$n_e(0)$	$n_m(0)$	$n_r(0)$	$U_e(0)$
Stepwise ionization					
-10 %	-28.22 %	+12.92 %	-78.34 %	-78.02 %	-7.87 %
+10 %	+22.95 %	-14.70 %	+76.30 %	+74.99 %	+6.86 %
Excitation and de-excitation					
-10 %	+8.62 %	-6.59 %	-46.11 %	+31.31 %	-0.64 %
+10 %	-9.91 %	+0.81 %	+41.11 %	+25.79 %	+0.88 %
Dissociative recombination					
-10 %	+3.82 %	+19.33 %	+24.95 %	+27.65 %	+0.64 %
+10 %	-5.44 %	-22.21 %	-24.36 %	-27.76 %	-0.24 %
Ion conversion					
-10 %	+7.4 %	+36.05 %	+43.29 %	+48.58 %	+0.88 %
+10 %	-9.13 %	-38.10 %	-40.99 %	-46.64 %	-0.4 %
Temperature dependence					
-10 %	-7.09 %	+20.41 %	-26.79 %	+30.02 %	-0.8 %
+10 %	+4.83 %	+14.55 %	+23.87 %	+25.99 %	+1.12 %

The sensitivity analysis of xenon dc discharge are shown in Tab. 5.2 and obtained from the variation of the input parameters for a gas pressures 40 Torr, and a peak current of 130 mA.

Table 5.2: The same as in Tab. 5.1, but for a gas pressure 40 Torr, and a peak current of 130 mA.

Parameter variation	E_z	$n_e(0)$	$n_m(0)$	$n_r(0)$	$U_e(0)$
Stepwise ionization					
-10 %	-26.23 %	+13.32 %	-82.16 %	-82.3 %	-7.43 %
+10 %	+20.74 %	-10.54 %	+81.78 %	+82.04 %	+6.32 %
Excitation and de-excitation					
-10 %	+9.99 %	+0.1 %	-41.50 %	+31.44 %	-1.2 %
+10 %	-9.1 %	+0.03 %	+38.87 %	+29.55 %	+1.2 %
Dissociative recombination					
-10 %	+6.61 %	+18.16 %	+7.93 %	+9.3 %	+0.68 %
+10 %	-6 %	-14.73 %	-7.4 %	-8.7 %	-0.6 %
Ion conversion					
-10 %	+13.45 %	+40.75 %	+13.17 %	+16.74 %	+0.86 %
+10 %	-13.56 %	-31.2 %	-15.02 %	-17.83 %	-1.37 %
Temperature dependence					
-10 %	-12.22 %	+24.22 %	-16.27 %	+18.56 %	-1.8 %
+10 %	+11.45 %	+27.25 %	+14.67 %	+17.13 %	+1.55 %

In the following, sensitivity analysis with respect to a variation of the stepwise ionization, the excitation and de-excitation, the dissociative recombination, the ion conversion and heavy particle temperature dependence of the dissociative recombination and three-body collisions are reported. The results of Tabs. 5.1

and 5.2 are obtained from a variation of -10 % and +10 % of the input parameter. The results of this sensitivity analysis are as follows:

- The significant relative sensitivities of the excited atom densities are obtained especially with respect to variation of the rate coefficients of the stepwise ionization.
- The mean electron energy has the lowest relative sensitivity with respect to variation of the atomic data.
- The variation of the rate coefficients of the stepwise ionization as well as ion conversion have the largest influence on the behaviour of the dc xenon discharge.
- The growth of the total gas pressure has negligible influence on the relative sensitivities of the properties of the xenon dc discharge with respect to variation of the electron impact rate coefficients.
- The growth of the total gas pressure by factor of two leads to the decrease by factor of two of the relative sensitivity of the excited xenon atoms with respect to variation of the heavy particle impact rate coefficients.
- The relative sensitivities of the electron density as well as the mean electron energy only sightly charges with variation of the total gas pressure.

5.4 Pulsed xenon discharge

Model calculations for pulsed xenon plasmas have been performed in accordance with the experimental conditions of [116; 117]. Measurements have been carried out for gas pressures between 10 and 50 Torr and peak currents between 60 and 150 mA. In the present paragraph results for gas pressures between 10 and 50 Torr, peak currents between 100 and 150 mA and a pulse repetition frequency of 6 kHz with a duty cycle of 1:1 are reported.

Fig. 5.5 shows the temporal behaviour of the measured discharge current. At about $t = 4$ μs the sustaining voltage is switched on and an increase of the discharge current is observed. At about $t = 87$ μs the discharge is switched off

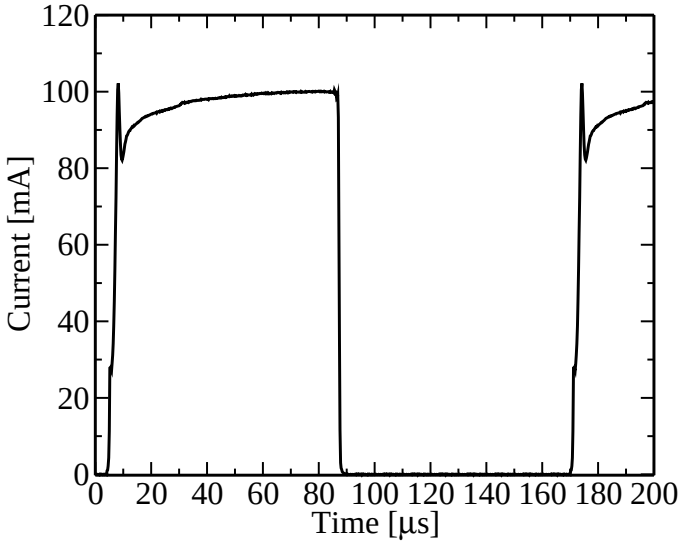

Figure 5.5: Temporal behaviour of the measured discharge current.

and the current drops from its peak value to zero within less than 1 μs. At $t = 170$ μs the sustaining voltage is switched on and cycle repeats. The measured current has been used as input for the model calculations.

5.4.1 Axial electric field

Fig. 5.6 illustrates the temporal variation of the axial electric field E_z for xenon pressures between 20 and 40 Torr and a peak current of 130 mA. The results obtained by means of standard fluid model have been compared with existing experimental data of [116; 117]. The results of the standard model agree well with the experimental data. They show an abrupt increase of the axial electric field E_z at about $t = 4$ μs. The axial electric field starts to decrease at about $t = 10$ μs. Within the time period from $t = 10$ and $t = 60$ μs discrepancies between theoretical and experimental data have been found. Such behaviour might be due to neglection of electrode regions in model assumming axially homogeneous electric field. The difference between both data increases with increasing of pressure. However, during the last 20 μs of the current-on phase good agreement between theoretical and experimental data has been obtained.

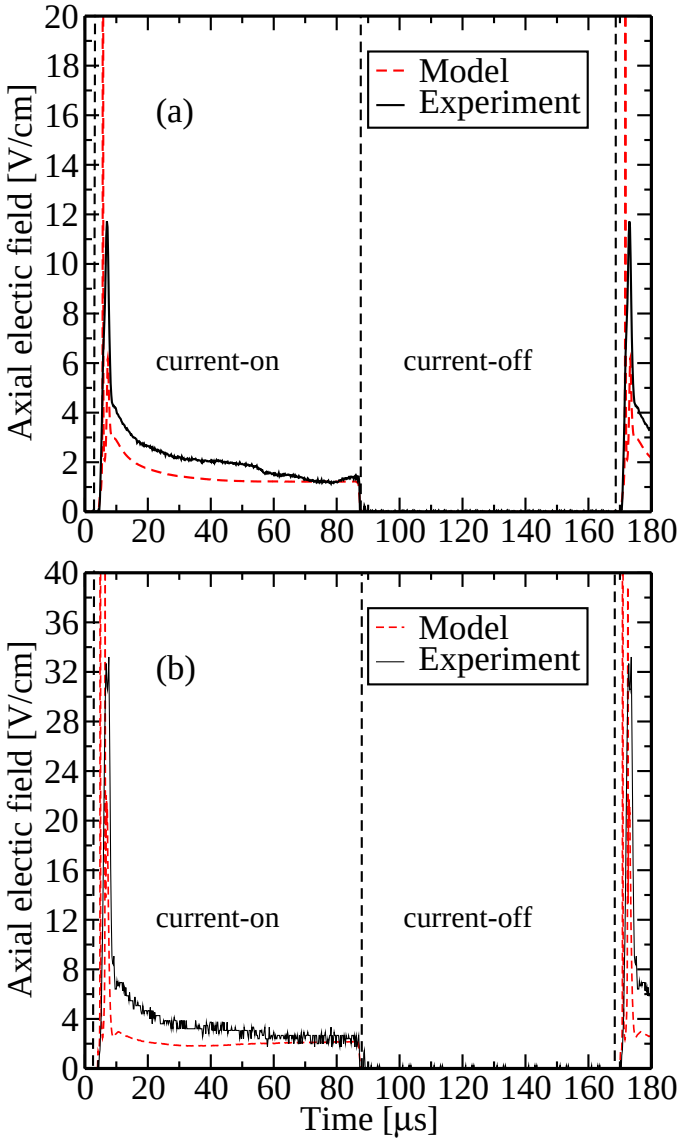

Figure 5.6: Temporal behaviour of the axial electric field for gas pressures (a) 20 Torr, (b) 40 Torr and a peak current of 130 mA.

5.4.2 Metastable atom density

Fig. 5.7 shows the temporal variation of the metastable atom density $Xe(1s_5)$ for xenon pressures between 20 and 40 Torr and a peak current of 130 mA. Results of the metastable density are represented by the density of the metastable atoms at the axis of the discharge column. The model predictions have been compared

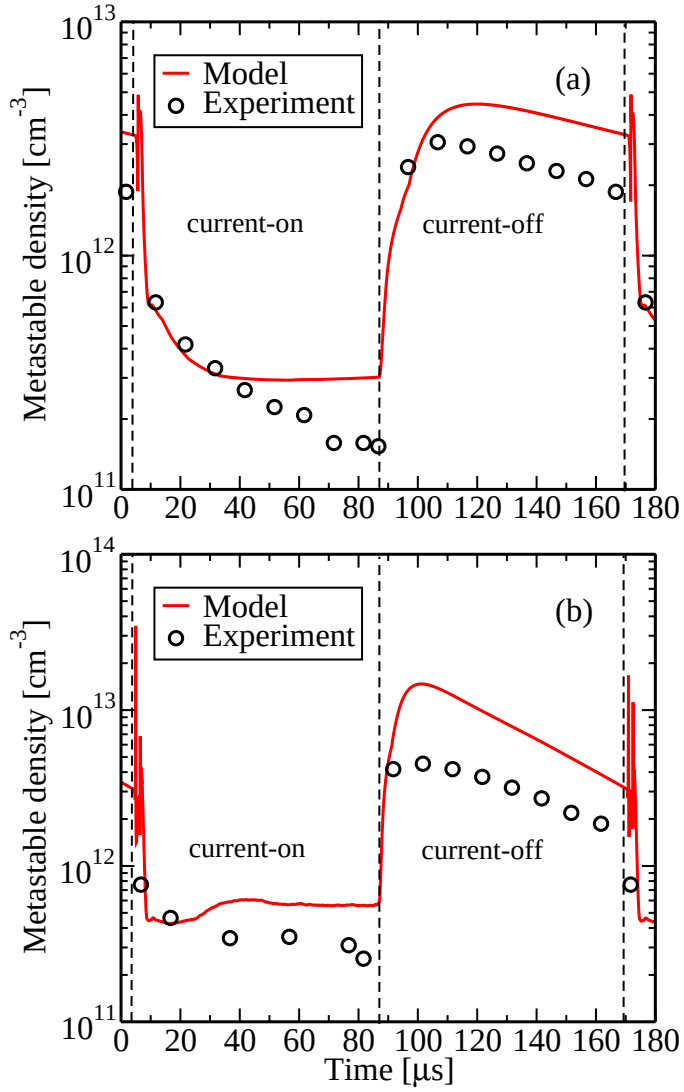

Figure 5.7: Temporal behaviour of the $Xe(1s_5)$ density for gas pressures (a) 20 Torr, (b) 40 Torr and a peak current of 130 mA.

with existing experimental data of [116]. They show a peak of the metastable density $Xe(1s_5)$ at about $t = 4$ μs, which is not observed in the experiment. The high axial electric field at the beginning of the discharge could be a reason for an enhanced population of metastable level. In the reignition phase of the discharge the metastable density slightly decreases for a gas pressure 20 Torr. However, for a gas pressure 40 Torr the metastable density slightly increases. The reason

could be an increased frequency of the ground state atom excitation, which leads to production of metastable atoms. During the afterglow phase of the discharge the metastable increases in comparison with the active phase of the discharge. The metastable density reaches maximum value then decreases. Increasing of the gas pressure leads to more considerable growing of metastable levels during the afterglow phase of the discharge. However, higher pressure leads to more faster decay of the metastable density after reaching the maximum value. The measured and calculated density of the metastable state agree well. The increase of the metastable density in the early afterglow is mainly caused by collision processes between $Xe(2p)$ and electrons, $Xe(2p)$ and ground state atoms and by radiation transitions from the $Xe(2p)$ states.

Fig. 5.8a shows the temporal variation of the metastable density at the axis of the discharge column for a xenon pressure 40 Torr and peak discharge currents between 100 and 150 mA. For considered range of peak current the temporal behaviour of axis values of the metastable density practically does not change. The calculated densities are in the range of $5 \cdot 10^{11} - 1.6 \cdot 10^{13}\,\mathrm{cm}^{-3}$ except the reignition region. In the current-off phase the metastable density at the axis of the discharge column becomes up to 30 times larger than in the active phase of the discharge. Growing of the peak current value leads to a small decrease of the maximum value and more slow decay of the metastable density during afterglow.

Fig. 5.8b illustrates the temporal variation of the metastable density at the axis of the discharge column for a peak current of a 130 mA and xenon pressures between 10 and 50 Torr. The population of the metastable level in the afterglow increases with growing of the gas pressure. Also, the time to reach the maximum density in the current-off phase is shortened by an increasing pressure. In particular, the maximum value of the metastable density at 30 Torr is reached after about 20 μs, whereas at 50 Torr only 10 μs are needed.

The observed peaks of the metastable density are connected with the production of high-lying excited atoms. These atoms are yielded by the dissociative recombination of the molecular ions. This recombination is strongly influenced by the dependence of the recombination coefficient on the "electron temperature". In the current-off phase of the discharge the "electron temperature" rapidly decreases due to the elastic collisions of electrons with the neutral gas. This leads

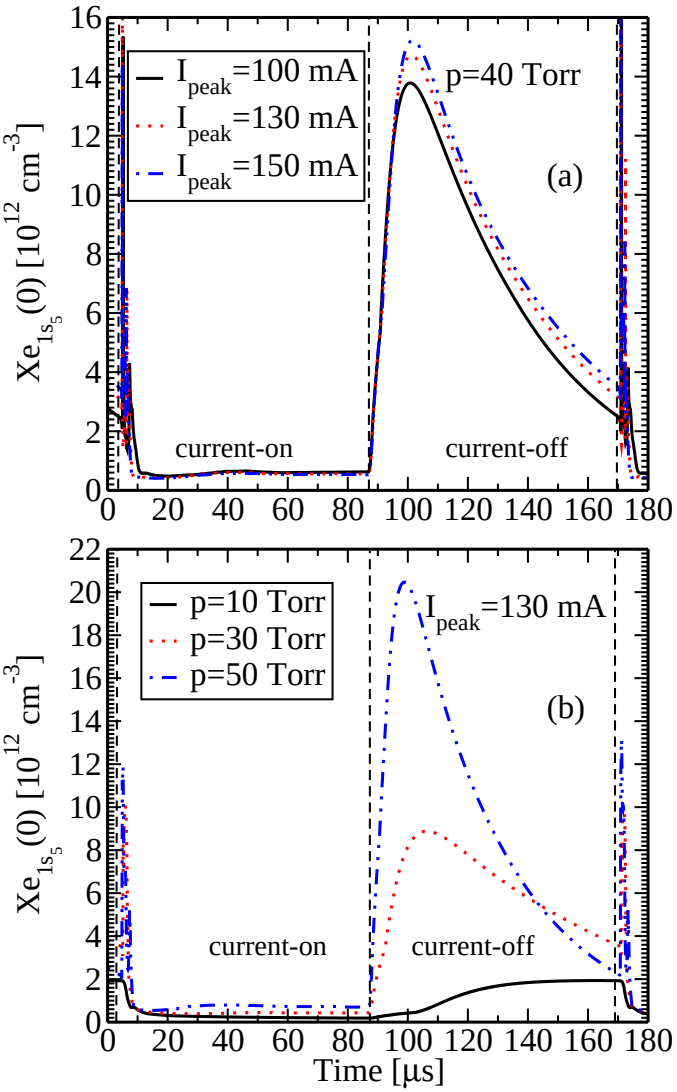

Figure 5.8: Temporal behaviour of the $Xe(1s_5)$ density at the axis of the discharge column (a) for a gas pressure 40 Torr and different peak currents, (b) for a peak current of 130 mA and different pressures.

to an increased recombination coefficient and consequently to an increased population of the high-lying excited atoms. The shortening of time needed to reach the maximum value of the metastable density can also be explained by the dependence of the recombination coefficient on the "electron temperature". With higher pressure the "temperature" will decay more rapidly and therefore the

metastable density reaches maximum much faster.

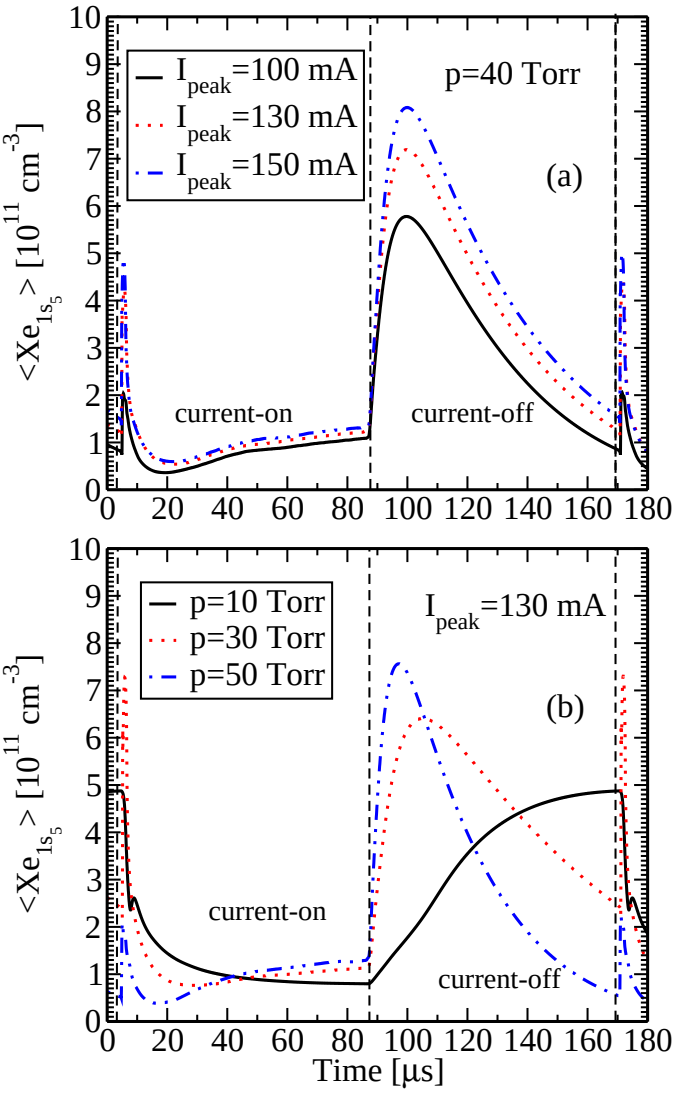

Figure 5.9: Temporal behaviour of the radially averaged $Xe(1s_5)$ density (a) for a gas pressure 40 Torr and different peak currents, (b) for a peak current of 130 mA and different pressures.

Fig. 5.9a shows the temporal variation of the radially averaged metastable density for a xenon pressure 40 Torr and peak discharge currents between 100 and 150 mA. The calculated metastable densities are in the range of $1 \cdot 10^{11} - 8 \cdot 10^{11}$ cm^{-3} except the reignition region. In the afterglow the radially averaged metastable

density becomes up to eight times larger than in the active phase of the discharge. Increase of the peak current value leads to a growth of the maximum value of the radially averaged metastable density. Consequently, growing of the peak current value leads to a broadening of the radial profile of metastable density during afterglow.

Fig. 5.9b illustrates the temporal variation of the radially averaged metastable density for a peak current of a 130 mA and xenon pressures between 10 and 50 Torr. Increasing of the gas pressure leads to the growing of the density of the radially averaged metastables during current-off phase. However, the ratio between maximum values of radially averaged densities for different pressures is smaller in comparison with ratio between maximum values of densities at the axis during the afterglow. Consequently, increasing of the gas pressure leads to a narrowing of the radial profile of metastable density during current-off phase.

Fig. 5.10 illustrates radially averaged temporal gain and loss rates of the metastable atoms $Xe(1s_5)$ for a gas pressure 40 Torr and a peak current of 130 mA. During current-on phase of the discharge the dominant loss rates are electron impact excitations of the $Xe(1s_5)$, which leads to productions of two high-lying levels: $Xe(2p_{10})$ and $Xe(2p_{9..5})$. The reverse processes are smaller in comparison with direct one. The electron impact gain reactions are supplemented with four heavy particle reactions (de-excitation of high-lying levels) as well as two radiation transitions from $Xe(2p_{10})$ and $Xe(2p_{9..5})$ levels. The gain and loss transitions between $Xe(1s_5)$ and high-lying levels compensate each other during the current-on phase of the discharge. Therefore, the main gain process of the metastable atoms $Xe(1s_5)$ during active phase of the discharge is electron impact excitation of the ground state atoms.

Current switch-off leads to decrease by one order of magnitude of the total gain and loss rates from $10^{18}\,\mathrm{cm^{-3}s^{-1}}$ in the active phase of the discharge to $10^{17}\,\mathrm{cm^{-3}s^{-1}}$ in the early afterglow. The electron density remains large in the early period of the afterglow. Thus, electron impact reaction dominate in this period. In particular, the dominant loss rates are electron impact excitation to two high-lying levels: $Xe(2p_{10})$ and $Xe(2p_{9..5})$. In the early afterglow the major gain rate is electron impact de-excitation from $Xe(2p_{10})$ level. Dissociative recombination of the molecular ions enhances population of the high-lying levels.

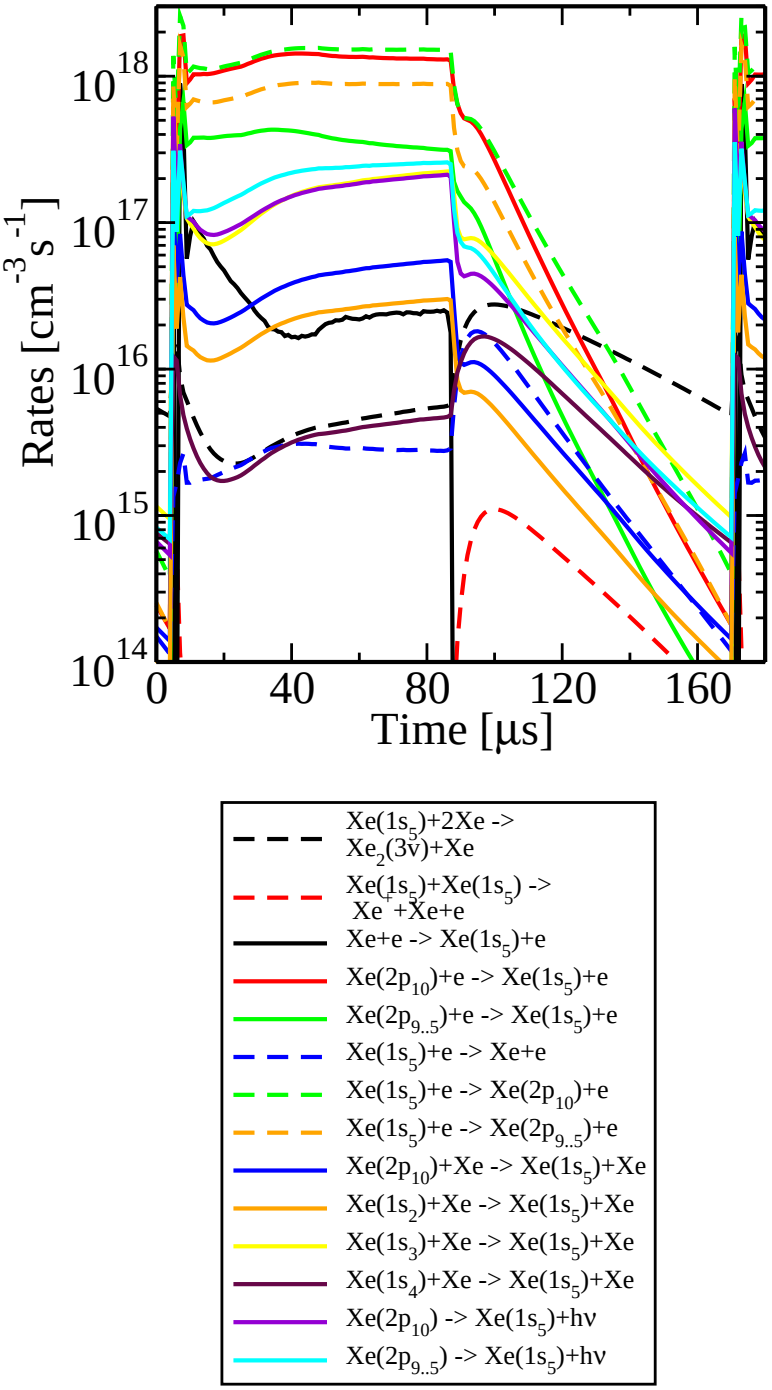

Figure 5.10: The calculated temporal evolutions of the radially averaged generation and loss rates of the metastable atoms $Xe(1s_5)$ for a gas pressure 40 Torr and a peak current of 130 mA.

These levels are instantly de-excited by collisions with electrons and ground state atoms as well as by radiation transitions. The total gain rates of $Xe(1s_5)$ are larger than the total loss rates in the early afterglow. Such behaviour leads to an abrupt increase of the metastable atom densities right away after current switch-off. During the afterglow the molecular ion density and electron density experiences fast decay, which, consequently, leads to fast decrease of the gain and loss rates. At about $t = 120$ μs the dominant loss reaction of the metastable level $Xe(1s_5)$ becomes three-body collision with two ground state atoms, which leads to production of excimers. More slow decay of this reaction rate in comparison with other gain reactions as well as higher absolute value leads to faster decrease of the metastable density $Xe(1s_5)$ during the late period of the afterglow.

5.4.3 Resonance atom density

Fig. 5.11 illustrates the temporal variation of the resonance atom density $Xe(1s_4)$ for xenon pressures between 20 and 40 Torr and a peak current of 130 mA. Results of the resonance density are represented by the density of the resonance atoms at the axis of the discharge column. The simulation results have been compared with existing experimental data of [116]. Similarly to the metastable density the resonance density has the same qualitative behaviour during the current-on and current-off phases of the discharge. However, the metastable density are three to four times higher than the resonant density. Also, the growing of the resonance density during afterglow is less pronounced in comparison with the metastable density.

The temporal evolutions of the radially averaged gain and loss rates of the resonance atoms $Xe(1s_4)$ are shown in Fig. 5.12 for a gas pressure 40 Torr and a peak current of 130 mA. In general temporal dependencies of the gain and loss rates of the resonance atoms $Xe(1s_4)$ are qualitatively the same as for the metastable atoms $Xe(1s_5)$. During the active phase of the discharge exciting and de-exciting collisions between $Xe(1s_4)$ and high-lying levels equilibrates each other. Additionally the resonance atoms are depopulated by the radiation transition to the ground state. As in case of $Xe(1s_5)$, population of the resonance atoms $Xe(1s_4)$ depends on electron impact excitation of the ground state atoms.

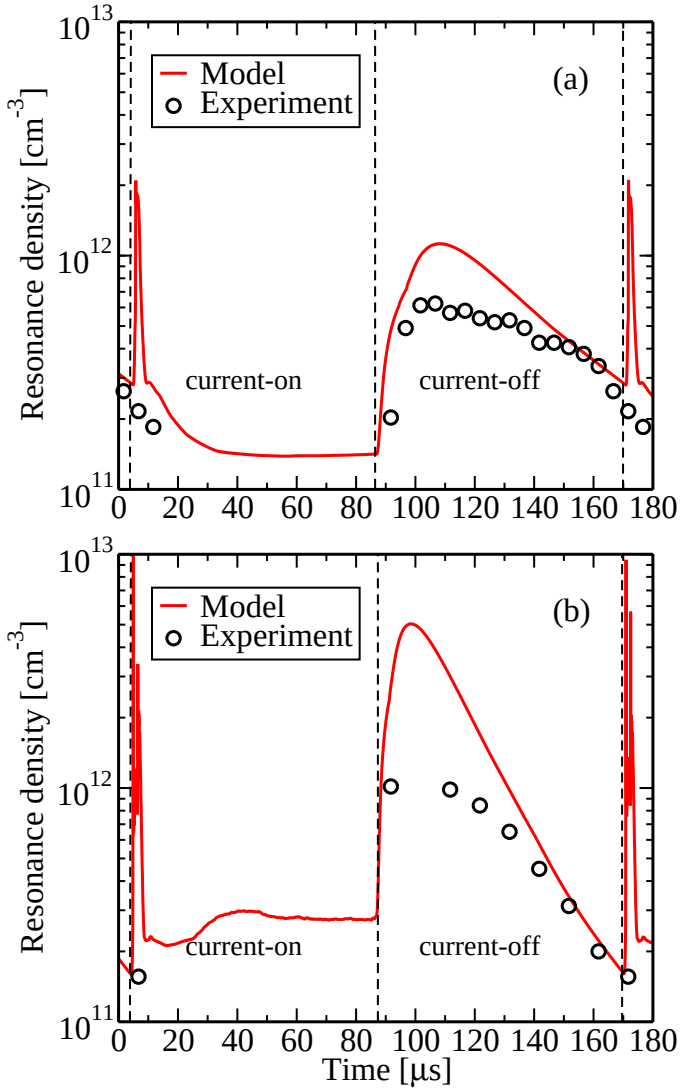

Figure 5.11: Temporal behaviour of the $Xe(1s_4)$ density for gas pressures (a) 20 Torr, (b) 40 Torr and a peak current of 130 mA.

In the early afterglow the density of the resonance atoms grows due to prevalence of de-exciting reactions between $Xe(1s_4)$ and high-lying levels over exciting ones. After reaching maximum value the resonance density decays similarly to the metastable density. Three-body reactions between $Xe(1s_4)$ and two ground state atoms has lower significance in total loss budget during the afterglow. At about $t = 110$ μs the dominant loss reaction of the resonance level $Xe(1s_4)$ be-

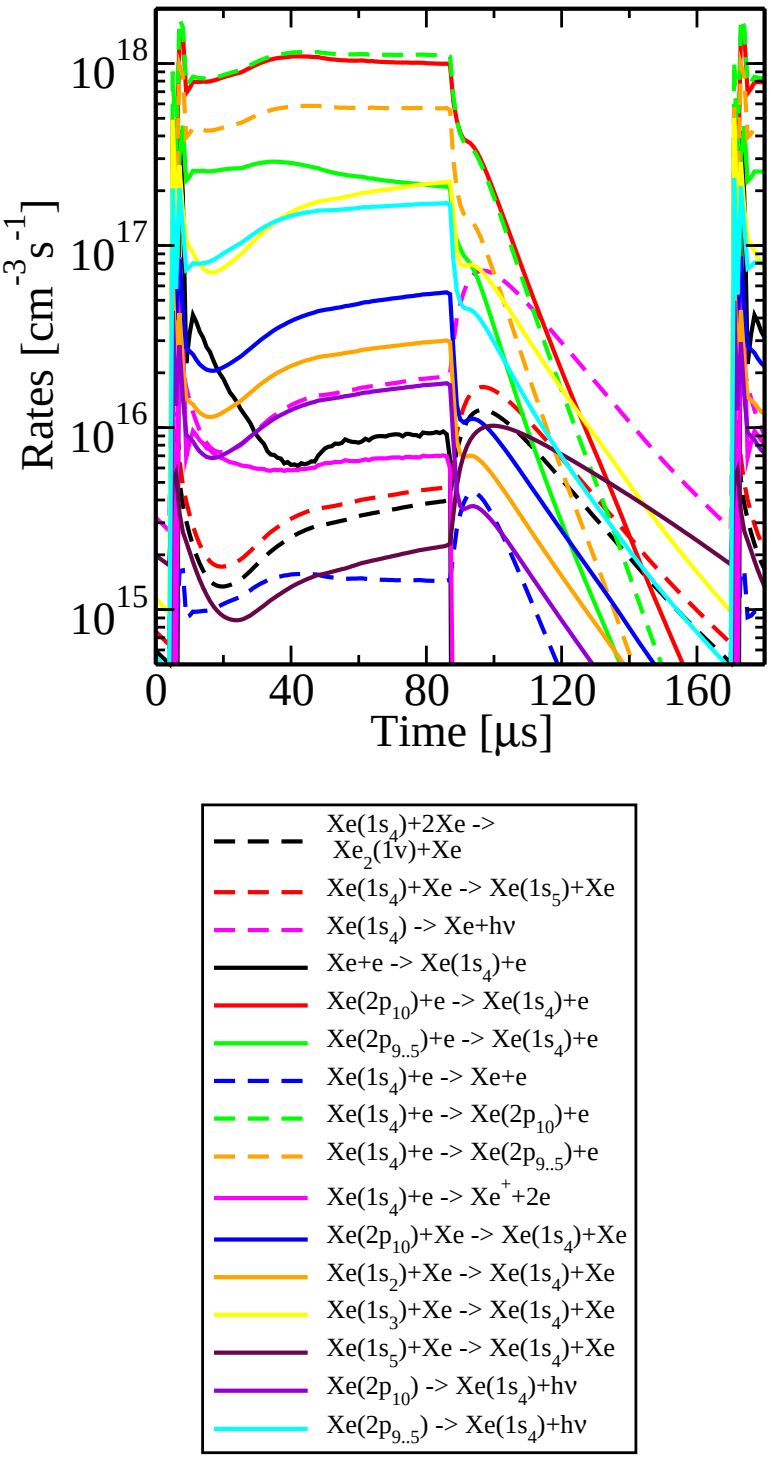

Figure 5.12: The calculated temporal evolutions of the radially averaged generation and loss rates of the resonance atoms $Xe(1s_4)$ for a gas pressure 40 Torr and a peak current of 130 mA.

comes the radiation transition to the ground state. Presence of this reactions leads to much faster decay of the resonance atoms in comparison with metastable ones during the afterglow phase of the discharge.

5.4.4 Excimer densities

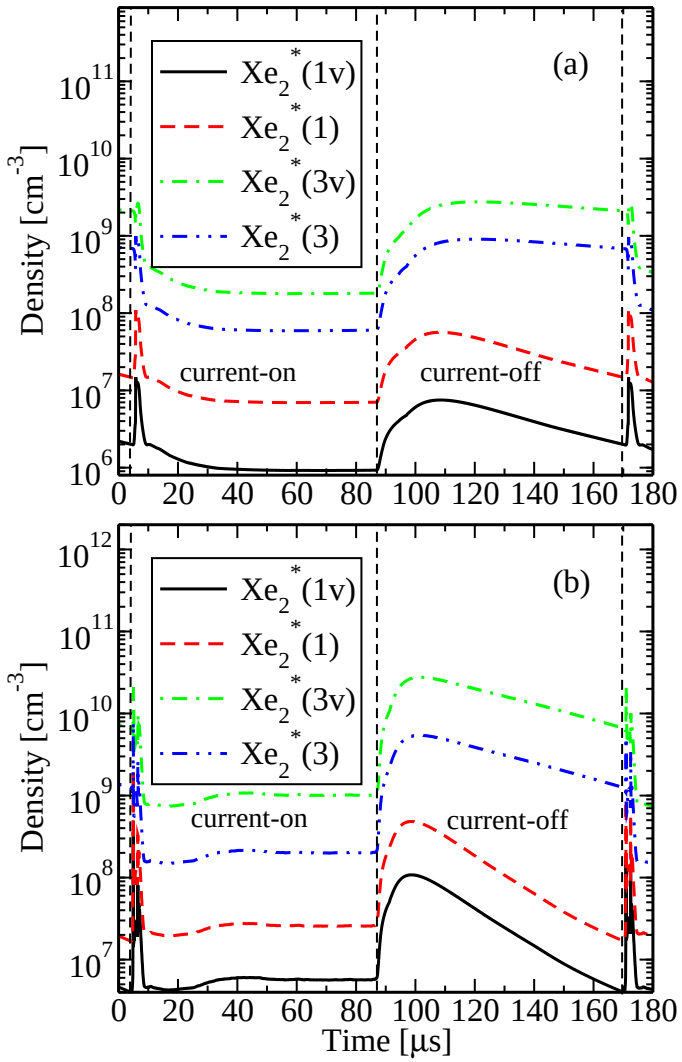

Figure 5.13: Temporal behaviour of excimer densities for gas pressures (a) 20 Torr, (b) 40 Torr and a peak current of 130 mA.

An instant increase of the VUV radiation of the so-called first and second

continuum around 151 and 172 nm has been measured in the afterglow [116]. This radiation is due to the radiative decay of the higher and of the relaxed lowest vibrational states of the Xe_2^* excimers. Such increase is confirmed by the results of the model calculation of the temporal variation of excimer densities [Fig. 5.13]. The analysis of the theoretical results indicates that the metastable $Xe(1s_5)$ and resonance $Xe(1s_4)$ atoms play the role of the precursor for the VUV radiation. The $Xe(1s_5)$ and the $Xe(1s_4)$ states decay via three-body collisions to vibrationally excited excimer states, according to the following reactions:

$$\begin{aligned} Xe(1s_5) + 2Xe &\rightarrow Xe_2^*(3v) + Xe \quad , \\ Xe(1s_4) + 2Xe &\rightarrow Xe_2^*(1v) + Xe \quad . \end{aligned}$$

In the next step the highly-excited excimer molecules undergo vibrational relaxation

$$\begin{aligned} Xe_2^*(3v) + Xe &\rightarrow Xe_2^*(3) + Xe \quad , \\ Xe_2^*(1v) + Xe &\rightarrow Xe_2^*(1) + Xe \quad . \end{aligned}$$

The radiative decomposition of these excited excimer states leads to the radiation of the first and second continuum around 151 and 172 nm

$$\begin{aligned} Xe_2^*(1v) &\rightarrow 2Xe + h\nu(151 \text{ nm}) \quad , \\ Xe_2^*(1) &\rightarrow 2Xe + h\nu(172 \text{ nm}) \quad , \\ Xe_2^*(3v) &\rightarrow 2Xe + h\nu(151 \text{ nm}) \quad , \\ Xe_2^*(3) &\rightarrow 2Xe + h\nu(172 \text{ nm}) \quad . \end{aligned}$$

Fig. 5.13 shows the temporal variation of excimer densities for xenon pressures between 20 and 40 Torr and a peak current of 130 mA. Results of excimer densities are represented by densities of excimers at the axis of the discharge column. An instant growth of the xenon excimer states is observed after current switching-off, which leads to increase of the VUV radiation and confirms experimental results. Such behaviour is more pronounced at higher pressure. The xenon excimer state densities increase by approximately one order of magnitude. The temporal behaviour of excimers states qualitatively the same as their precursors. In particular, the decay velocity of the $Xe_2^*(1v)$ and the $Xe_2^*(1)$ is larger than that of the the $Xe_2^*(3v)$ and the $Xe_2^*(3)$ during the afterglow.

5.4.5 Electron density

Fig. 5.14 illustrates the temporal variation of the radial distributions of the electron density normalized to axis density $n_e(0)$ for a peak current 130 mA, gas pressures 10 Torr and 40 Torr. The instants $t = 10$ μs, $t = 50$ μs, and $t = 85$ μs represent early reignition, the middle and end of the active phase of the discharge, respectively. The moments $t = 125$ μs and $t = 165$ μs represent the middle and end of the afterglow of the discharge, respectively.

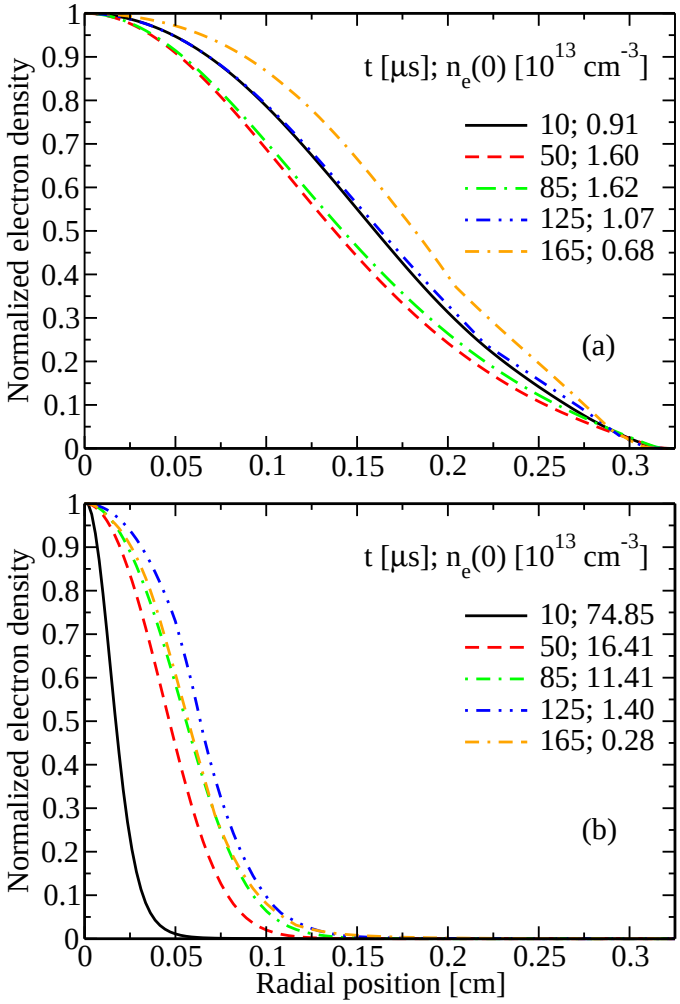

Figure 5.14: Radial profiles of the normalized electron density for a peak current 130 mA, gas pressures (a) 10 Torr and (b) 40 Torr and various phases.

At lower pressure during the active phase of the discharge the axis value of the electron density reaches maximum at about $t = 50$ μs [Fig. 5.14a]. Until the end of the active phase $n_e(0)$ slightly decreases. The radial profile of the electron density is broad and remains practically the same during current-on phase. During the afterglow phase of the discharge the absolute value of the electron density decreases exponentially and becomes approximately two times lower. The half-width of the electron density profile increases approximately by a factor of 1.5.

At higher pressure during the active phase of the discharge the axis value of the electron density reaches the maximum much faster at about $t = 10$ μs [Fig. 5.14b]. After the reaching of the maximum value $n_e(0)$ decays exponentially and becomes approximately six times lower at the end of the active phase of the discharge. Instantly after the reignition of the discharge the characteristic radius of the plasma filament becomes approximately two times narrower. Decreasing the axis value of the electron density is supplemented with broadening of the radial profile. At the end of the active phase of the discharge the half-width of the plasma filament is smaller for the higher pressure than lower one. Such behaviour is due to much higher nonlinear dependence of the ionization rate on electron density. Also, at higher pressure the volume recombination processes are higher than for lower one. During the afterglow of the discharge the absolute value of the electron density decay more rapidly in comparison with lower pressure because of increased production of the molecular ions. The electron density decreases by more than one order of magnitude. However, the normalized radial profile remains the same during the afterglow of the discharge. This is due to domination of the volume recombination processes over surface one during the considered time range.

In order to evaluate the various contribution to the electron production and destruction, Fig. 5.15 shows radially averaged temporal gain and loss rates of the electrons for a gas pressure 40 Torr and a peak current of 130 mA. An increase of the discharge current leads to an abrupt growing of the electron production due to the stepwise ionization. Ionization from the ground state is not shown due to the negligible contribution to the total ionization budget. Also, the electron gain rate due to the chemoionization is insignificant. In the early current-on phase

the major loss rate is the ambipolar diffusion to the wall. The contribution to the electron losses due to ambipolar diffusion decreases with time but remains significant. At about $t = 50$ μs the dominant loss rate of the electrons becomes the dissociative recombination of the molecular ions. This process is compensated by the stepwise ionization till end of the current-on phase. The losses due to three-body recombination and dissociative recombination of the Xe_3^+ are insignificant during the active phase of the discharge.

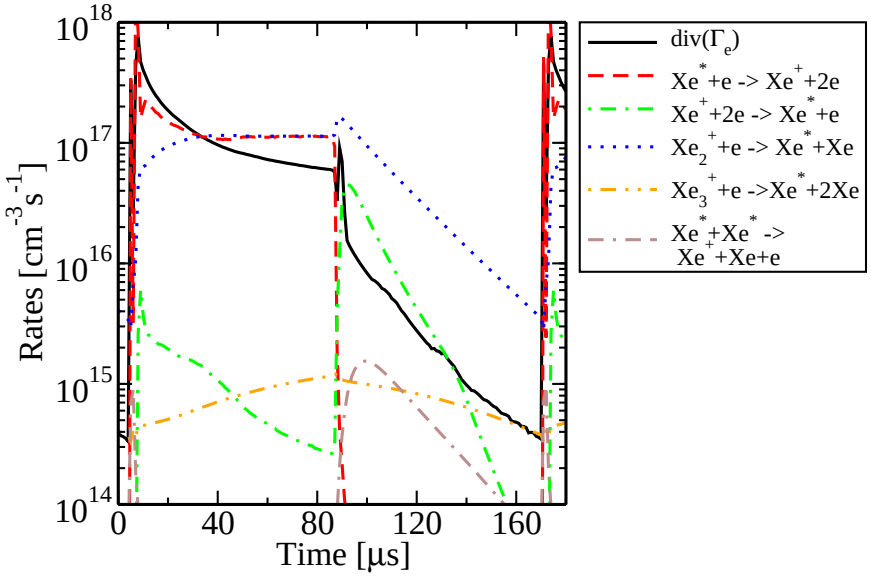

Figure 5.15: The calculated temporal evolutions of the radially averaged generation and loss rates of the electrons for a gas pressure 40 Torr and a peak current of 130 mA.

Switching-off of the discharge current leads to an abrupt decrease of the electron production due to the stepwise ionization. The generation of the electrons by the chemoionization increases during the afterglow but remains much smaller than loss processes. The dominant loss mechanism of the electrons is dissociative recombination of the Xe_2^+ during the the afterglow. This process experiences maximum right away after current switch-off. The reason of such behaviour is an instant decrease of the mean electron energy, which leads to the growing of the dissociative recombination rate. Using the same reason the behaviour of the three-body recombination can be explained. The loss rate experiences increase by

more than two order of magnitude. At about $t = 100$ μs the three-body recombination rate reaches the maximum value and predominates over the ambipolar diffusion. However, after 10 μs the three-body recombination rate becomes lower than ambipolar diffusion and decreases much faster. The loss due to dissociative recombination of the Xe_3^+ is almost insignificant during the afterglow of the discharge.

5.4.6 Molecular ion density

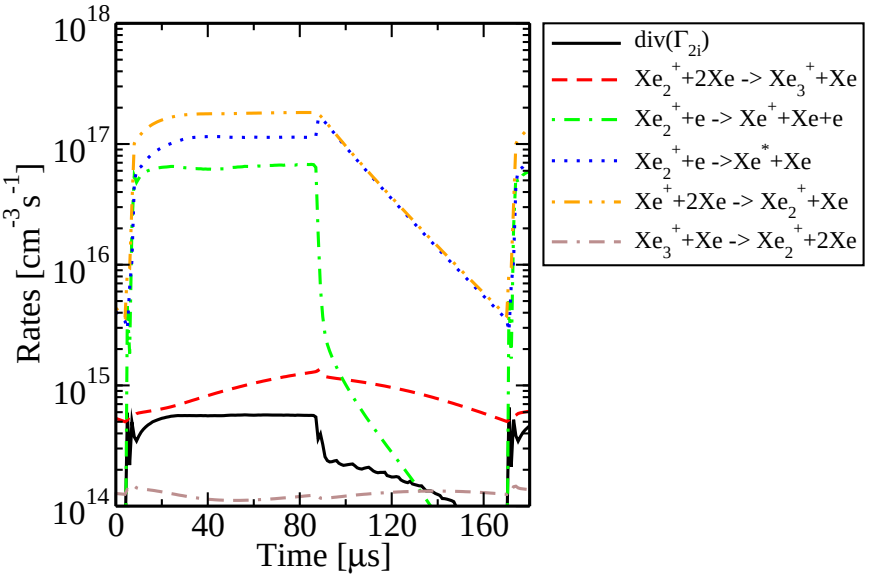

Figure 5.16: The calculated temporal evolutions of the radially averaged generation and loss rates of the molecular ions Xe_2^+ for a gas pressure 40 Torr and a peak current of 130 mA.

The temporal evolutions of the radially averaged gain and loss rates of the molecular ions are shown in Fig 5.16 for a gas pressure 40 Torr and a peak current of 130 mA. During the active phase of the discharge the dominant production rate of the molecular ions is conversion from atomic ions. This gain process is compensated by two loss processes: the dissociative recombination of the molecular ions and the conversion of Xe_2^+ to the atomic ions by electron impact. An abrupt decrease of the mean electron energy leads to instant decrease of the conversion

rate of the molecular ions to Xe^+ by electron impact during the afterglow. Thus, all molecular ions, which were created by the reactions of the atomic ions with two ground state atoms are immediately lost due to the dissociative recombination processes. Conversion of the molecular ions to Xe_3^+, reverse process and flux term are insignificant during the active and the afterglow phase of the discharge.

5.4.7 Mean electron energy

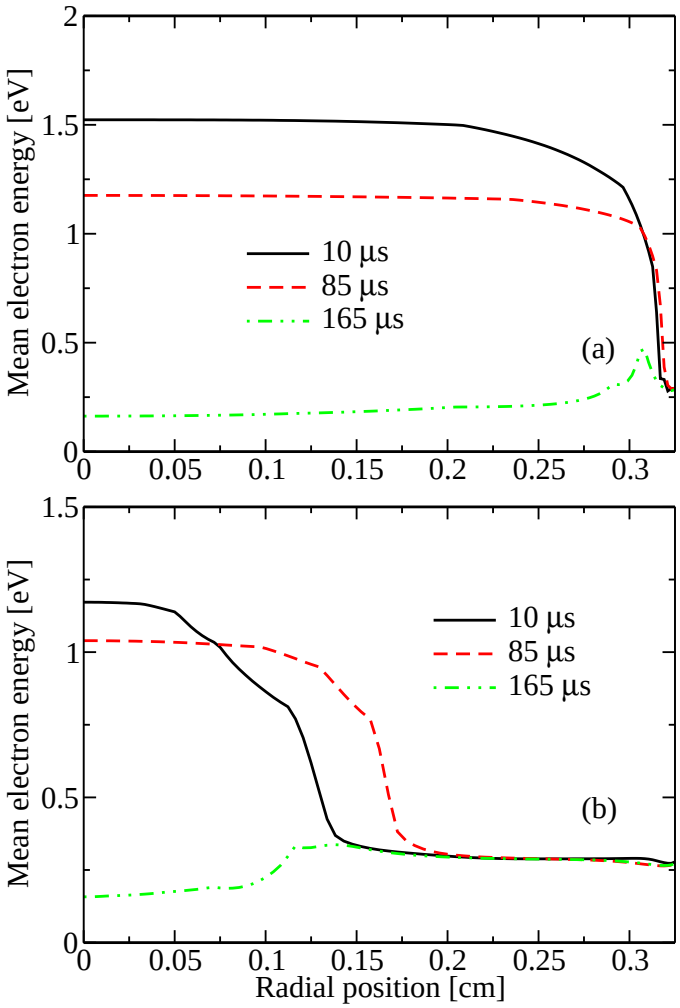

Figure 5.17: Radial profiles of the mean electron energy for a peak current 130 mA, gas pressures (a) 10 Torr and (b) 40 Torr and various phases.

Fig. 5.17 shows the temporal variation of the radial distributions of the mean electron energy for a peak current 130 mA, gas pressures 10 Torr and 40 Torr. The instants $t = 10$ μs and $t = 85$ μs represent early reignition and end of the active phase of the discharge, respectively. The moment $t = 165$ μs represents the end of the afterglow of the discharge.

At lower pressure during the active phase of the discharge the axis value of the mean electron energy decreases while the half-width remains the same [Fig. 5.17a]. This is direct consequence of the electron density behaviour during the current-on phase. During the afterglow phase of the discharge the absolute value of the mean electron energy decreases and becomes approximately three times lower. This is due to the absence of the axial electric field during current-off phase.

A similar behaviour in the radial variations of the mean electron energy is observed for the two pressures of 10 and 40 Torr. The active phase of the discharge at higher pressure is characterized by the lower value of the mean electron density on axis and by more constricted radial profile [Fig. 5.17b]. The reason of such behaviour is variation of the electron density during the current-on phase. At higher pressure the axis value of the electron density becomes higher and the radial profile becomes more constricted.

In Fig. 5.18, the important contribution to the local electron power balance, i.e., the transport term $\partial(r\Gamma_\varepsilon)/(r\partial r)$, Joule heating, the gain rates due to chemoionization S_{ci}, superelastic collisions (de-excitation) S_{sc}, three-body recombination S_{r3} and the loss rates due to "radial cooling" $e_0\Gamma_e E_r$, elastic collisions, excitation, ionization, and dissociative recombination of electrons are shown as functions of the radial position at $p = 10$ Torr, for peak current $I = 130$ mA, at $t = 10$, $t = 85$ and $t = 165$ μs. The three different times represent the begin of the current-on phase, the end of the active phase and the end of the current-off phase, respectively.

During the active phase of the discharge [Figs. 5.18a, 5.18b], the dominant power gain process is the gain from the axial electric field, while the contribution of the transport term and superelastic electron collisions is less significant. The chemoionization and three-body recombination gains are almost negligible at the end of the current-off phase. Inelastic losses due to excitation represent the main

power loss mechanism for the electrons, while elastic collisions have about 3 times smaller contribution. The losses due to ionizing collision processes, dissociative recombination and "radial cooling" are of minor importance. The magnitude of the power gain by Joule heating and de-exciting collisions is smaller than power losses in the discharge core, and it slightly exceeds the losses in the outer column part. The difference between these terms in the mean electron energy balance in the core region is compensated by the transport term. During the active phase of the xenon pulsed discharge the qualitative picture of the mean electron energy balance is the same as for constricted argon dc discharge [Figs. 4.17b and 4.17c]. The electron power component is also nonlocal. The energy flux is inward directed in the constricted plasma core and transfers energy from the outer to inner parts of the column.

The picture change completely in the afterglow phase of the discharge [Fig. 5.18c]. The absolute values of the main power contributions at the discharge axis have decreased by about two orders of magnitude compared with the active phase of the discharge in Fig. 5.18b. The absence of the axial electric field leads to vanishing of the Joule heating. Thus, the dominant power gain process becomes superelastic electron collisions, while the gain from the three-body recombination has smaller contribution. The gains due to chemoionizing collisions are of minor importance during the afterglow for considered discharge conditions. During current-off phase, the electron power is dissipated mainly in elastic collisions and to a lesser extent in exciting collisions. The losses due to dissociative recombination and ionization are of minor importance. "Radial cooling" has considerable importance only near the wall, where it is compensated by transport term. In the afterglow, the magnitude of the power gain by de-exciting collisions and three-body recombination is larger than that of elastic and inelastic losses in the discharge core, and it is slightly smaller in the outer column part. Similarly to the active phase, the large difference between these terms in the mean electron energy balance in the core region is compensated by the transport term. However, the energy flux is outward directed in the plasma core and transfers energy from the inner to outer parts of the column during the afterglow phase of the discharge.

Fig. 5.19 illustrates the corresponding contributions to the electron power balance for a peak current 130 mA and a pressure of 40 Torr, at $t = 10$, $t = 85$ and $t = 165$ μs. A similar behaviour in the radial variations of the different contributions is observed for the two pressures of 10 and 40 Torr with larger absolute values and more constricted profiles at higher pressure. Contrary to the lower pressure, the transport term has negative sign near the axis at the active phase of the discharge [Figs. 5.19a, 5.19b], and is attributed to the prevalence of the power gains over losses. As shown in Fig. 5.19c, the absolute values of the main power contributions at the discharge axis decay much faster with increasing of the gas pressure. Faster decrease of the electron density during afterglow at higher pressure leads to lower contribution of the three-body recombination power rates. Higher pressure is accompanied by a larger power gain in chemoionizing collisions, which is caused by considerable production of the metastable and resonance atoms during afterglow phase of the discharge. With increasing pressure the importance of the dissociative recombination power losses increases. Contrary to the lower pressure, "radial cooling" is of minor significance.

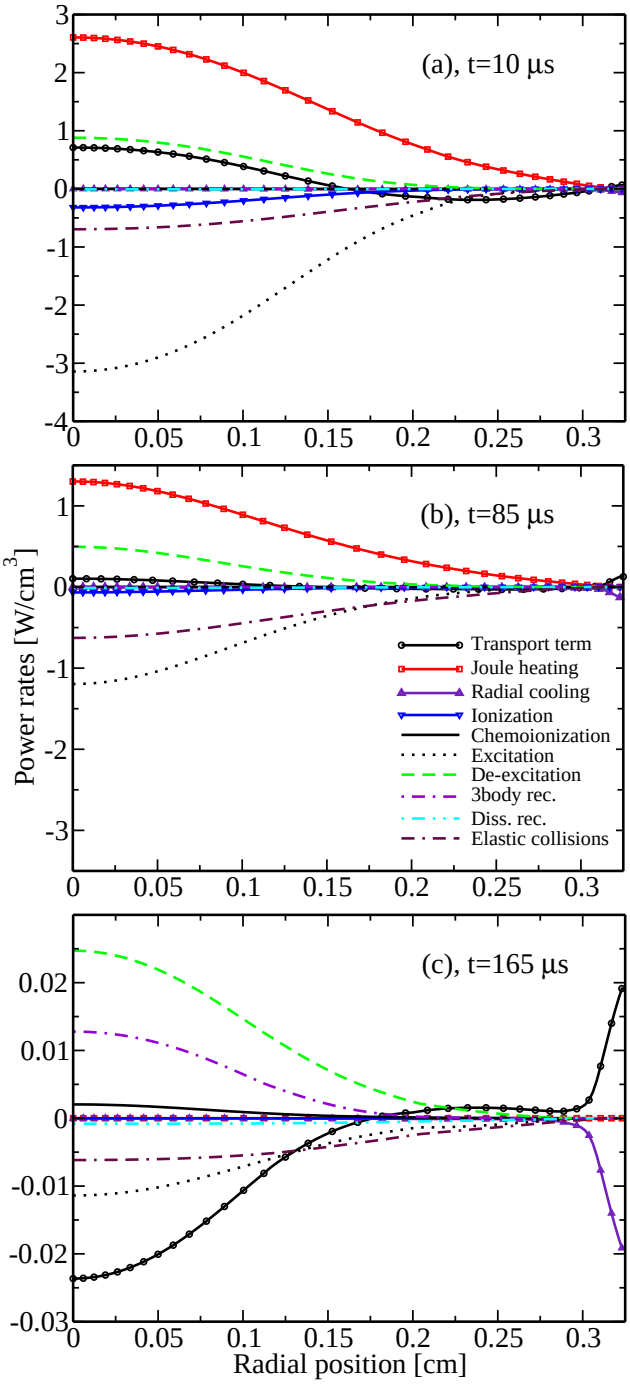

Figure 5.18: Contributions to the electron power balance as a function of the radial position at $p = 10$ Torr, for peak current $I = 130$ mA, at (a) $t = 10$, (b) $t = 85$ and (c) $t = 165$ μs.

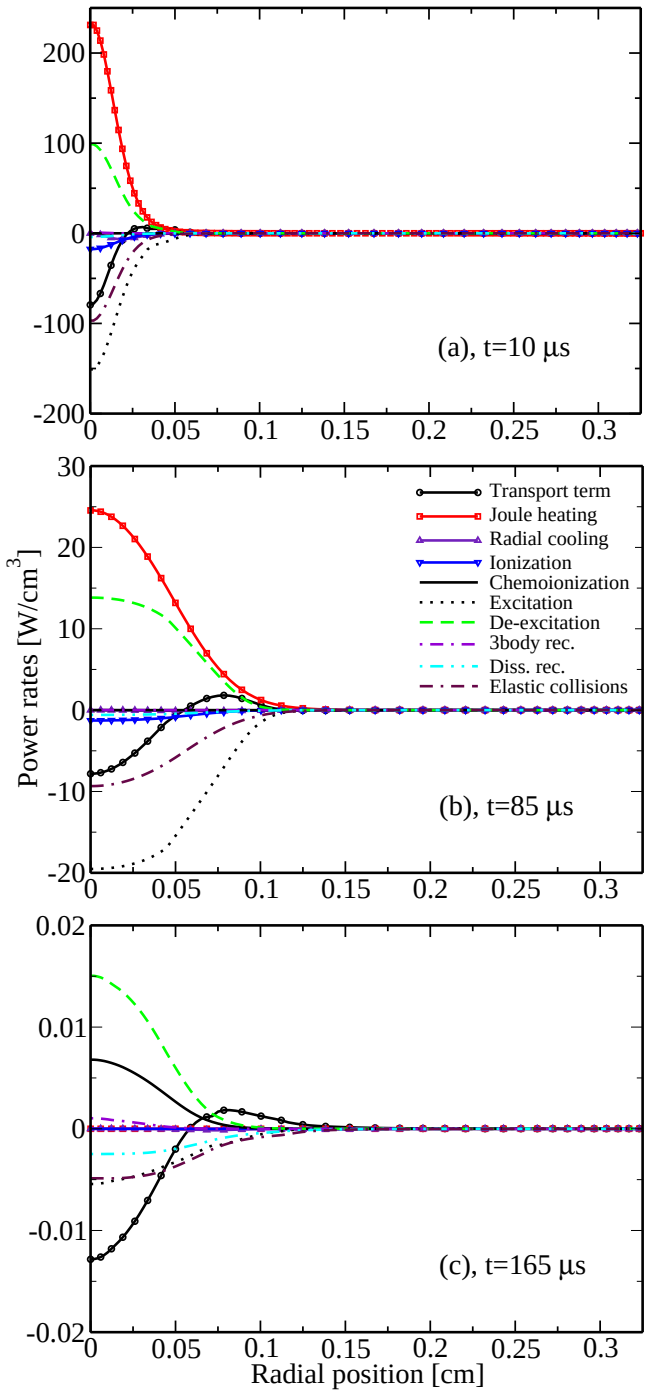

Figure 5.19: Quantities as in Fig. 5.18 but for a pressure of 40 Torr.

6 Conclusions and outlook

The positive column in rare-gas plasmas during glow-to-arc transition has been studied by a new time- and radial-dependent fluid model. This model consists of the coupled solution of the balance equations for the neutral and charged species, the mean electron energy, and the heavy particle temperature in the plasma, and a current balance determining the axial electric field. Assuming an axially and azimuthally homogeneous plasma in cylindrical geometry, the radial structure is taken into account and Poisson's equation for the space-charge potential is solved in addition.

The model adopts the nonlocal moment method, i.e., the system of the balance equations resulting from the moments of the time- and radially dependent Boltzmann equation is solved. The electron transport and rate coefficients are applied in dependence on the mean energy of the electrons, the heavy particle temperature, and the ionization degree. For the given gas, the model involves the solution of the steady-state spatially homogeneous Boltzmann equation and its coupling with the the space-time profiles of the electron mean energy, the heavy particle temperature, and the degree of ionization. The transport coefficients of the ions are adapted as as functions of the reduced electric field. For the argon discharge 9 species, 28 collision processes as well as 5 radiative processes are considered in the collisional-radiative model. 16 species, 76 collision processes as well as 12 radiative processes are included in the collisional-radiative model for the xenon discharge. The drift-diffusion approximation has been used for both the electron particle and energy fluxes, which includes the flux due to the electric field (drift) and the flux due to density gradients (diffusion). The flux boundary conditions have been employed for the charge carriers and mean electron energy of electrons, which contains the term due to direct drift and term due to random

motion. Additionally, the influence of the reflection from the boundary has been taken into account. In addition, model calculations using rate and transport coefficients of the electrons using the Maxwellian as well as the Druyvesteyn energy distribution have been performed.

The fluid equations are numerically solved by means of a finite-difference method. In order to describe the large density gradients for the particle flux and the electron energy flux in drift-diffusion approximation, the exponential scheme of Scharfetter-Gummel has been used. To avoid strong restrictions on the numerical time step, caused by coupling of the fluid equations with Poisson's equation, a semi-implicit procedure has been adapted for the self-consistent calculation of the radial potential.

The model has been used to identify and characterize the transition from the diffuse to the constricted mode of the dc positive column in argon in a discharge tube with radius of 1 cm for pressures between 100 and 500 Torr, and currents from 0.6 to 70 mA.

The analysis of the glow-to-arc transition is based upon the voltage-current characteristics as well as the dependence of the heavy particle temperature and density and mean energy of the electrons on the discharge current. Generally a good agreement is found between the standard model results, available experimental data and further modelling results. When applying a Maxwellian energy distribution for the electrons the experimentally confirmed glow-to-arc transition of the glow discharge plasma cannot be described for the parameter range considered. The assumption of the Druyvesteyn distribution for the electrons was found to be suitable for describing qualitatively the constriction effect. However, the best agreement has been archived using the EVDF obtained from the solution of the 0D electron BE with consideration of electron-electron collisions.

The role of molecular ion-atomic ion kinetics and heavy particle temperature in the discharge constriction phenomenon has been pointed out. In particular, an increase of the heavy particle temperature of the plasma filament leads to depopulation of the molecular ion density and as a consequence to a broadening of the characteristic radius of the positive column.

Properties of the argon positive column for higher currents have been predicted by means of the fluid modelling. The model predictions show that the

assumption of a Maxwellian energy distribution gives almost the same results as standard model for discharge currents $I \geq 1$ A and can be used for simplification in this parameter range.

The analysis of the power budget of the electrons by means of the standard model reveals the transition from a local to a nonlocal behaviour when the discharge jumps into the constricted mode. The further increase of the discharge current in the constricted mode leads to a transformation of the nonlocal situation back into an almost local one. This transition proceeds faster at higher pressure.

Model calculations have been carried out for xenon dc and pulsed discharges in a discharge tube with an inner diameter of 6.5 cm at currents between 60 and 150 mA and pressures from 10 to 50 Torr.

Model predictions for the dc column plasma in xenon show that the plasma is constricted at the pressure and current range considered. The model results agree well with available experimental data of the axial electric field.

There are still uncertainties in the atomic data. To investigate the influence of the cross sections on the results, the sensitivity analysis for the dc positive column in xenon has been performed as an example. The variation of the rate coefficients of the stepwise ionization as well as ion conversion has the largest influence on the behaviour of the dc xenon discharge.

The pulsed positive column in xenon plasmas at conditions of the contracted discharge has been studied by means of the standard model. The main features of the pulsed xenon discharge at medium pressure are discussed. The results have been compared with available experimental data of the axial electric field and of excited xenon atom densities. The agreement is well for the electric field. The model results reproduce the significant increase of low-lying (metastable and resonance) atomic levels densities in the early afterglow phase of the pulse, which has also been observed in the experiments. Additionally, a growth by approximately one order of magnitude of the higher and of the relaxed lowest vibrational states of the Xe_2^* excimers has been obtained during early afterglow phase of the pulse. They are responsible for an instant increase of the VUV radiation of the so-called first and second continuum around 151 and 172 nm, which has also been observed in the experiments.

The analysis of a medium-pressure xenon discharge in pulsed mode reveals that the increase of the low-lying atomic levels in the early afterglow is mainly caused by collision processes between high-lying levels and electrons, high-lying levels and ground state atoms and by radiation transitions from the high-lying levels. During the early afterglow the population of the high-lying levels increases due to decay of the electron temperature, which leads to growth of the dissociative recombination of the molecular ions. Such behaviour is more pronounced at higher pressure because of increases production of the molecular ions. The radial profile of the electron density becomes narrower with increasing pressure due to increases electron-atom collision frequency. During the afterglow phase of the discharge the electron loss takes place faster at higher pressure because of increased production of the molecular ions.

The analysis of the power budget of the electrons of a medium-pressure xenon discharge in pulsed mode shows slightly nonlocal behaviour of the mean electron energy balance during the active phase of the discharge. The afterglow phase of the discharge is characterized by pronounced nonlocal behaviour of the mean electron energy balance.

The possible future steps can be divided into four different fields:

- The constricted dc glow discharge in gas flow exhibits four different current regimes instead of only a single one in gas at rest [119]. One of these regimes corresponds to a spiral twisting of gas flow by the constricted flow discharge and can be used in plasma actuators to flow control. The physical model can be optimized by implementing the momentum balance equation for the mass averaged (neutrals, electronically excited atoms and positive ions) gas flow velocity.

- The proper description of the resonance radiation transfer is significant in the glow-to-arc transition, because it is one more factor acting against constriction. Therefore, application of the so-called matrix method [120] to describe the radiation trapping phenomenon instead of effective lifetime approach is required.

- Constriction effect is accompanied by the hysteresis phenomenon, i.e., the transition from glow to constricted mode at increasing current and the opposite transition at decreasing current occurs at different values of discharge parameters [3; 37]. The present model can be improved by applying the equation for the external electrical circuit as it was proposed in [4].

- Finally, the model could be extended in two dimensions in order to investigate the formation of complex discharge phenomena, e.g. striations, partially constricted positive column.

A

Appendix A

A.1 Argon collisional-radiative model

Table A.1: Reactions in argon plasma.

#	Reaction	Rate coefficient	Reference
	Excitation and de-excitation		
1	$Ar + e \rightarrow Ar^*(m) + e$	BE	[66; 67]
2	$Ar^*(m) + e \rightarrow Ar + e$	BE	[66; 67]
3	$Ar + e \rightarrow Ar^*(r) + e$	BE	[66; 67]
4	$Ar^*(r) + e \rightarrow Ar + e$	BE	[66; 67]
5	$Ar + e \rightarrow Ar^*(p) + e$	BE	[66; 67]
6	$Ar^*(p) + e \rightarrow Ar + e$	BE	[66; 67]
7	$Ar^*(m) + e \rightarrow Ar^*(r) + e$	BE	[66; 67]
8	$Ar^*(r) + e \rightarrow Ar^*(m) + e$	BE	[66; 67]
9	$Ar^*(m) + e \rightarrow Ar^*(p) + e$	BE	[66; 67]
10	$Ar^*(p) + e \rightarrow Ar^*(m) + e$	BE	[66; 67]
11	$Ar^*(r) + e \rightarrow Ar^*(p) + e$	BE	[66; 67]

continued on the next page

continued

#	Reaction	Rate coefficient	Reference
12	$Ar^*(p) + e \rightarrow Ar^*(r) + e$	BE	[66; 67]
	Ionization		
13	$Ar + e \rightarrow Ar^+ + 2e$	BE	[68]
14	$Ar^*(m) + e \rightarrow Ar^+ + 2e$	BE	[69]
15	$Ar^*(r) + e \rightarrow Ar^+ + 2e$	BE	[69]
16	$Ar^*(p) + e \rightarrow Ar^+ + 2e$	BE	[69]
17	$Ar_2^*(1) + e \rightarrow Ar_2^+ + 2e$	BE	[70]
18	$Ar_2^*(3) + e \rightarrow Ar_2^+ + 2e$	BE	[70]
	Three-body recombination		
19	$Ar^+ + 2e \rightarrow Ar^*(p) + e$	$7.19 \times 10^{-27}(T_e)^{-4.5}$	[9]
	Ion conversion		
20	$Ar^+ + 2Ar \rightarrow Ar_2^+ + Ar$	$2.25 \times 10^{-31}(T_h/300)^{-0.4}$	[72]
	Dissociative recombination		
21	$Ar_2^+ + e \rightarrow Ar^*(p) + Ar$	$6 \times 10^{-8}(T_e)^{-2/3}$ $\times(\frac{1-\exp(-418/T_h)}{1-0.31\exp(-418/T_h)})$	[71]
	Neutral association		
22	$Ar^*(m) + 2Ar \rightarrow Ar_2^*(3) + Ar$	8.3×10^{-33}	[9]
23	$Ar^*(m) + 2Ar \rightarrow Ar_2^*(1) + Ar$	2.5×10^{-32}	[9]
24	$Ar^*(r) + 2Ar \rightarrow Ar_2^*(3) + Ar$	8.3×10^{-33}	[9]
25	$Ar^*(r) + 2Ar \rightarrow Ar_2^*(1) + Ar$	2.5×10^{-32}	[9]
	Penning ionization		
26	$Ar^*(m) + Ar^*(m) \rightarrow Ar^+ + Ar + e$	1.3×10^{-9}	[73]
27	$Ar^*(r) + Ar^*(r) \rightarrow Ar^+ + Ar + e$	5×10^{-10}	[73]
28	$Ar^*(r) + Ar^*(m) \rightarrow Ar^+ + Ar + e$	5×10^{-10}	[73]
	Spontaneous radiation		
29	$Ar^*(p) \rightarrow Ar^*(m) + h\nu$	1.91482×10^7	[75; 76]
30	$Ar^*(p) \rightarrow Ar^*(r) + h\nu$	1.37507×10^7	[75; 76]
31	$Ar^*(r) \rightarrow Ar + h\nu$	3.15×10^8	[74–76]
32	$Ar_2^*(1) \rightarrow 2Ar + h\nu$	2.38×10^8	[75; 76]
33	$Ar_2^*(3) \rightarrow 2Ar + h\nu$	3.13×10^5	[75; 76]

Dimensions of the rate coefficients are following: two-body reaction - [cm^3/s], three-body-reaction - [cm^6/s], spontaneous radiation - [s^{-1}]. The "electron temperature" is deduced from the mean electron energy $T_e = (2/3)U_e$ and is given in [eV]. The heavy particle temperature T_h is given in [K]. For all radiation transitions natural lifetimes are given.

A.2 Xenon collisional-radiative model

Table A.2: Reactions in xenon plasma.

#	Reaction	Rate coefficient	Reference
	Excitation and de-excitation		
1	$Xe + e \rightarrow Xe^*(1s_5) + e$	BE	[82; 83]
2	$Xe^*(1s_5) + e \rightarrow Xe + e$	BE	[82; 83]
3	$Xe + e \rightarrow Xe^*(1s_3) + e$	BE	[82; 83]
4	$Xe^*(1s_3) + e \rightarrow Xe + e$	BE	[82; 83]
5	$Xe + e \rightarrow Xe^*(1s_4) + e$	BE	[82; 83]
6	$Xe^*(1s_4) + e \rightarrow Xe + e$	BE	[82; 83]
7	$Xe + e \rightarrow Xe^*(1s_2) + e$	BE	[82; 83]
8	$Xe^*(1s_2) + e \rightarrow Xe + e$	BE	[82; 83]
9	$Xe + e \rightarrow Xe^*(2p_{10}) + e$	BE	[82; 83]
10	$Xe^*(2p_{10}) + e \rightarrow Xe + e$	BE	[82; 83]
11	$Xe + e \rightarrow Xe^*(2p_{9..5}) + e$	BE	[82; 83]
12	$Xe^*(2p_{9..5}) + e \rightarrow Xe + e$	BE	[82; 83]
13	$Xe + e \rightarrow Xe^*(2p_{4..1}) + e$	BE	[82; 83]
14	$Xe^*(2p_{4..1}) + e \rightarrow Xe + e$	BE	[82; 83]
15	$Xe^*(1s_5) + e \rightarrow Xe^*(2p_{10}) + e$	BE	[84]
16	$Xe^*(2p_{10}) + e \rightarrow Xe^*(1s_5) + e$	BE	[84]
17	$Xe^*(1s_5) + e \rightarrow Xe^*(2p_{9..5}) + e$	BE	[84]
18	$Xe^*(2p_{9..5}) + e \rightarrow Xe^*(1s_5) + e$	BE	[84]
19	$Xe^*(1s_3) + e \rightarrow Xe^*(2p_{4..1}) + e$	BE	[84]
20	$Xe^*(2p_{4..1}) + e \rightarrow Xe^*(1s_3) + e$	BE	[84]
21	$Xe^*(1s_4) + e \rightarrow Xe^*(2p_{10}) + e$	BE	[84]
22	$Xe^*(2p_{10}) + e \rightarrow Xe^*(1s_4) + e$	BE	[84]
23	$Xe^*(1s_4) + e \rightarrow Xe^*(2p_{9..5}) + e$	BE	[84]
24	$Xe^*(2p_{9..5}) + e \rightarrow Xe^*(1s_4) + e$	BE	[84]
25	$Xe^*(1s_2) + e \rightarrow Xe^*(2p_{4..1}) + e$	BE	[84]
26	$Xe^*(2p_{4..1}) + e \rightarrow Xe^*(1s_2) + e$	BE	[84]
	Ionization and e-impact collisions		
27	$Xe + e \rightarrow Xe^+ + 2e$	BE	[85]
28	$Xe^*(1s_5) + e \rightarrow Xe^+ + 2e$	BE	[69]
29	$Xe^*(1s_3) + e \rightarrow Xe^+ + 2e$	BE	[69]
30	$Xe^*(1s_4) + e \rightarrow Xe^+ + 2e$	BE	[69]

continued on the next page

continued

#	Reaction	Rate coefficient	Reference
31	$Xe^*(1s_2) + e \rightarrow Xe^+ + 2e$	BE	[69]
32	$Xe^*(2p_{10}) + e \rightarrow Xe^+ + 2e$	BE	[69]
33	$Xe^*(2p_{9..5}) + e \rightarrow Xe^+ + 2e$	BE	[69]
34	$Xe^*(2p_{4..1}) + e \rightarrow Xe^+ + 2e$	BE	[69]
35	$Xe_2^*(1v) + e \rightarrow Xe_2^+ + 2e$	BE	[86]
36	$Xe_2^*(3v) + e \rightarrow Xe_2^+ + 2e$	BE	[86]
	Electron-ion recombination		
37	$Xe_2^+ + e \rightarrow Xe^+ + Xe + e$	BE	[87]
38	$Xe^+ + 2e \rightarrow Xe^*(2p_{10}) + e$	$2.38 \times 10^{-28}(T_e)^{-5}$	[88]
39	$Xe^+ + 2e \rightarrow Xe^*(2p_{9..5}) + e$	$1.66 \times 10^{-27}(T_e)^{-5}$	[88]
40	$Xe^+ + 2e \rightarrow Xe^*(2p_{4..1}) + e$	$9.52 \times 10^{-28}(T_e)^{-5}$	[88]
41	$Xe_2^+ + e \rightarrow Xe^*(2p_{10}) + Xe$	$1.00 \times 10^{-8}(T_e)^{-0.5}$ $\times(T_h/300)^{-0.75}$	[89; 98]
42	$Xe_2^+ + e \rightarrow Xe^*(2p_{9..5}) + Xe$	$7.05 \times 10^{-8}(T_e)^{-0.5}$ $\times(T_h/300)^{-0.75}$	[89; 98]
43	$Xe_2^+ + e \rightarrow Xe^*(2p_{4..1}) + Xe$	$4.03 \times 10^{-8}(T_e)^{-0.5}$ $\times(T_h/300)^{-0.75}$	[89; 98]
44	$Xe_3^+ + e \rightarrow Xe^*(2p_{10}) + 2Xe$	$1.90 \times 10^{-6}(T_e)^{-0.5}$ $\times(T_h/300)^{-0.75}$	[90; 98]
45	$Xe_3^+ + e \rightarrow Xe^*(2p_{9..5}) + 2Xe$	$1.33 \times 10^{-5}(T_e)^{-0.5}$ $\times(T_h/300)^{-0.75}$	[90; 98]
	Ion conversion		
46	$Xe^+ + 2Xe \rightarrow Xe_2^+ + Xe$	1.0×10^{-31} $\times(T_h/300)^{-0.75}$	[93; 98]
47	$Xe_2^+ + 2Xe \rightarrow Xe_3^+ + Xe$	9.0×10^{-32} $\times(T_h/300)^{-0.75}$	[94; 98]
48	$Xe_3^+ + Xe \rightarrow Xe_2^+ + 2Xe$	2.7×10^{-13}	[94]
	Conversion to dimer		
49	$Xe^*(1s_5) + 2Xe \rightarrow Xe_2^*(3v) + Xe$	8.55×10^{-32} $\times(T_h/300)^{-0.75}$	[95; 98]
50	$Xe_2^*(3v) + Xe \rightarrow Xe_2^*(3) + Xe$	7.0×10^{-11}	[96]
51	$Xe^*(1s_4) + 2Xe \rightarrow Xe_2^*(1v) + Xe$	1.4×10^{-31} $\times(T_h/300)^{-0.75}$	[96; 98]
52	$Xe_2^*(1v) + Xe \rightarrow Xe_2^*(1) + Xe$	7.0×10^{-11}	[96]
	Collisional de-activation		
53	$Xe^*(2p_{4..1}) + Xe \rightarrow Xe^*(2p_{9..5}) + Xe$	4.2×10^{-10}	[92]
54	$Xe^*(2p_{9..5}) + Xe \rightarrow Xe^*(2p_{10}) + Xe$	3.7×10^{-11}	[91]
55	$Xe^*(2p_{9..5}) + Xe \rightarrow Xe^*(1s_2) + Xe$	1.5×10^{-11}	[91]

continued on the next page

continued

#	Reaction	Rate coefficient	Reference
56	$Xe^*(2p_{9..5}) + Xe \rightarrow Xe^*(1s_3) + Xe$	3.7×10^{-11}	[91]
57	$Xe^*(2p_{10}) + Xe \rightarrow Xe^*(1s_2) + Xe$	1.0×10^{-10}	[91]
58	$Xe^*(2p_{10}) + Xe \rightarrow Xe^*(1s_3) + Xe$	6.0×10^{-11}	[91]
59	$Xe^*(2p_{10}) + Xe \rightarrow Xe^*(1s_4) + Xe$	1.0×10^{-11}	[91]
60	$Xe^*(2p_{10}) + Xe \rightarrow Xe^*(1s_5) + Xe$	1.0×10^{-11}	[91]
61	$Xe^*(1s_2) + Xe \rightarrow Xe^*(2p_{10}) + Xe$	6.6×10^{-11}	[91]
62	$Xe^*(1s_2) + Xe \rightarrow Xe^*(1s_4) + Xe$	4.5×10^{-12}	[91]
63	$Xe^*(1s_2) + Xe \rightarrow Xe^*(1s_5) + Xe$	4.5×10^{-12}	[91]
64	$Xe^*(1s_2) + Xe \rightarrow Xe^*(1s_3) + Xe$	2.5×10^{-11}	[91]
65	$Xe^*(1s_3) + Xe \rightarrow Xe^*(2p_{10}) + Xe$	2.0×10^{-12}	[91]
66	$Xe^*(1s_3) + Xe \rightarrow Xe^*(1s_5) + Xe$	4.5×10^{-12}	[91]
67	$Xe^*(1s_3) + Xe \rightarrow Xe^*(1s_4) + Xe$	4.5×10^{-12}	[91]
68	$Xe_2^*(1v) + Xe \rightarrow Xe^*(1s_5) + Xe$	2.6×10^{-10}	[96]
69	$Xe_2^*(1v) + Xe \rightarrow Xe^*(1s_4) + Xe$	5.8×10^{-11}	[96]
	Excited state-excited state collisions		
70	$Xe^*(1s_5) + Xe^*(1s_5) \rightarrow Xe^+ + Xe + e$	1.9×10^{-10}	[73]
71	$Xe^*(1s_4) + Xe^*(1s_4) \rightarrow Xe^+ + Xe + e$	1.9×10^{-10}	[73]
72	$Xe^*(1s_5) + Xe^*(1s_4) \rightarrow Xe^+ + Xe + e$	1.9×10^{-10}	[73]
	Interstate mixing		
73	$Xe^*(1s_5) + Xe \rightarrow Xe^*(1s_4) + Xe$	$9.27 \times 10^{-16} \exp(\frac{1416}{T_h})$	[97]
74	$Xe^*(1s_4) + Xe \rightarrow Xe^*(1s_5) + Xe$	1.03×10^{-13}	[97]
75	$Xe_2^*(3) + Xe \rightarrow Xe_2^*(1) + Xe$	4.6×10^{-15}	[96]
76	$Xe_2^*(1) + Xe \rightarrow Xe_2^*(3) + Xe$	1.25×10^{-13}	[97]
	Spontaneous radiation		
1	$Xe^*(2p_{10}) \rightarrow Xe^*(1s_4) + h\nu$	2.58×10^6	[100]
2	$Xe^*(2p_{10}) \rightarrow Xe^*(1s_5) + h\nu$	3.125×10^7	[100]
3	$Xe^*(2p_{9..5}) \rightarrow Xe^*(1s_4) + h\nu$	1.38×10^7	[100]
4	$Xe^*(2p_{9..5}) \rightarrow Xe^*(1s_5) + h\nu$	2.08×10^7	[100]
5	$Xe^*(2p_{4..1}) \rightarrow Xe^*(1s_2) + h\nu$	1.88×10^7	[100]
6	$Xe^*(2p_{4..1}) \rightarrow Xe^*(1s_3) + h\nu$	5.99×10^6	[100]
7	$Xe^*(1s_4) \rightarrow Xe + h\nu$	2.67×10^8	[74; 100]
8	$Xe^*(1s_2) \rightarrow Xe + h\nu$	2.5×10^8	[74; 100]
9	$Xe_2^*(3) \rightarrow 2Xe + h\nu$	9.71×10^6	[96]
10	$Xe_2^*(3v) \rightarrow 2Xe + h\nu$	2.5×10^7	[96]
11	$Xe_2^*(1) \rightarrow 2Xe + h\nu$	2.22×10^8	[96]
12	$Xe_2^*(1v) \rightarrow 2Xe + h\nu$	2.0×10^8	[96]

Dimensions of the rate coefficients are following: two-body reaction - [cm^3/s], three-body-reaction - [cm^6/s], spontaneous radiation - [s^{-1}]. The "electron temperature" is deduced from the mean electron energy $T_e = (2/3)U_e$ and is given in [eV]. The heavy particle temperature T_h is given in [K]. For all radiation transitions natural lifetimes are given.

B

Appendix B

B.1 Description of electron kinetic properties

In the framework of the standard fluid model, the stationary, spatially homogeneous Boltzmann equation of the electrons has been solved for given reduced electric field E_z/N, heavy particle temperature T_h, ionization degree n_e/N and collision cross section data (see Sec. 2.5) using a generalized version of the solution technique [57] adapted to account for non-conservative electron collision processes, the random motion of gas particles and electron-electron collisions [121]. Using the resulting isotropic distribution $f_0(U)$ and first anisotropic component $f_1(U)$ of the EVDF, the rate coefficients (B.7) and (2.18) as well as the transport coefficients of the electrons are determined, where the mobility and diffusion coefficient for the particle (μ_e, D_e) and energy (μ_ε, D_ε) transport are

given by [60; 122]

$$N\mu_e = -\frac{N}{3E_z}\sqrt{\frac{2}{m_e}}\int_0^\infty U f_1(U)\mathrm{d}U\,, \tag{B.1}$$

$$ND_e = \frac{1}{3}\sqrt{\frac{2}{m_e}}\int_0^\infty \frac{U}{Q_{\mathrm{eff}}} f_0(U)\mathrm{d}U\,, \tag{B.2}$$

$$N\mu_\varepsilon = -\frac{N}{3E_z}\sqrt{\frac{2}{m_e}}\int_0^\infty U^2 f_1(U)\mathrm{d}U\,, \tag{B.3}$$

$$ND_\varepsilon = \frac{1}{3}\sqrt{\frac{2}{m_e}}\int_0^\infty \frac{U^2}{Q_{\mathrm{eff}}} f_0(U)\mathrm{d}U\,. \tag{B.4}$$

The effective momentum transfer cross section

$$Q_{\mathrm{eff}} = \frac{1}{N}\left[\sum_j n_j\left(Q_j^d + \sum_m Q_{j,m}^{in}\right) + \sqrt{\frac{m_e}{2U}}\bar{\nu}^{io}\right] \tag{B.5}$$

in these equations includes the effect of possible temporal growth of the electron number density with the net production frequency $\bar{\nu}^{io}$ according to

$$\bar{\nu}^{io} = \sum_j \sum_k n_j k_{j,k}^{io}\,, \tag{B.6}$$

where the sum is over all ionization (io) processes. Finally, look-up tables for the electron coefficients (B.7), (2.18), (B.1), (B.2), (B.3) and (B.4) as functions of the mean electron energy $U_e = \int_0^\infty U^{3/2} f_0(U)\mathrm{d}U$, heavy particle temperature T_h and ionization degree n_e/N have been produced and used to treat these coefficients in the fluid model calculations. Thus, the dependence of the electron coefficients on time and space occurs via $U_e(r,t)$, $T_h(r,t)$ and $n_e(r,t)/N(r,t)$.

In particular, the rate coefficient $k_{j,m}^{in}$ of the mth inelastic collision process of electrons with the neutral species j has the representation [57]

$$k_{j,m}^{in} = \sqrt{\frac{2}{m_e}}\int_0^\infty U Q_{j,m}^{in}(U) f_0(U)\mathrm{d}U\,. \tag{B.7}$$

Here $f_0(U)$ denotes the isotropic part of the EVDF with the normalization $\int_0^\infty U^{1/2} f_0(U)\mathrm{d}U = 1$. U and m_e are the kinetic energy and mass of the electrons and $Q_{j,m}^{in}$ is the total cross section for the inelastic collision process considered with the energy loss or gain $U_{j,m}^{in}$.

Appendix C

Throughout this appendix, the (i) subscript indicates the mesh-point locations, the (j) subscript indicates species, n the number of points, while the superscript k is associated to an estimate at the time t^k. Subsequent time is given by $t^{k+1} = t^k + \Delta t$. The abbreviations used are the same as in Chapter 3.

C.1 Time and spatial discretization

C.1.1 Poisson's equation

$$A_i \Phi_{i-1}^{k+1} + B_i \Phi_i^{k+1} + C_i \Phi_{i+1}^{k+1} = R_i$$

$$A_i = -\frac{r_l \cdot h_p}{0.5 \cdot r_i \cdot h_m \cdot h_p \cdot (h_p + h_m)} \left(1 + \frac{e_0}{\varepsilon_0} \Delta t \sum_j (\mu_j)_{i-1/2}^k (n_j)_{i-1/2}^k \right)$$

$$C_i = -\frac{r_r \cdot h_m}{0.5 \cdot r_i \cdot h_m \cdot h_p \cdot (h_p + h_m)} \left(1 + \frac{e_0}{\varepsilon_0} \Delta t \sum_j (\mu_j)_{i+1/2}^k (n_j)_{i+1/2}^k \right)$$

$$B_i = -A_i - C_i$$

$$
\begin{aligned}
R_i \;=\; & \frac{e_0}{\varepsilon_0}\sum_j \mathrm{sgn}(\mathrm{Z_j})n_j + \\
& \frac{e_0}{\varepsilon_0}\Delta t\Big[\frac{r_l\cdot h_p}{0.5\cdot r_i\cdot h_m\cdot h_p\cdot(h_p+h_m)}\sum_j \mathrm{sgn}(\mathrm{Z_j})(D_j)^k_{i-1/2}(n_j)^k_{i-1/2} - \\
& \frac{h_p+h_m}{0.5\cdot h_m\cdot h_p\cdot(h_p+h_m)}\sum_j \mathrm{sgn}(\mathrm{Z_j})(D_j)^k_{i}(n_j)^k_{i} + \\
& \frac{r_r\cdot h_m}{0.5\cdot r_i\cdot h_m\cdot h_p\cdot(h_p+h_m)}\sum_j \mathrm{sgn}(\mathrm{Z_j})(D_j)^k_{i+1/2}(n_j)^k_{i+1/2}\Big]
\end{aligned}
$$

C.1.2 Transport equations for charge carriers and mean electron energy

$$A_i(n_j)^{k+1}_{i-1} + B_i(n_j)^{k+1}_{i} + C_i(n_j)^{k+1}_{i+1} = R_i$$

$$A_i = -\frac{r_l\cdot h_p}{0.5\cdot r_i\cdot h_p\cdot h_m\cdot(h_p+h_m)}(D_j)^k_{i-1/2}f_2\left(z_{i-1/2}\right)$$

$$C_i = \frac{r_r\cdot h_m}{0.5\cdot r_i\cdot h_p\cdot h_m\cdot(h_p+h_m)}(D_j)^k_{i+1/2}f_1\left(z_{i+1/2}\right)$$

$$
\begin{aligned}
B_i = \frac{1}{\Delta t} & - \frac{r_l\cdot h_p}{0.5\cdot r_i\cdot h_p\cdot h_m\cdot(h_p+h_m)}(D_j)^k_{i-1/2}f_1\left(z_{i-1/2}\right) + \\
& \frac{r_r\cdot h_m}{0.5\cdot r_i\cdot h_p\cdot h_m\cdot(h_p+h_m)}(D_j)^k_{i+1/2}f_2\left(z_{i+1/2}\right)
\end{aligned}
$$

$$R_i = \frac{(n_j)^k_i}{\Delta t} + (S_j)^k_i$$

$$z_{i+1/2} = -\frac{\mathrm{sgn}(Z_j)(\mu_j)^k_{i+1/2}(\Phi^{k+1}_{i+1} - \Phi^{k+1}_i)}{(D_j)^k_{i+1/2}}$$

The functions $f_1(z)$ and $f_2(z)$ are defined according to Eqs. 3.12 and 3.13.

C.1.3 Transport equation for metastable atoms

$$A_i(n_m)^{k+1}_{i-1} + B_i(n_m)^{k+1}_{i} + C_i(n_m)^{k+1}_{i+1} = R_i$$

$$A_i = -\frac{r_l\cdot h_p}{0.5\cdot r_i\cdot h_p\cdot h_m\cdot(h_p+h_m)}(D_m)^k_{i-1/2}$$

$$C_i = -\frac{r_r \cdot h_m}{0.5 \cdot r_i \cdot h_p \cdot h_m \cdot (h_p + h_m)} (D_m)^k_{i+1/2}$$

$$B_i = \frac{1}{\Delta t} - A_i - C_i$$

$$R_i = \frac{(n_m)^k_i}{\Delta t} + (S_m)^k_i$$

C.1.4 Transport equation for heavy particle temperature

$$A_i (T_h)^{k+1}_{i-1} + B_i (T_h)^{k+1}_i + C_i (T_h)^{k+1}_{i+1} = R_i$$

$$A_i = -\frac{r_l \cdot h_p}{0.5 \cdot r_i \cdot h_p \cdot h_m \cdot (h_p + h_m)} (\lambda_h)^k_{i-1/2}$$

$$C_i = -\frac{r_r \cdot h_m}{0.5 \cdot r_i \cdot h_p \cdot h_m \cdot (h_p + h_m)} (\lambda_h)^k_{i+1/2}$$

$$B_i = \frac{1}{\Delta t} - A_i - C_i$$

$$R_i = \frac{(T_h)^k_i}{\Delta t} + (S_{el})^k_i$$

C.1.5 Boundary conditions for charge carriers and mean electron energy

$$A_n (n_j)^{k+1}_{n-1} + B_n (n_j)^{k+1}_n = R_n$$

$$A_n = \frac{1}{r_n - r_{n-1}} (D_j)^k_{n-1/2} f_2(z_{n-1/2})$$

$$\begin{aligned} B_n \;=\; & \frac{1}{r_n - r_{n-1}} (D_j)^k_{n-1/2} f_1(z_{n-1/2}) - \\ & \frac{1 - b_j}{1 + b_j} \left(\mathrm{sgn}(Z_j)(2a_j - 1)(\mu_j)^k_n E^{k+1}_{r,n-1/2} + 0.5 V^k_{th,n} \right) \end{aligned}$$

$$R_n = 0$$

C.1.6 Boundary conditions for metastable atoms

$$A_n(n_m)_{n-1}^{k+1} + B_n(n_m)_n^{k+1} = R_n$$

$$A_n = \frac{1}{r_n - r_{n-1}}(D_m)_{n-1/2}^k$$

$$B_n = -\frac{1}{r_n - r_{n-1}}(D_m)_{n-1/2}^k - \frac{1 - b_m}{1 + b_m}\left(0.5V_{th,n}^k\right)$$

$$R_n = 0$$

C.1.7 Grid generation

All calculations have been performed with nonuniform grid. The example of the nonuniform grid with 21 grid points is illustrated in Fig. C.1.

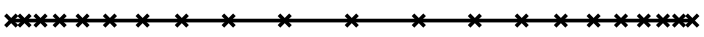

Figure C.1: The example of the nonuniform grid.

The grid is constructed by the code, which is presented below. The number of the grid points should be odd value.

```
subroutine grid(x,minx,maxx,n)

implicit none
integer,intent(in)::n !The number of the grid points.
real(kind=8),intent(in)::minx !  (0<minx<∞).  Low value implies higher
```

```
!  concentration of the grid points near boundaries.  High value leads
!  to almost equidistant grid.
real(kind=8),intent(in)::maxx !  Domain size.
real(kind=8),dimension(n),intent(out)::x !The grid output.
integer i
real(kind=8) ratio
ratio=(((maxx/2.0+minx)/minx)**(1.0/((n-1)/2.0)))-1.0
do i=1,(n-1)/2+1
x(i)=minx*((1.0+ratio)**(i-1))-minx
end do
do i=1,(n-1)/2
x((n-1)/2+i+1)=-x((n-1)/2+1-i)+maxx
end do
end subroutine
```

C.1.8 Numerical parameters

Table C.1: Numerical parameters.

Parameter	Value
Δr_i	$2 \cdot 10^{-3} - 2 \cdot 10^{-2}$ cm
n	101
Δt (pulsed)	$5 \cdot 10^{-12}$ s
Δt (steady-state)	$2.5 \cdot 10^{-11}$ s
CPU time	1 - 3 weeks

References

[1] Y. Raizer, *Gas Discharge Physics*. Berlin: Springer-Verlag, 1991.

[2] J. Massey and S. Cannon, "Constricted Discharges in the Rare Gases. I. Spectroscopic and Electrical Measurements," *J. Appl. Phys.*, vol. 36, pp. 361–372, 1964.

[3] Y. Golubovskii and R. Sonnenburg, "Contraction of an Inert-Gas Discharge. I. Argon (Experiment)," *Sov. Phys. Tech. Phys.*, vol. 24, pp. 173–177, 1979.

[4] N. Dyatko, Y. Ionikh, I. Kochetov, D. Marinov, A. Meshchanov, A. Napartovich, F. Petrov, and S. Starostin, "Experimental and Theoretical Study of the Transition Between Diffuse and Contracted Forms of the Glow Discharge in Argon," *J. Phys.D: Appl. Phys.*, vol. 41, p. 055204 (14pp), 2008.

[5] S. Watanabe, S. Saito, K. Takahashi, and T. Onzawa, "Observations of the Glow-To-Arc Transition between Thoriated Tungsten Electrodes with a Parallel RC Circuit," *J. Phys. D: Appl. Phys*, vol. 36, pp. 2521–2525, 2003.

[6] A. Fridman, A. Chirokov, and A. Gutsol, "Non-Thermal Atmospheric Pressure Discharges," *J. Phys. D: Appl. Phys*, vol. 38, pp. R1–R24, 2005.

[7] D. Staack, B. Farouk, A. Gutsol, and A. Fridman, "Characterization of a DC Atmospheric Pressure Normal Glow Discharge," *Plasma Sources Sci. Technol.*, vol. 14, pp. 700–711, 2005.

[8] G. Hogan and C. Webb, "Radially and Time-Resolved Measurements of Electron Density in an Operating Copper Vapour Laser," *Meas. Sci. Technol.*, vol. 8, pp. 1095–1104, 1997.

[9] A. Eletskii and B. Smirnov, "Physical Processes in Gas Lasers," *J. Russ. Las. Res.*, vol. 7, pp. 207–323, 1986.

[10] A. Czernichowski, "Gliding Arc. Application to Engineering and Enviroment Control," *Pure & Appl. Chem.*, vol. 66, pp. 1301–1310, 1994.

[11] J. Reiche, F. Könemann, W. Mende, and M. Kock, "Diagnostics of Discharge Modes of a Free-Burning Low-Current Argon Arc," *J. Phys. D: Appl. Phys.*, vol. 34, pp. 3177–3188, 2001.

[12] M. Lieberman and A. Lichtenberg, *Principles of Plasma Discharges and Material Processing*. New York: Wiley, 1994.

[13] G. Zissis and S. Kitsinelis, "State of Art on the Science and Technology of Electrical Light Sources: from the Past to the Future," *J. Phys. D: Appl.Phys.*, vol. 42, p. 173001, 2009.

[14] D. Uhrlandt, R. Bussiahn, S. Gorchakov, H. Lange, D. Loffhagen, and D. Nötzold, "Low-Pressure Mercury-Free Plasma Light Sources: Experimental and Theoretical Perspectives," *J. Phys. D: Appl.Phys.*, vol. 38, pp. 3318–3325, 2005.

[15] T. Nozaki and K. Okazaki, "Carbon Nanotube Synthesys in Atmospheric Pressure Glow Discharge: A Review," *Plasma Process. Polym.*, vol. 5, pp. 300–321, 2008.

[16] Q. Liang, C. Chin, J. Lai, C. Yan, Y. Meng, H. Mao, and R. Hemley, "Enhanced Growth of High Quality Single Crystal Diamond by Microwave Plasma Assisted Chemical Vapor Deposition at High Gas Pressures," *Appl. Phys. Lett.*, vol. 94, p. 034103, 2009.

[17] K. Yamakawa, M. Hori, T. Goto, S. Den, T. Katagiri, and H. Kano, "Etching Process of Silicon Dioxide with Nonequilibrium Atmospheric Pressure Plasma," *J. Appl. Phys.*, vol. 98, p. 013301, 2005.

[18] R. Sankaran and K. Giapis, "High-Pressure Micro-Discharges in Etching and Deposition Applications," *J. Phys. D: Appl. Phys*, vol. 36, pp. 2914–2921, 2003.

[19] C. Sarra-Bournet, S. Tungeon, D. Mantovani, and G. Laroche, "A Study of Atmospheric Pressure Plasma Discharges for Surface Functionalization of PTFE Used in Biomedical Applications," *J. Phys. D: Appl. Phys*, vol. 39, pp. 3461–3469, 2006.

[20] U. Kogelschatz, H. Esrom, Y.-Y. Zhang, and I. Boyd, "High-Intensity Sources of Incoherent UV and VUV Excimer Radiation for Low-Temperature Materials Processing," *Appl. Surf. Sci.*, vol. 168, pp. 29–36, 2000.

[21] K.-D. Weltmann, R. Brandenburg, T. von Woedtke, J. Ehlbeck, R. Foest, M. Stieber, and E. Kindel, "Antimicrobial Treatment of Heat Sensitive Products by Miniaturized Atmospheric Pressure Plasma Jets (APPJs)," *J. Phys. D: Appl. Phys*, vol. 41, p. 194008, 2008.

[22] T. Oppenländer, "Mercury-Free Sources of VUV/UV Radiation: Application of Modern Excimer Lamps (Excilamps) for Water and Air Treatment," *J. Environ. Eng. Sci.*, vol. 6, pp. 253–264, 2007.

[23] M. Jinno, M. Okamoto, M. Takeda, and H. Motomura, "Luminance and Efficacy Improvement of Low-Pressure Xenon Pulsed Fluorescent Lamps by Using an Auxiliary External Electrode," *J. Phys. D: Appl. Phys.*, vol. 40, pp. 3889–3885, 2007.

[24] C. Kenty, "Volume Recombination, Constriction, and Volt-Ampere Characteristics of the Positive Column," *Phys. Rev.*, vol. 126, pp. 1235–1238, 1962.

[25] J. Massey, "Constricted Discharges in the Rare Gases. II. Analysis of the Macroscopic Properties of the Discharge," *J. Appl. Phys.*, vol. 36, pp. 373–380, 1964.

[26] Y. Baranov and K. Yl'yanov, "Contraction of the Positive Column. I." *Sov. Phys. Tech. Phys.*, vol. 14, p. 176, 1969.

[27] ——, "Contraction of the Positive Column. II." *Sov. Phys. Tech. Phys.*, vol. 14, p. 183, 1969.

[28] S. Hatori and S. Shioda, "Contraction of a Positive Column in an Argon Glow Discharge," *J. Phys. Soc. Japan*, vol. 40, pp. 1449–1455, 1975.

[29] D. Venzke, "Untersuchungen der kontrahierten Edelgassäule bei mittleren Drücken. I. Verfahren zur Ermittlung der Plasmaparameter und ihrer Radialverteilungen," *Beitr. Plasmaphys.*, vol. 15, pp. 35–45, 1975.

[30] Y. Golubovskii, A. Zinchenko, and Y. Kagan, "Neon Positive Column at High Pressures," *Sov. Phys. Tech. Phys.*, vol. 22, pp. 851–855, 1977.

[31] D. Venzke, "Untersuchungen der kontrahierten Edelgassäule bei mittleren Drücken. II. Meßergebnisse in Argon," *Beitr. Plasmaphys.*, vol. 18, pp. 65–78, 1978.

[32] Y. Golubovskii and R. Sonnenburg, "Contraction of an Inert-Gas Discharge. III. Neon," *Sov. Phys. Tech. Phys.*, vol. 24, pp. 437–439, 1979.

[33] E. Toader, "On the Constricted Neon Positive Column," *J. Phys.D: Appl. Phys.*, vol. 28, pp. 75–80, 1994.

[34] A. Eletskii and B. Smirnov, "Contraction of the Positive Column of a Glow Discharge," *Sov. Phys. Tech. Phys.*, vol. 15, pp. 1308–1310, 1969.

[35] K. Ul'yanov, "Contraction of the Positive Column by Dissociative Recombination," *Sov. Phys. Tech. Phys.*, vol. 18, pp. 360–364, 1973.

[36] T. Růžička and K. Rohlena, "A Theory of the Positive Column Constriction in the Noble Gas Discharges at Medium Pressures," *Czech. J. Phys. B*, vol. 26, pp. 282–293, 1976.

[37] Y. Golubovskii and R. Sonnenburg, "Contraction of an Inert-Gas Discharge. II. Argon (Theory)," *Sov. Phys. Tech. Phys.*, vol. 24, pp. 177–180, 1979.

[38] Y. Golubovskii, V. Nekuchaev, and E. Pelyukova, "Contraction of a Gas Discharge Interpreted as a Phase Transition to a New Dissipative Structure," *Tech. Phys.*, vol. 41, pp. 254–260, 1996.

[39] ——, "Bifurcation Analysis of Contraction in Inert Gases I. Bifurcations of Steady-State Discharges," *Tech. Phys.*, vol. 41, pp. 1011–1019, 1996.

[40] G. Petrov and C. Ferreira, "Numerical Modelling of the Constriction of the DC Positive Column in Rare Gases," *Phys. Rev. E*, vol. 59, pp. 3571–3582, 1999.

[41] I. Shkurenkov, Y. Mankelevich, and T. Rakhimova, "Simulation of Diffuse, Constricted-Stratified, and Constricted Modes of a DC Dicharge in Argon: Hysteresis Transition between Diffuse and Constricted-Stratified Modes," *Phys. Rev. E*, vol. 79, p. 046406, 2009.

[42] K. Nobata and M. Kando, "Characteristics and Contraction of Oxygen Glow Discharge," *J. Appl. Phys.*, vol. 50, pp. 3956–3963, 1979.

[43] D. Ogle and G. Woolsey, "Diffuse and Constricted Glow Discharges in SF_6," *J. Phys. D: Appl. Phys.*, vol. 20, pp. 453–461, 1987.

[44] P. Daniels, R. Franklin, and J. Snell, "The Contracted Positive Column in Electronegative Gases," *J. Phys. D: Appl. Phys.*, vol. 23, pp. 823–831, 1990.

[45] P. Milsom, "Constriction of the Positive Column in a DC-Driven Sulphur Hexafluoride Gas Discharge," *J. Phys. D: Appl. Phys.*, vol. 29, pp. 403–410, 1996.

[46] Y. Kabouzi, M. Calzada, M. Moisan, K. Tran, and C. Trassy, "Radial Contraction of Microwave-Sustained Plasma Columns at Atmospheric Pressure," *J. Appl. Phys.*, vol. 91, pp. 1008–1019, 2002.

[47] E. Godolides and H. Sawin, "Continuum Modeling of Radio-Frequency Glow Discharges. I. Theory and Results for Electropositive and Electronegative Gases," *J. Appl. Phys.*, vol. 72, pp. 3971–3987, 1992.

[48] J. Verboncoeur, J. Parker, B. Penetrante, and M. W., "Comparison of Collision Rates in Particle-in-Cell, Monte Carlo, and Boltzmann Codes," *J. Appl. Phys.*, vol. 80, pp. 1299–1303, 1996.

[49] S. Longo, "Monte Carlo Simulation of Charged Species Kinetics in Weakly Ionized Gases," *Plasma Sourses Sci. Technol.*, vol. 15, pp. S181–S188, 2006.

[50] D. Loffhagen and F. Sigeneger, "Advances in Boltzmann Equation Based Modelling of Discharge Plasmas," *Plasma Sources Sci. Technol.*, vol. 18, p. 034006, 2009.

[51] V. Kolobov and R. Arslanbekov, "Simulation of Electron Kinetics in Gas Discharges," *IEEE Trans. Plasma Sci.*, vol. 34, pp. 895–909, 2006.

[52] J. Ingold, "Nonequilibrium Positive Column," *Phys. Rev. E*, vol. 56, pp. 5932–5944, 1997.

[53] V. E. Golant, A. P. Zhilinsky, and I. E. Sakharov, *Fundamentals of Plasma Physics*. New York: Wiley, 1980.

[54] I. Shkarofsky, T. Johnston, and M. Bachynski, *The Particle Kinetics of Plasmas*. Reading, MA: Addison-Wesley, 1966.

[55] G. M. W. Kroesen, D. C. Schram, C. J. Timmermans, and J. C. M. de Haas, "The Energy Balance of a Plasma in Partial Local Thermodynamic Equilibrium," *IEEE Trans. Plasma Sci.*, vol. 18, pp. 985–991, 1990.

[56] R. Winkler and M. W. Wuttke, "A detailed study of electron kinetics involved in modelling discharge pumped excimer laser plasmas," *Appl. Phys. B*, vol. 54, pp. 1–17, 1992.

[57] H. Leyh, D. Loffhagen, and R. Winkler, "A New Multi-Term Solution Technique for the Electron Boltzmann Equation Weakly Ionized Steady-State Plasmas," *Comp. Phys. Commun.*, vol. 113, pp. 33–48, 1998.

[58] D. Loffhagen, "Impact of electron-electron collisions on the spatial electron relaxation in non-isothermal plasmas," *Plasma Chem. Plasma Process.*, vol. 25, no. 5, pp. 519–538, 2005.

[59] ——, private communication, 2009.

[60] G. Hagelaar and L. Pitchford, "Solving the Boltzmann Equation to Obtain Electron Transport Coefficients and Rate Coefficients for Fluid Models," *Plasma Sources Sci. Technol.*, vol. 14, pp. 722–733, 2005.

[61] D. Loffhagen, F. Sigeneger, and R. Winkler, "Electron kinetics in weakly ionized plasmas," in *Low Temperature Plasmas: Fundamentals, Technologies and Techniques*, 2nd ed., R. Hippler, H. Kersten, M. Schmidt, and K. H. Schoenbach, Eds. Weinheim: WILEY-VCH, 2008, vol. 1, ch. 2, pp. 15–45.

[62] G. Hagelaar, F. de Hoog, and G. Kroesen, "Boundary Conditions in Fluid Models of Gas Discharges," *Phys. Rev. E*, vol. 62, pp. 1452–1454, 2000.

[63] P. Macko and N. Sadeghi, "Determination of the Non-Relaxation (Reflection) Probability of Metastable Ar($^3P_2$) Atoms on a Pyrex Surface," *Plasma Sources Sci. Technol.*, vol. 13, pp. 303–308, 2004.

[64] W. J. M. Brok, J. van Dijk, M. D. Bowden, J. J. A. M. van der Mullen, and G. M. W. Kroesen, "A Model Study of Propagation of the First Ionization Wave during Breakdown in a Straight Tube Containing Argon," *J. Phys. D: Appl. Phys.*, vol. 36, no. 16, pp. 1967–1979, 2003.

[65] C. Yamabe, S. Buckman, and A. Phelps, "Measurement of Free-Free Emision from Low-Energy-Electron Collisions with Ar," *Phys. Rev. A*, vol. 27, pp. 1345–1352, 1983.

[66] O. Zatsarinny and K. Bartschat, "*B*-Spline Breit-Pauli *R*-Matrix Calculations for Electron Collisions with Argon Atoms," *J. Phys. B: At. Mol. Opt. Phys*, vol. 37, pp. 4693–4706, 1999.

[67] M. Hayashi, "Bibliography of Electron and Photon Cross Sections with Atoms and Molecules Published in the 20th Century - Argon -," *NIFS-DATA-072*, 2003.

[68] D. Rapp and P. Englander-Golden, "Total Cross Sections for Ionization and Attachment in Gases by Electron Impact .I. Positive Ionization," *J. Chem. Phys.*, vol. 43, pp. 1464–1479, 1965.

[69] H. Deutsch, K. Becker, S. Matt, and T. Märk, "Calculated Cross Sections for the Electron-Impact Ionization of Metastable Atoms," *J. Phys. B: At. Mol. Opt. Phys*, vol. 32, pp. 4249–4259, 1999.

[70] M. Flannery and K. McCann, "Cross Sections for Ionization of Rare Gas Excimers by Electron Impact and Atomic and Molecular Processes in Excimer Lasers," *Technical Report AFWAL-TR-80-2015*, p. 16, 1980.

[71] A. Cunningham, T. O'Malley, and R. Hobson, "On the Role of Vibrational Excitation in Dissociative Recombination," *J. Phys. B: At. Mol. Opt. Phys*, vol. 14, pp. 773–782, 1981.

[72] J. Jones, D. Lister, D. Wareing, and N. Twiddy, "The Temperature Dependence of the Three-Body Reaction Rate Coefficient for Some Rare-Gas Atomic Ion-Atom Reactions in the Range 100-300 K," *J. Phys. B: At. Mol. Opt. Phys*, vol. 13, pp. 3247–3255, 1980.

[73] N. Kolokolov, A. Kudrjavtsev, and A. Blagoev, "Interaction Processes with Creation of Fast Electrons in the Low Temperature Plasma," *Phys. Scr.*, vol. 50, pp. 371–402, 1994.

[74] T. Holstein, "Imprisonment of Resonance Radiation in Gases. II," *Phys. Rev.*, vol. 83, no. 6, pp. 1159–1168, 1951.

[75] W. Wiese, J. Braulth, K. Danzmann, V. Helbig, and M. Kock, "Unified Set of Atomic Transitions Probabilities for Neutral Argon," *Phys. Rev. A*, vol. 39, pp. 2461–2471, 1989.

[76] A. Irimia and C. Fischer, "Breit-Pauli and Dirac-Hartree-Fock Energy Levels and Transition Probabilities in Neutral Argon," *J. Phys. B: At. Mol. Opt. Phys*, vol. 37, p. 16591672, 2004.

[77] A. Phelps and Z. Petrović, "Cold-Cathode Discharges and Breakdown in Argon: Surface and Gas Phase Production of Secondary Electrons," *Plasma Sources Sci. Technol.*, vol. 8, pp. R21–R44, 1999.

[78] H. Ellis, R. Pai, E. McDaniel, E. Mason, and L. Viehland, "Transport Properties of Gaseous Ions over a Wide Energy Range," *Atomic Data and Nuclear Data Tables*, vol. 17, pp. 177–210, 1976.

[79] J. Velazco, J. Kolts, and D. Setser, "Rate Constants and Quenching Mechanism for Metastable States of Argon, Krypton, and Xenon," *J. Chem. Phys.*, vol. 69, pp. 4357–4373, 1978.

[80] L. Sin Fai Lam, "Relativistic Effects in Electron Scattering by Atoms III. Elastic Scattering by Krypton, Xenon and Radon," *J. Phys. B: At. Mol. Opt. Phys*, vol. 15, pp. 119–142, 1982.

[81] M. Hayashi, "Determination of Electron-Xenon Total Excitation Cross Sections, from Threshold to 100 eV, from Experimental Values of Townsends α," *J. Phys. D: Appl. Phys.*, vol. 16, pp. 581–589, 1983.

[82] S. Nakazaki, K. Berrington, W. Eissner, and Y. Itikawa, "Excitation of Xenon by Electron Impact," *J. Phys. B: At. Mol. Opt. Phys*, vol. 30, pp. 5805–5818, 1997.

[83] M. Puech and S. Mizzi, "Collision Cross Sections and Transport Parameters in Neon and Xenon," *J. Phys. D: Appl. Phys.*, vol. 24, pp. 1974–1985, 1991.

[84] L. Vriens and A. Smeets, "Cross-Section and Rate Formulas for Electron-Impact Ionization, Excitation, Deexcitation, and Total Depopulation of Excited Atoms," *Phys. Rev. A*, vol. 22, pp. 940–951, 1980.

[85] R. Wetzel, F. Baiocchi, T. Hayes, and R. Freund, "Absolute Cross-Sections for Electron-Impact Ionization of the Rare-Gas Atoms by the Fast-Neutral-Beam Method," *Phys. Rev. A*, vol. 35, pp. 559–577, 1987.

[86] M. Flannery, K. McCann, and N. Winter, "Cross Sections for Electron Impact Ionisation of Metastable Rare-Gas Excimers (He_2^*, Kr_2^*, Xe_2^*)," *J. Phys. B: At. Mol. Opt. Phys*, vol. 14, pp. 3789–3796, 1981.

[87] V. Marchenko, "Dissociation of Homonuclear Ions by Electron Impact," *Sov. Phys. JETP*, vol. 58, pp. 292–298, 1984.

[88] R. Carman, "A Self-Consistent Model for a Longitudinal Discharge Excited He-Sr Recombination Laser," *IEEE J. Quantum Electron.*, vol. QE-26, pp. 1588–1608, 1990.

[89] H. Oskam and V. Mittelstadt, "Recombination Coefficient of Molecular Rare-Gas Ions," *Phys. Rev.*, vol. 132, pp. 1445–1454, 1963.

[90] C. Werner, E. George, P. Hoff, and C. Rhodes, "Radiative and Kinetic Mechanisms in Bound-Free Excimer Lasers," *IEEE J. Quantum Electron.*, vol. QE-13, pp. 769–783, 1977.

[91] W. Alford, "State-to-State Rate Constans for Quenching of Xenon $6p$ Levels by Rare Gases," *J. Chem. Phys.*, vol. 96, pp. 4330–4340, 1992.

[92] T. Nelson, D. Setser, and M. Richmann, "Quenching Rate Constans of the Xe($5p^5$6p and 6p) States and the Energy-Pooling Ionization Reaction of Xe($5p^5$6p) Atoms ," *J. Phys. Chem.*, vol. 99, pp. 7482–7494, 1995.

[93] Y. Gabrielyan, V. Papanyan, and S. Ter-Avetisyan, "Xenon Discharge Afterglow in the VUV Region," *Opt. Spektrosk.*, vol. 70, pp. 736–741, 1991.

[94] R. Carman and R. Mildren, "Computer Modelling of a Short-Pulse Excited Dielectric Barrier Discharge Xenon Excimer Lamp ($\lambda \sim 172$ nm)," *J. Phys. D: Appl. Phys.*, vol. 36, pp. 19–33, 2003.

[95] W. Wieme, "Decay of Excited Species in the Afterglow of a Pulsed Discharge in Xenon," *J. Phys. B: Atom. Mol. Phys.*, vol. 7, pp. 850–856, 1974.

[96] P. Moutard, P. Laporte, J.-L. Subtil, N. Damany, and H. Damany, "Pressure Effects on Kinetics and Decay Processes in Xenon after Selective Photoexcitation," *J. Chem. Phys.*, vol. 88, pp. 7485–7500, 1988.

[97] W. Wieme and J. Lenaerts, "Excimer Formation in Argon, Krypton, and Xenon Discharge Afterglows between 200 and 400 K," *J. Chem. Phys.*, vol. 74, pp. 483–493, 1981.

[98] A. Karelin and O. Simakova, "Kinetics of the Active Medium of a Multi-wave IR Xenon Laser in Hard-Ioniser-Pumped Mixtures with He and Ar. I. Electron-Beam Pumping," *Quantum Electron.*, vol. 29, pp. 678–686, 1999.

[99] V. Ivanov and Y. Skoblo, "Plasma Decay Rate in Diffuse and Contracted Discharges in Xenon," *Sov. J. Plasma Phys.*, vol. 12, pp. 406–409, 1986.

[100] M. Aymar and M. Coulombe, "Theoretical Transition Probabilities and Lifetimes in Kr I and Xe I Spectra," *At. Data Nucl. Data Tables*, vol. 21, pp. 537–566, 1978.

[101] M. Biondi and L. Chanin, "Mobilities of Atomic and Molecular Ions in the Noble Gases," *Phys. Rev.*, vol. 94, pp. 910–916, 1954.

[102] A. Barbet, N. Sadeghi, and J. Pebay-Peyroula, "Decay of Metastable Xenon Atoms $Xe^*(^3P_2)$ in a Xenon Afterglow," *J. Phys. B: Atom. Molec. Phys.*, vol. 8, pp. 1776–1784, 1975.

[103] N. Vargaftik and Y. Vasilevskaya, "Thermal Conductivity of Krypton and Xenon at Temperatures up to 5000 K," *J. Eng. Phys. Thermophys.*, vol. 39, pp. 1217–1222, 1980.

[104] D. U. von Rosenberg, *Methods for the Numerical Solution of Partial Differential Equations.* New York: American Elsevier, 1969.

[105] R. Courant, K. Friedrichs, and H. Lewy, "Über die partiellen Differenzengleichungen der mathematischen Physik," *Math. Ann.*, vol. 100, p. 1, 1928.

[106] D. Scharfetter and H. Gummel, "Large-Signal Analysis of a Silicon Read Diod Oscillator," *IEEE Trans. Electron Devices*, vol. ED-16, pp. 64–77, 1969.

[107] M. Barnes, T. Colter, and M. Elta, "Large-Signal Time-Domain Signal Modeling of Low-Pressure RF Glow Discharges," *J. Appl. Phys.*, vol. 61, pp. 81–89, 1987.

[108] J.-P. Boeuf and L. Pitchford, "Pseudospark Discharges Via Computer Simulation," *IEEE Trans. Plasma Sci.*, vol. 19, pp. 286–296, 1991.

[109] P. Ventzek, R. Hoekstra, and M. Kushner, "Two-Dimensional Modeling of High Plasma Density Inductively Coupled Sources for Material Processing," *J. Vac. Sci. Technol. B*, vol. 12, pp. 461–477, 1994.

[110] A. Eletskii and B. Smirnov, "Nonuniform Gas Discharge Plasma," *Physics Uspekhi*, vol. 39, pp. 1137–1156, 1996.

[111] D. Uhrlandt, "Power Balance and Space-Charge Confinement in a Neon DC Column Plasma," *J. Phys. D: Appl. Phys.*, vol. 35, pp. 2159–2168, 2002.

[112] T. Scherzer, A. Tauber, and R. Mehnert, "UV Curing of Pressure Sensitive Adhesives Studied by Real-Time FTIR-ATR Spectroscopy," *Vibr. Spectr.*, vol. 29, pp. 125–131, 2002.

[113] J. Zhang, H. Esrom, and I. Boyd, "Decomposition Mechanisms of Thin Palladium Acetate Film with Excimer UV Radiation," *Appl. Surf. Sci.*, vol. 96-98, pp. 399–404, 1996.

[114] J. Madsen, Z. Cui, and C. Takoudis, "Low Temperature Oxidation of SiGe in Ozone: Ultrathin Oxides," *J. Appl. Phys.*, vol. 87, pp. 2046–2051, 2000.

[115] W. Chen, J. Zhang, F. Qi, K. Hu, and I. Boyd, "Surface Modification of Polyimide with Excimer UV Radiation at Wavelength of 126 nm," *Thin Solid Films*, vol. 453-454, pp. 3–6, 2004.

[116] E. Kindel and C. Schimke, "Measurements of Excited States Density and the VUV-Radiation in the Pulsed Xenon Medium Pressure Discharge," *Contrib. Plasma Phys.*, vol. 36, pp. 711–721, 1996.

[117] E. Kindel, private communication, 2009.

[118] S. Kleditzsch and U. Riedel, "Sensitivity Studies for Volume Averaged Models of Plasma Etch Reactors," *Surf. Coat. Technol.*, vol. 142-144, pp. 536–539, 2001.

[119] Y. Akishev, M. Grushin, V. Karalnik, A. Petryakov, and N. Trushkin, "Non-Equilibrium Constricted DC Glow Discharge in N_2 Flow at Atmospheric Pressure: Stable and Unstable Regimes," *J. Phys. D: Appl. Phys.*, vol. 43, p. 075202, 2010.

[120] Y. Golubovskii, I. Porokhova, H. Lange, and D. Uhrlandt, "Metastable and Resonance Atom Densities in a Positive Column: I. Distinctions in Diffusion and Radiation Transport ," *Plasma Sources Sci. Technol.*, vol. 14, pp. 36–44, 2005.

[121] M. Hannemann, P. Hardt, D. Loffhagen, M. Schmidt, and R. Winkler, "The Electron Kinetics in the Cathode Region of $H_2/Ar/N_2$ Discharges," *Plasma Sources Sci. Technol.*, vol. 9, pp. 387–399, 2000.

[122] N. R. Pinhão, Z. Donkó, D. Loffhagen, M. J. Pinheiro, and E. A. Richley, "Comparison of Kinetic Calculation Techniques for the Analysis of Electron Swarm Transport at Low to Moderate E/N Values," *Plasma Sources Sci. Technol.*, vol. 13, no. 4, pp. 719–728, 2004.

Acknowledgement

I would like to express my gratitude to all the people who gave me assistance and support during my work at Leibniz Institute for Plasma Science and Technology (INP Greifswald). They motivated me by giving new views on current problems as well as new ideas.

First of all I would like to thank my two supervisors Priv.-Doz. Dr. Detlef Loffhagen and Dr. Dirk Uhrlandt for believing in me and for giving me the great opportunity to do this PhD. I am thankful for the interesting topic proposed, for many helpful discussions during the work, and for patiently explaining to me the basics of plasma physics modelling. This support and encouragement help me a lot to finish the complicated task of writing this thesis.

I am very grateful to all members of Plasma Modelling Group for supporting me all the time, especially Dr. Sergey Gorchakov for assistance during first time in Germany as well as for introduction to me the basics of numerical modelling. I thank Dr. Gordon Grubert for kind help with all the computer problems. I want also acknowledge Dr. Margarita Baeva for creating a friendly, informal, and collaborative atmosphere.

I would like to thank Professor Yuriy Golubovskii for his helpful conversations about constriction of glow discharges.

Most importantly, I would like to thank my parents, Vasyliy and Lyudmyla Gnybida, for their support and love. I would also like to thank my sister, Olena, for her support and friendship too.

Erklärung

Hiermit erkläre ich, daß diese Arbeit bisher von mir weder an der Mathematisch-Naturwissenschaftlichen Fakultät der Ernst-Moritz-Arndt-Universität Greifswald noch einer anderen wissenschaftlichen Einrichtung zum Zwecke der Promotion eingereicht wurde.

Ferner erkläre ich, daß ich diese Arbeit selbständig verfaßt und keine anderen als die darin angegebenen Hilfsmittel benutzt habe.

_____

(Mykhaylo Gnybida)

Curriculum Vitae

Personal information

Name:	Mykhaylo Gnybida
Date of Birth:	April 1, 1982
Place of Birth:	Kamenets-Podolsky, Ukraine
Nationality:	Ukrainian
Address:	330, Makarenkostr. 35a, 17491, Greifswald, Germany
Phone:	+49 (03834) 554466
E-mail:	gnybida@inp-greifswald.de

Education

since 10/06	PhD study at Leibniz Institute for Plasma Science and Technology, Greifswald, Germany
09/03-03/05	M.Sc. in applied physics, Kharkiv "V. N. Karazin" National University, Kharkiv, Ukraine
09/99-06/03	B.Sc. in applied physics, Kharkiv "V. N. Karazin" National University, Kharkiv, Ukraine

Work experience

since 04/06	Scientific staff member at Leibniz Institute for Plasma Science and Technology, Greifswald, Germany
04/05-03/06	Engineer-physicist at National Science Center "Kharkiv Institute of Physics and Technology", Kharkiv, Ukraine